Title:

Improvements of cuttings transport models through physical experiments and numerical investigations of solid-liquid transport

A thesis submitted in fullfilment of the requirements
for the degree of Doctor of Engineering

Presented by

Roger Aragall Tersa
from Barcelona

approved by the
Faculty of Mathematics/Computer Science and Mechanical Engineering
of the University of Clausthal

Day of the presentation
30.10.2015

Bibliografische Information der Deutschen Nationalbibliothek

Die Deutsche Nationalbibliothek verzeichnet diese Publikation in der Deutschen Nationalbibliografie; detaillierte bibliografische Daten sind im Internet über http://dnb.dnb.de abrufbar.

Bibliographic information published by the Deutsche Nationalbibliothek

The Deutsche Nationalbibliothek lists this publication in the Deutsche Nationalbibliografie; detailed bibliographic data are available in the Internet at http://dnb.dnb.de.

Chairperson of the Board of Examiners:	Prof. Dr.-Ing. Armin Lohrengel
Chief Reviewer:	Prof. Dr.-Ing. habil. Gunther Brenner
Reviewer:	Prof. Dr.-Ing. Joachim Oppelt

Dissertation Clausthal 2015

D 104

© **PAPIERFLIEGER VERLAG** GmbH, Clausthal-Zellerfeld, 2016
Telemannstraße 1 · 38678 Clausthal-Zellerfeld
www.papierflieger.eu

1. Auflage, 2016

ISBN 978-3-86948-498-3

Foreword and Acknowledgements

This thesis took shape during my time as research assistant at the Institute of Applied Mechanics (Institut für Technische Mechanik) belonging to the Clausthal University of Technology, from 01.09.2009 to 07.07.2015 in the frame of the Geothermal Energy and High Performance Drilling Research Program gebo between the federal state of Lower Saxony and the company Baker Hughes.

I wish to take this opportunity to express my sincere thanks to my supervisor Prof. Dr.-Ing. Gunther Brenner. At the beginning, for giving me the opportunity to participate in his group of research. During the time at the institute, for teaching me so many lessons in technical and not so technical matters, as well as for granting optimal work conditions. Finally, for his confidence and interest in the progress of my work. Without him, this thesis would not have been possible.

I would also like to thank Prof. Dr.-Ing. Joachim Oppelt for the interest in my work and for his acceptance of the review. Likewise, I would like to thank Prof. Dr.-Ing. Armin Lohrengel for his participation as Chairperson of the Board of Examiners.

I would like to thank, as well, the staff at the Institute of Applied Mechanics. Prof. Dr.-Ing. Stefan Hartmann for granting optimal working conditions during his time as head of the institute, Heidi Andresen for helping me with the financial and administrative matters, Bernd Riechel for his support in relation to computational matters and Joachim Koch for his technical assistance.

During my research, a number of students chose to do their M.Sc., Diploma or Bachelor thesis work with me. Their work has been a significant contribution to this thesis. Therefore, I would like to thank Pavan Kumar (for helping me with the construction of the experimental flow loop), Corina Mäder (who assisted with the first multi-phase measurements and helped improve its accuracy), Vijay Mulchandani (who assisted with measurements of bidisperse suspensions), Fan Yu and Jian Dai (who assisted in the validation of the CFD-DEM simulations) and Matthias Thurmann (who implemeted a procedure to automatize the numerical simulation campaigns). Further thanks are due to Hanno Fassbinder and the company Sympatec, for offering his assistance in the measurements of the glass spheres particle size distributions.

During my time at the department of Fluid Mechanics of the Institute of Applied Mechanics, I had the chance to work with two groups of fantastic people. Right at the start, with Dr.-Ing. Andreas Lucius, Dipl.-Ing. Merim Mukinovic, Dr.-Ing. Ernesto Monaco, Dipl.-Ing. Yang Yang, Dipl.-Inf. Yong Ma and Dr.-Ing. Rashid Jamshidi we shared many common experiences and interesting talks. In the second part, with Dipl.-Ing. Christian Walter, Dipl.-Ing. Geni Barthelmie and M.Sc. Sergey Lesnik I got a new impulse due to their vitality and positive attitude.

The work in the frame of the gebo project gave me the opportunity to get to know a large number of great people. Between them, I would specially like to thank Dr. Martina Weichmann and Dipl.-Ing. Roland May. The former for her tips and recommendations in relation to scientific work. The latter for his support and the always interesting conversations.

I would also like to thank my parents Josep and Teresa, my sister Núria and all my friends for supporting me through the years.

Finally, I would like to thank my family, especially my wife Àngels, who accepted starting this adventure together, and my children Ona and Jan for their comprehension, patience and support.

Goslar, March 2016. Roger Aragall Tersa

Abstract

Wellbore drilling has experienced an increase in complexity due to the interest in reaching targets situated in High Pressure-High Temperature (HPHT) environments or constructing large sections of the well with high deviations from verticality. Established models for selecting operational flow rates or drilling fluid rheology and density are based on empirical correlations. These are only applicable for well defined ranges of conditions and for stationary assumptions not given in complex wellbores. In the last two decades, more flexible and transient models founded on causal mechanisms responsible of the system's behavior are finding wider application. These rely on an accurate understanding of the phenomena taking place within the wellbore. High resolution numerical models can be used to increase this understanding. However, experimental data are still needed for their validation. This thesis provides such experimental data and evaluates high resolution numerical models able to predict cuttings transport relevant phenomena at the wellbore diameter scale.

In the experimental part of this thesis, a solid-liquid vertical flow-loop designed and constructed to generate experimental data for validation is presented. The setup consists of a 64 mm diameter and 2,000 mm length pipe, medicinal white oil and glass spherical particles with diameters ranging from 2 to 6 mm providing a system with physical phenomena similar to the one found in cuttings transport. The particle image velocimetry (PIV) and particle tracking velocimetry (PTV) techniques are implemented to obtain liquid and particles velocity profiles as well as particle position histograms of solid-liquid mono- and bidisperse flows. This is accomplished through refractive index matching of the dispersed phase, the continuous phase and the conduct material. Results point out the relevancy of the lift force in configuring particles distribution across the pipe section. This force creates concentration accumulations at specific radial positions. Furthermore, a significant momentum transfer between the considered particles is observed in bidisperse systems.

The computational part of the thesis considers the implementation of the two-fluid method and the discrete particle model (DPM) to simulate the experimental system and prove their validity for the prediction of cuttings transport relevant problems. The two-fluid method shows good agreement with experiments performed with monodisperse systems and supplies an explanation for the concentration accumulations observed in the experiments. However, this lacks predictive capacity when polydisperse systems are investigated. On the other hand, the DPM model implemented here is able to reproduce bidisperse experimental results up to 3% concentrations. For higher ones, advanced models considering particle collisions in viscous fluids should be included. The DPM model is selected as the best alternative for cuttings transport problems. A sensitivity analysis focused on the effect of eccentricity on vertical particle transport is finally conducted to demonstrate which information can be extracted. The sensitivity analysis reveals the effect of the lift force on particle transport, which results in better transport than the one predicted with the homogeneous particle distribution assumption, normally taken in drilling engineering calculations.

Kurzfassung

Das Auffahren von Bohrlöchern ist anspruchsvoller geworden, da zunehmend unter Umgebungsbedingungen mit höheren Drücken und Temperaturen (High Pressure-High Temperature - HPHT) gearbeitet wird. Zusätzlich erschwerend werden große Teile der Bohrungen schräg oder vertikal ausgeführt. Die etablierte Modelle zur Bestimmung der Volumenströme und Bohrflüssigkeitseigenschaften basieren auf empirischen Annahmen. Sie sind nur für bestimmte Betriebsbedingungen geeignet und beruhen auf der Annahme stationärer Zustände. Damit vernachlässigen sie viele Bohrlochphänomene. In den letzten beiden Jahrzehnten haben transiente Modelle, die systemrelevante Wirkmechanismen beschreiben, eine Verbreitung erfahren. Diese Modelle erfordern ein genaues Verständnis der im Bohrloch auftretenden Phänomene. Mit hochauflösenden numerischen Modellen kann dieses Verständnis erreicht werden. In dieser Arbeit werden sowohl die zur Validierung nötigen experimentellen Daten als auch die Bewertungen hochauflösender numerischer Modelle des Bohrkleintransports erarbeitet.

Im experimentellen Teil dieser Arbeit wird der Versuchsaufbau, eine vertikale “flow-loop” mit Bohrloch-Suspension zur Generierung von experimentellen Daten, vorgelegt. Der Versuchsaufbau besteht aus einem 64 mm dicken und 2.000 mm langen Rohr, medizinischem Weißöl- und kugelförmigen Glas-Partikel mit Durchmessern von 2 bis 6 mm. Das System stellt physikalische Phänomene ähnlich des Bohrkleintransports dar. Die “Particle Image Velocimetry” (PIV) und “Particle Tracking Velocimetry” (PTV) Techniken werden implementiert, um Geschwindigkeitsprofile von Fluid und Partikeln zu gewinnen sowie Histogramme der Partikelpositionen mono- und bidisperser Suspensionen. Dies wird durch den Abgleich des Brechungsindex von disperser und kontinuierlicher Phase sowie des Rohrmaterials erreicht. Die Ergebnisse zeigen die Bedeutung der Auftriebskraft für die Konfiguration der Partikelverteilung über den Rohr-Querschnitt. Diese Kraft bewirkt Partikelansammlungen an spezifischen radialen Positionen. Darüber hinaus wird in bidispersen Systeme eine erheblicher Impulsaustausch zwischen den betrachteten Partikeln beobachtet.

Der rechnerische Teil der Arbeit betrachtet die Simulation der “two-fluid”- Methode und des “Discrete Particle Model” (DPM) und überprüft ihre Gültigkeit für die Vorhersage des Bohrkleintransport. Die “two-fluid” Methode zeigt eine gute Übereinstimmung mit Experimenten mit monodispersen Systemen und liefert eine Erklärung für die in den Experimenten beobachteten Partikelansammlungen. Für polydisperse Systeme ist die “two-fluid”- Methode jedoch nicht geeignet. Auf der anderen Seite ist das hier implementierte DPM-Modell in der Lage experimentelle Ergebnisse bisdisperser Systeme für

Volumenkonzentrationen bis zu 3% zu reproduzieren. Für höhere Konzentrationen sollten erweiterte Modelle mit der Betrachtung von Teilchenkollisionen in viskosen Flüssigkeiten aufgenommen werden. Das DPM-Modell wird ausgewählt als die beste Alternative für Bohrklein-Transportprobleme. Für den Einfluss der Exzentrizität auf den vertikalen Partikeltransport wird eine Sensitivitätsanalyse durchgeführt. Die Analyse zeigt, dass die Auftriebskraft einen besseren Partikeltransport bewirkt, als den unter der Annahme homogener Partikelverteilung, die typischerweise in die Bohrtechnik angenommen wird.

Contents

Nomenclature

Acronyms

ACTM	Adaptive Collision Time Model
CFL	Courant-Friedrichs-Lewy
DEM	Discrete Element Method
DNS	Direct Numerical Simulation
DPM	Discrete Particle Method
EGS	Enhanced Geothermal Systems
gebo	Geothermal Energy and High Performance Drilling Research Program gebo
GUI	Graphical User Interface
HDR	Hot-Dry-Rock
HFR	Hot-Fractured-Rock
HPHT	High Pressure-High Temperature
HWR	Hot-Wet-Rock
LBM	Lattice Boltzmann Method
LSRV	Low Shear Rate Viscosity
OSF	Optimal Space-Filling
PDC	Polycristalline Diamond Compact
PIV	Particle Image Velocimetry
PLIC	Simple Line Interface Calculation
PSD	Particle Size Distribution
PTV	Particle Tracking Velocimetry

ROP	Rate of penetration
SLIC	Simple Line Interface Calculation
VOF	Volume of Fluid

Latin Symbols

A	Area open to flow, m^2
A_1	Cross-sectional area of layer 1, m^2
A_2	Cross-sectional area of layer 2, m^2
A_p	Cross-sectional area of the particle to the direction of the incoming flow
C	Average concentration
C_0	Feed concentration
C_{max}	Maximum Courant number
d_p	Particle diameter, m
d_c	Cuttings diameter, m
D_{eq}	Equivalent diameter, m
D_{hyd}	Hydraulic diameter, m
D_h	Diameter of wellbore, m
D_{plug}	Plug diameter, m
D_p	Diameter of drill pipe, m
E	Offset distance between axes of the drill pipe and the wellbore, m
e	Eccentricity
f_d	Drag force acting on an individual particle, N
F_g	Gravity force, N
$F_{\Delta P}$	Pressure gradient force, N
$f_{\nabla \cdot \tau}$	Viscous force acting on an individual particle, N
$f_{\nabla p}$	Pressure gradient force acting on an individual particle, N
f_B	Basset force acting on an individual particle, N
$f_{c,ij}$	Inter-particle elastic force, N

f_{cell}^{i}	Fractional volume of particle i residing in the cell under consideration
$f_{d,ij}$	Inter-particle damping force, N
F_{LS}	Saffman lift force, N
F_l	Gravity force, N
F_l	Lift force, N
f_{Mag}	Magnus force acting on an individual particle, N
$f_{pf,i}$	Particle-fluid interaction force, N
F_{pl}	Plastic force, N
f_{Saff}	Saffman lift force acting on an individual particle, N
F_{tot}	Interfacial momentum transfer per unit volume, N/m^3
F_{vm}	Virtual mass force, N
f_{vm}	Virtual mass force acting on an individual particle, N
G	Shear modulus, Pa
g	Gravity, m/s^2
h	Bed height, m
I	Identity matrix
I_i	Moment of inertia of the particle, kg m^2
$L_{1,in}$	Wetted perimeter, m
$L_{1,out}$	Wetted perimeter, m
L_{12}	Wetted perimeter of layer interface, m
$L_{2,in}$	Wetted perimeter, m
$L_{2,out}$	Wetted perimeter, m
m_i	Mass of the particle, kg
m_p	Particle mass, kg
$M_{r,ij}$	Friction component of the torque acting on the particle, Nm
$M_{t,ij}$	Tangential component of the torque acting on the particle, Nm
n	Number of particles in a particular cell

n_p	Number of spherical particles per unit volume
$P(r/R)$	Radial probability distribution function
P_s	Solids pressure, Pa/m^2
Q_c	Volumetric flow rate of the cuttings, m^3/s
Q_m	Volumetric flow rate of the mud, m^3/s
R_i	Radius of the particle, m
r_p	Particle radius, m
t	Time
$t_{contact,n}$	Contact time in the normal direction, s
$t_{contact,t}$	Contact time in the tangential direction, s
U	Drilling fluid velocity, m/s
U_1	Velocity of solid-liquid mixture in layer 1, m/s
u_f	Fluid velocity, m/s
u_p	Particle velocity, m/s
U_s	Average settling velocity in the axial direction, m/s
u_s	Slip velocity, m/s
U_a	Average annulus velocity, m/s
U_{l2}	Friction velocity at layer interface, m/s
U_{mix}	Mixture velocity, m/s
U_{plug}	Average plug velocity, m/s
U_{s2}	Velocity of solid in layer 2, m/s
U_{sa}	Average settling velocity in the annular region, m/s
U_{splug}	Average settling velocity in the plug region, m/s
v_i	Translational velocity of the particle, m/s
V_p	Volume of the particle, m^3
v_{*C}	Critical wall friction velocity, m/s
V_{cell}	Volume of the cell, m^3

v_{n0}	Centerline velocity of a Newtonian fluid at the volumetric rate obtained in a particular experiment
W	Annular gap at the lowest position, m
K	Consistency index, Pa·s^n
YP	Yield point, Pa

Greek Symbols

ϕ_i	Bulk volume fraction
α	Wellbore angle, rad
β	Momentum transfer coefficient
β_{exp}	Volumetric expansion coefficient, 1/K
β_{LS}	Ratio of the shear flow Reynolds number and the particle Reynolds number
β_{MT}	Interphase momentum transfer coefficient
η	Dynamic viscosity, Pa·s
Γ_{dep}	Deposition mass flux per unit length, (kg/s)/m
Γ_{ent}	Entrainment mass flux per unit length, (kg/s)/m
λ	Friction factor
λ_{plug}	Plug diameter ratio
μ	Dynamic viscosity, Pa·s
μ_l	Dynamic viscosity of the liquid, Pa·s
μ_a	Apparent viscosity, Pa·s
μ_s	Shear solids viscosity, Pa/m^2
ν_2	Poisson ratio, -
ω_l	Vorticity of the liquid, 1/s
ϕ	Volume fraction
ϕ_{rep}	Angle of repose, rad
Π	Dimensionless group
Ψ	Sphericity

ρ	Density, kg/m^3
ρ_c	Cuttings density, kg/m^3
ρ_f	Fluid density, kg/m^3
ρ_p	Density of the particle, kg m^{-3}
τ_1	Shear stress of layer 1 against the wall, N/m^2
τ_2	Shear stress of layer 2 against the wall, N/m^2
τ_{12}	Interfacial shear stress between layer 1 and 2, N/m^2
τ_l	Liquid phase stress tensor, Pa/m^2
τ_s	Solids phase stress tensor, Pa/m^2
τ_{wc}	Wall shear stress, Pa
Θ_h	Angle defined in
Θ_p	Angle defined in
ζ_s	Bulk solids viscosity, Pa/m^2
v_i	Rotational velocity of the particle, rad/s

Subscripts

i	Index of the particle considered
j	Index of the particle interacting
f	Fluid
g	Gravity
l	Liquid
p	Particle
ph	Considered phase (solid, liquid, ...)
s	Solid

Superscripts

T	Transposed

Dimensionless Groups

A_c	Acceleration number

C_d	Drag coefficient
C_{LS}	Saffman lift coefficient
C_{vm}	Virtual mass coefficient
Re_p	Particle Reynolds number
Re_S	Shear flow Reynolds number

Other Symbols

$\Delta t_{coupling}$	Time-step of the coupling, s
Δt_{flow}	Time-step of the flow, s
Δt_{soft}	Time-step of the particles in soft collision model, s
ΔV	Volume of a computational cell, m^3
Δx_i	Length interval or size of the cell along every coordinate, m

1 Motivation and goal of this thesis

Geothermal energy is energy stored as heat under the solid surface of the earth. Of this energy, around 30% consists of residual heat produced during the formation of the earth. The source of this residual heat was the kinetic energy from material agglomerating 5 milliards (5×10^9) years ago to form the earth. The remaining 70% is generated by the radioactive decay of the isotopes potassium 40, uranium 235, uranium 238 and thorium 232. These continuously produce heat inside the earth [1]. Strictly speaking, geothermal energy cannot be considered as a renewable source of energy. However, the amount of energy stored is of such quantity that it could cover human demands for thousands of years. This fact converts geothermal energy in a good alternative to fossil fuels and nuclear energy.

Mankind has dealt with geothermal energy since the Paleolithic era, 2.6 million years ago. Most commonly on spots where the geologic conditions are favourable. Such spots are characterized by a thin earth crust where the contact of aquifers with hot and permeable geologic formations makes hot water easily available at the surface. These are typically found in active volcanic regions, e.g., in Iceland, the Yellowstone National Park in USA or the Valley of Geysers in Russia to name some where the rare Geyser phenomenon is observed. In several other locations hot water springs are available and have been used by humans as hot baths or even house heating. If aquifers are not close to the surface it is possible to reach them through deep well-bores. Such kind of resources are called hydrothermal systems and are not the rule, but peculiar cases. Most of the geothermal energy within the reach of current drilling technology is situated at less convenient locations, where no aquifers and low permeability are found. For this reason, several initiatives are developing new technologies able to harness geothermal energy by stimulating essentially dry and low permeable formations. Such resources are known as petrothermal, also known as Hot-Dry-Rock (HDR), Hot-Wet-Rock (HWR), Hot-Fractured-Rock (HFR) or Enhanced Geothermal Systems (EGS).

When not close to active volcanic regions, both the hydrothermal and the petrothermal resources require the drilling of deep well-bores. To guarantee productivity the construction of such well-bore is designed to meet natural crack systems in the formation, which increase the heat transfer surface in the underground. When these are not available, production of artificial cracks is also possible. Current drilling technology is specially adapted to the oil and gas industries. Oil and gas well-bores have the objective to connect the natural mineral deposits with the facilities at the surface during the exploitation period. This is basically the same target as in geothermal well-bores. Specially when considering the exploitation of hydrothermal systems at depths between 3,000 and 4,000 meters. In the case of petrothermal systems, where the heat is extracted from "hard rock" formations, there exist substantial differences:

- The average temperature is larger
- The target formations are not relatively soft mineral deposits, but hard rock
- For the operation of the system, natural or artificial stable and large area cracks are necessary
- To reduce the hydraulic pressure losses, production and injection well-bores with large diameters are necessary
- The average depth is larger

For these constraints it is necessary to find new solutions. Simultaneously the costs must be reduced. The typical costs of 5,000 meter and deeper well-bores are at this time between 2.5 and 3 million euros per 1,000 meters. Therefore, the profitability of geothermal systems is not assured.

In order to improve current drilling technology applied to geothermal targets, the German state of Lower Saxony started the gebo research initiative. This one had the aim to propose new solutions for the production of geothermal energy in the North German region. The project was divided in four research directions considered relevant for the development of geothermal energy: (1) geological systems, (2) drilling technology, (3) materials and (4) electronic systems. The research performed within gebo had the following objectives:

- Reducing drilling costs
- Increasing the safety of the drilling technology in hot hard rock formations
- Reducing the financial risks

Within these objectives the present work was part of the drilling technology research direction. This was divided in several projects, from which this work took care of the cuttings transport problem. This is the subject of the following section.

1.1 The cuttings transport problem [1]

A crucial task during the construction of a well is the extraction of the drilled material, known as cuttings. The removal of these cuttings essentially creates the hole and allows the drilling bit to come in direct contact with the bottom of the hole. To accomplish this

---

[1] Part of this description was published in the OIL GAS European Magazine 1/2014 as a shortened version of a lecture presented at the Conference “Celle Drilling 2013” [2].

task drilling fluid is pumped down through the drill pipe to the drill bit, and flows up within the annular gap between the drill pipe and the well walls. The upward moving flow through the annulus transports the cuttings. Furthermore, the drilling fluid plays other important roles such as the control of the pressure within the well or the cooling of the drilling bit. The harsh and complex conditions within the well-bore difficult the complete monitoring of the drilling operation through measuring equipment. Therefore, modelling approaches are applied to supplement important information characterizing the progress of the process. Traditionally, steady-state models based on empirical correlations have been used to determine operational parameters [3]. These are mainly focused on the determination of a minimum transport velocity and the corresponding friction losses. The typical operating velocity recommended is between a range of 2 and 6 times the settling velocity of the largest particles [4]. This lack of accuracy has important safety and energy consumption implications. Furthermore, a proper representation of the transport condition requires an improved understanding of the phenomena affecting it. There is a significant difference between predicting a minimum velocity to transport material and predicting the actual transport velocity of the material. While the former leaves room for safety factors, the latter requires the best possible precision.

In the drilling industry the efficiency of the operation depends "on a considerable number of interacting processes in which the drilling fluid plays a central role". This was stated by Swanson [5] more than 20 years ago in the context of conventional drilling methods used for vertical shallow well-bores. Today, due to the increasing requirements, drilling is even more challenging. This is due to the High Pressure-High Temperature (HPHT) conditions, such as in deep geothermal drilling beyond depths of 6,000 m. At these conditions, the rheological properties of the drilling fluids change considerably and in consequence, the hole cleaning process is affected. In directional drilling the main challenge is the lack of generalized and reliable models for the transport characteristics of drill cuttings. As a result, cutting beds may form and potentially increase the risk of clogging. Besides this, drilling is a dynamic process. For larger time scales this is due to the passage through different geological formations with varying rates of penetration and due to intermittent operations. For small time scales, this is due to the orbit eccentricity of the rotating drill string or geometric entities causing unsteadiness of the flow. Merely due to the transport of drill cuttings additional flow instabilities may occur. In particular in geothermal drilling, these issues have to be assessed in view of the huge financial risk of the entire drilling project. In order to support decision making, simulations based on suitable models are extremely valuable.

1.2 Multiscale modeling approach

Drilling hydraulic models are supposed to predict pressure and temperature, velocities of the phases present as well as hold-up and bed heights in the well. Thus, appropriate models need to consider at least two phases: (1) the drilling fluid as a continuous phase with a shear-, temperature- and time-dependent rheology and (2) the cuttings as a dispersed phase, which may have a wide particle size distribution, various shapes and densities. Particle size and concentration are crucial parameters because they determine the transport characteristics of the particles in the continuous phase. This defines the appropriate modelling concept. Finally, gravity determines the flow regimes found in the wellbore as a function of deviation.

From a physical point of view, the hole cleaning process in the drilling industry features a number of various phenomena, including amongst others the complex rheology of the drilling fluids, multi-phase transport as well as thermal transport. Different approaches are necessary to model these phenomena with an appropriate level of detail, i. e., at different length scales. Subsequently, scale bridging attempts to determine properties of the system behaviour on a coarser scale, using information of models from smaller scales. At the top level the whole trajectory of the well bore is considered. Here, usually one-dimensional approaches are employed, such as the drift-flux or three-layer models, which allow the evaluation of global input/output at moderate computational costs. However, these models require constitutive equations or closure relations, which are usually obtained in laboratory experiments. Here, the motion of the continuous phase, the transport characteristics of the granular particles, as well as various forms of interactions between the phases are modelled. In that respect, in the case of multiphase flows in non-Newtonian liquids a lack of knowledge prevails. To elucidate these problems is part of the motivation of this thesis.

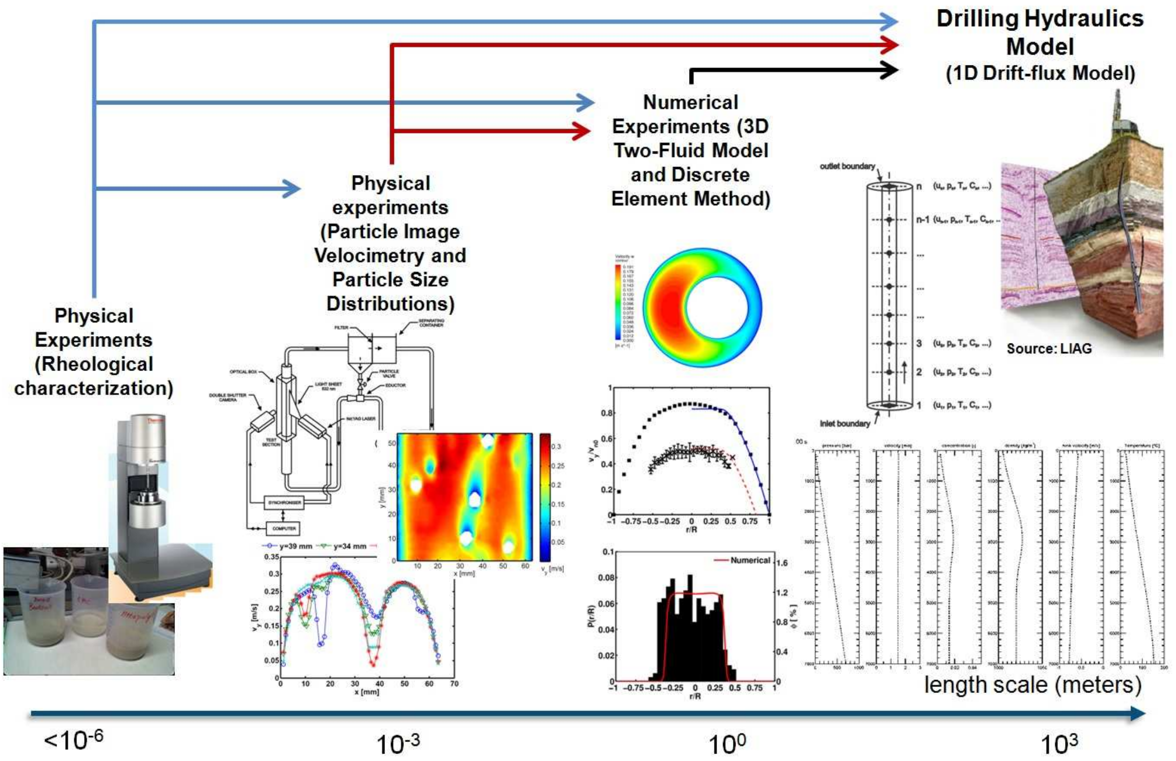

Figure 1.1: Different objects of interest in the drilling hydraulics problem.

1.2.1 Large scale: trajectory of the well

Large scale modelling aims at a virtual representation of the complete well-bore with different objectives such as: (1) safety studies and accident scenarios, (2) design and development of devices, (3) optimization of operational criteria and (4) monitoring or steering by simulation. At this scale, necessary input parameters are: (1) flow rate, (2) properties of the drilling fluid, (3) amount of solids to be carried (ROP variation), (4) formation temperature distribution and (5) progression in the hole cleaning process. Correspondingly, the output is: (1) the velocity of the various phases, (2) pressure, (3) hold-up, (4) fluid temperature and (5) bed height in case of horizontal drilling.

The transport in the whole trajectory of the well is modelled based on one-dimensional transient transport models coupled with transient thermal models considering the temperature distribution of the formation. A bi-directional coupling of the transport and thermal model is accomplished through the diffusive and convective transport in the fluid flow. The drift-flux model is used to determine the transport of the disperse phase. This approach requires friction factors to model viscous effects in the well-bore. The prediction of the particle concentration and holdup relies on parameters, which require the analysis of meso-scale simulations.

1.2.2 Meso scale: wellbore diameter

At the diameter scales, the main objective of the simulations is to generate data for models applied at larger scales. However, operational criteria may still be inferred through these methods. Similar to the approach presented above, inputs and outputs have to be defined. At this scale, necessary input parameters include: (1) phase properties, (2) eccentricity, (3) drill string angular velocity. Outputs are: (1) fluid and cuttings flow fields, (2) pressure gradient, (3) concentration distributions and (4) bed height.

In drilling hydraulics, sections of the well-bore may be modeled using CFD (computational fluid dynamics). Such models allow determining details of the flow fields at single planes or smaller sections of the pipe. Depending on geometrical parameters such as the diameter ratio of drill string and casing and the eccentricity, the non-dimensional pressure gradient λ is determined. This parameter among others are entered in the above large scale models. The results of these models require validation with measurements, where average velocities of fluid and particles and particle distributions need to be obtained. The intention in the gebo project was to supplement the physical experiments with numerical experiments and generate the parameters for the drift-flux model through numerical simulations. The first task was the location of numerical models able to supply the necessary information. Two main options were found: (1) the two-fluid model and (2) CFD coupled with discrete element methods (DEM), where the flow around the particles was not resolved.

The two-fluid model or its more general version the multi-fluid model is an Eulerian-Eulerian representation of multi-phase flows. The abstractness comes from the fact, that this is done also in the case of solid-liquid suspensions where the dispersed phase are the solid particles. One of the first authors to implement it for two-phase flow simulations was Ishii in 1975 [6]. On the other hand, the coupling between CFD and DEM is a an Eulerian-Lagrangian approach, where the fluid is still treated through an Eulerian reference and the particles motion is described in a Lagrangian frame. DEM was firstly introduced by Cundall and Strack [7] on 1979, who named it distinct element method. In both cases the models still rely on closure relations to determine momentum transfer between phases, therefore are not fully predictive.

1.2.3 Small scale: particle diameter

At particle scales, simulations able to resolve flow fields around the particles allow specification of drag and lift coefficients as a function of fluid and particle properties and the system configuration. The specification of drag forces of particles is necessary in large and meso-scale models to determine settling velocities. Furthermore, lift forces are required to determine the distribution of particles across sections and the capacity of drilling fluids to entrain particles in deviated sections. Necessary inputs are: (1) non-Newtonian rheology, (2) particle size distributions and (3) particle shapes. Outputs from these models include: (1) drag coefficients, (2) lift coefficients or (3) plastic force, described by Clark and Bickham [8] as "the force required to lift a cutting from a stagnant layer of drilling mud".

1.3 Aim and outline of this thesis

This thesis focuses on the first step of the multiscale modeling approach: provision of detailed empirical data quantifying momentum transfer in solid-liquid bidisperse suspensions. Due to the fundamental nature of the research, results and conclusions extracted from this thesis may be used in other industrial applications.

Several open questions exist in the field of solid-liquid suspensions. From those, we concentrate on polydispersity. This is related to the different particle sizes generated during the drilling of a geologic formation. The study of polydispersity needs to clarify its effects on drag and lift forces, which determine important parameters as the settling velocities and the cross-sectional distributions of the particles. Likewise, it serves as a reference for numerical modeling validation. The work uses laminar flows in a vertical tube to concentrate on the main subject and avoid interferences of turbulence. The studies are carried out using medicinal white oil, which presents Newtonian rheology.

In the following chapter, the state of the art in cuttings transport with special emphasis on modeling and its research needs is given. After that, a chapter dedicated to the experimental setup and the measurement system is included. The next chapter focuses on the two numerical approaches selected to simulate the cuttings transport problem at the diameter scale. The experimental results are separated between those corresponding to monodisperse suspensions and those corresponding to bidisperse suspensions. After these results are introduced, a comparison with the previously presented numerical methods follows. At the end of this same chapter, a sensitivity analysis to investigate the effects of eccentricity on cuttings transport is also presented. Conclusions and recommendations are given in the final chapter.

2 State of the Art

> *"If I have seen further, it is by standing on the shoulders of giants."*
>
> - Sir Isaac Newton

In this chapter the state of the art in relation to the cuttings transport problem is presented. It starts with a brief introduction of specific models for the prediction of cuttings transport. Following, basic definitions of the forces acting on particles and necessary developments are presented. After that, experimental methods able to measure the flow of solid-liquid suspensions are reviewed to show different possibilities to supply high quality data for numerical validation. Finally, a review of numerical methods for the simulation of multiphase flows is given.

2.1 Cuttings transport modeling

"Even though hole cleaning is much less of a problem today than it was 10 or 20 years ago, i.e., today there is a lower percentage of stuck pipes and lost wells, the way that it is currently handled is still very costly. Frequent wiper trips, reaming and/or washing to the bottom, maximum pumping rates, etc., although prudent at this time, are in fact lost time and money caused by the inadequacy of current technology in cuttings transport. Considering that the need for directional and horizontal drilling, both in numbers and extent, grows constantly, research into the hole cleaning problem would be a prudent investment."

Pilehvari, A.A., Azar, J.J. and Shirazi, S.A. (1999): State-of-the-Art Cuttings Transport in Horizontal Wellbores. *SPE Drilling & Completion*, Vol. 14, 196-200.

The observation of Pilehvari et al. [9] points out the potential for improvement in hole cleaning. Through monitoring of the process outputs and internal states, and control of the process inputs, more efficient hole cleaning could be achieved. Nazari et al. [10] proposed a systematic approach describing the necessary improvements in order to realise automation of the hole cleaning process. To make it possible two main directions were recommended: (1) development of real-time measurements and (2) development of a generalized systematic model for hole cleaning not yet available.

Two types of models may be developed: empirical correlations and mechanistic models. The former are based on direct observation and measurement, which supply relationships among experimental data. The latter are based on the underlying causal mechanisms responsible of a system's behaviour. Empirical correlations or models present less complication in its derivation, but the accuracy of their predictions is limited to systems similar to those used during the experiments. On the other hand, mechanistic models require more involved analysis, but these are capable of dealing with a broader range of situations and are, therefore, more flexible.

2.1.1 Empirical correlations by Luo *et al.*

Luo *et al.* [11] developed empirical correlations based on the forces acting on the cuttings and the associated dimensionless groups for deviated wells in order to find critical flow rates. The analysis starts by differentiating the forces acting on the cuttings:

1. Forces which tend to hold the cuttings in the bed (gravitational force & frictional force).
2. Forces which tend to move the cuttings out of the bed (lift force & drag force).

Then, the different transport modes or flow patterns were analysed considering the previous forces.

1. Heterogeneous suspension. When the flow rate is high, the cuttings are kept in suspension due to the lift force, which compensates the gravitational force component.
2. Separated beds/dunes. For lower flow rates or larger hole angles, the lift force cannot keep the cuttings in suspension but the drag force is strong enough to drag the cuttings forward. The flow pattern is thought to be a combination of the lift force and the drag force.
3. Continuous moving bed. Only the drag force moves the cuttings forward.

For the mathematical modelling Luo *et al.* [11] selected 7 independent variables:

1. μ_a, apparent viscosity.
2. ρ_f, density of the fluid.
3. d_c, diameter of the cuttings.
4. ρ_c, density of the cuttings.
5. $W = \frac{D_h - D_p}{2} - E$, annular gap at the lowest position, where D_h and D_p are diameters of wellbore and drillpipe, respectively, and E is the offset distance between the axes of the drill pipe and the wellbore.
6. $g\ (\rho_c - \rho_f)\ sin\ \alpha$, gravitational force component against the cuttings' lifting up from the wellbore surface, where ρ_c is the density of the cuttings and α the wellbore angle.

7. $v_{*C} = (\frac{\tau_{wc}}{\rho_f})^{0.5}$, critical wall friction velocity, where τ_{wc} is the wall shear stress.

However, they pointed out that two important variables as ROP and drillpipe rotation were not considered. In the case of the ROP, they proposed to introduce correction correlations. In the case of drillpipe rotation, they observed a small effect on the critical flow rate and therefore neglected it. From the previous listed variables four dimensionless groups were derived using the Buckingham PI theorem:

1. Dimensionless group Π_1:
$$\Pi_1 = \frac{v_{*C}^2}{d_c g(\rho_c - \rho_f) sin\alpha} \tag{2.1}$$
This dimensionless group expresses the ratio of the fluid dynamic force (lift/drag) to the effective gravitational force.
2. Dimensionless group Π_2:
$$\Pi_2 = \frac{d_c v_{*C} \rho_f}{\mu_a} \tag{2.2}$$
This dimensionless group is considered as a particle Reynolds number.
3. Dimensionless group Π_3:
$$\Pi_3 = \frac{d_c}{W} \tag{2.3}$$
This dimensionless group reflects the influence of the cuttings size relative to the size of the annular gap.
4. Dimensionless group Π_4:
$$\Pi_4 = \frac{\rho_f}{\rho_c} \tag{2.4}$$
This dimensionless group expresses the influence of the inertia force when the cuttings accelerate upon starting to move.

Luo *et al.* [11] neglected Π_3 and Π_4 because they found, through experimental tests in large flow loops, that these dimensionless groups have small effects in comparison to Π_1 and Π_2. Hence, they obtained the following expression to describe the critical condition for initiation of cuttings transport:

$$\Pi_1 = a\ \Pi_2^b \tag{2.5}$$

Coefficients a and b were obtained based on regression analysis. By using this model, Luo *et al.* [11] obtained an average percentage difference between the predicted and the experimental data of 15,9 %. These coefficients need to be defined on the basis of the particular conditions found in a drilled wellbore. Therefore, are system dependent.

2.1.2 Mechanistic models by Clark and Bickham

Clark and Bickham [12] defined three clear pattern transitions depending on the wellbore angle. For high angles, transport is via a rolling mechanism; at intermediate angles, transport is via a lifting mechanism, and at near-vertical angles, particle settling determines transport. The dominating mechanisms in each range are used to predict cuttings bed heights and annular cuttings concentrations as functions of operating parameters (flow rate, penetration rate), wellbore configuration (depth, hole angle, hole size, pipe size), fluid properties (density, rheology) and cuttings characteristics (density, size, bed porosity, angle of repose). Table 2.1 from Robinson [13] shows the different zones and puts them in relation to occurring physical phenomena and critical parameters for cuttings transport. A draw back from the mechanistic models developed by Clark and Bickham [12] is that pipe eccentricity and rotary speed are not taken into account.

Hole Angle	Critical Parameters (in order of importance)	To improve hole cleaning	Cuttings Transport Mechanism
Zone I 0° - 35° Vertical wells	1. flow rate/annular velocity 2. Rheology (YP, or better yet, K) 3. ROP	Increase Increase Decrease	Particle settling velocity
Zone II 35° - 65° (Low deviated wells)	1. flow rate/annular velocity 2. Drill string rotational rate 3. Rheology(6rpm/LSRV and PV) 4. ROP	Increase Increase flatten Profile Decrease	Lifting
Zone III 65° + (High deviated wells)	1. Bit cutter size (PDC)/cutting size 2. Drill string rotational rate 3. flow rate/annular velocity 4. Rheology (6rpm/LSRV and PV) 5. ROP	Decrease Increase Increase flatten Profile Decrease	Rolling

YP = yield point; K = consistency index; LSRV = low shear rate viscosity; PDC = polycrystalline diamond compact.

Table 2.1: Different hole zones and parameters affecting hole cleaning [13].

2.1.2.1 Five Percent Maximum Concentration Model

This model is applied on vertical sections of the well, that is, Zone I in table 2.1. It determines the annular velocity required to limit the suspended cuttings concentration to five percent by volume in the flowing mud stream. Therefore, it is based on the mechanisms determining slip of one phase with respect to the other also known as holdup. The area which is open to flow is characterized as a tube instead of an annulus. This simplifies the wellbore geometry. The tube diameter is based on the hydraulic diameter for pressure drop calculations and on the equivalent diameter for velocity calculations. Since drilling mud often exhibits a yield stress, Clark and Bickham [12] consider that there may be a region, near the center of the cross section, where the shear stress is less than the yield stress. There, the mud moves as a plug, i.e., rigid body motion as shown in figure 2.1. In the annular velocity around the plug, the mud flows with a velocity gradient and behaves as a viscous fluid.

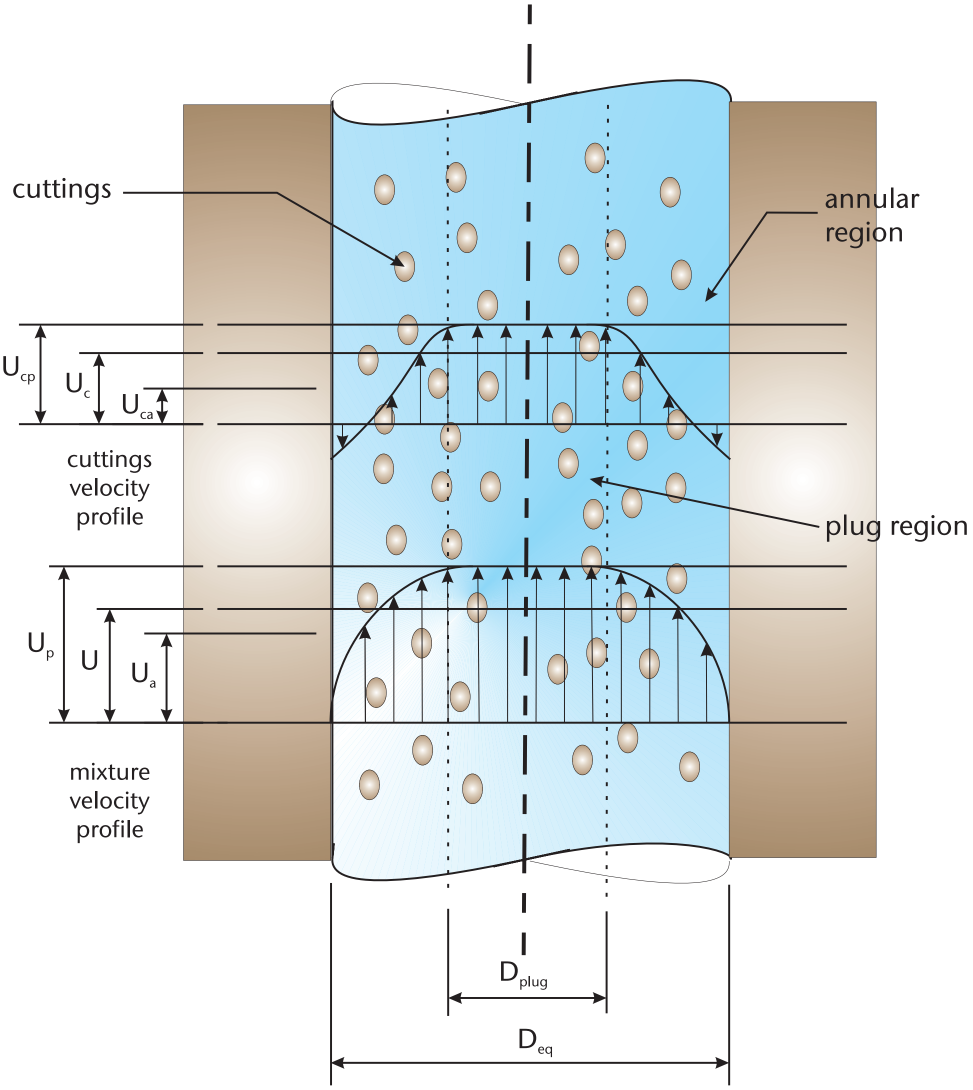

Figure 2.1: Mixture and cuttings velocity for a Herschel-Bulkley laminar flow after Clark and Bickham [12], where U_{cp} is the cuttings velocity in plug, U_c the cuttings average velocity, U_{ca} the cuttings velocity in the annulus, U_p the mixture velocity in the plug, U the mixture average velocity and U_a the mixture velocity in the annulus.

The hydraulic diameter is defined as four times the flow area divided by the length of the wetted perimeter

$$D_{hyd} = \frac{4 \times \text{cross-sectional area}}{\text{wetted perimeter}}. \tag{2.6}$$

This relationship can be used to determine the hydraulic diameter of the area open to flow above the cutting bed. For the wellbore annulus, the hydraulic diameter of the wellbore cross section (with no cuttings present) is

$$D_{hyd} = D_h - D_p, \tag{2.7}$$

where D_h is the wellbore diameter and D_p is the outer diameter of the drill-string. The equivalent diameter is defined as:

$$D_{eq} \equiv \sqrt{\frac{4A}{\pi}}, \tag{2.8}$$

where A is the area open to flow. For the wellbore annulus, the equivalent diameter is

$$D_{eq} = \sqrt{D_h^2 - D_p^2}. \tag{2.9}$$

The plug diameter ratio is

$$\lambda_p = D_{plug}/D_{eq}. \tag{2.10}$$

The mixture velocity is

$$U_{mix} = \frac{Q_c + Q_m}{A}, \tag{2.11}$$

where Q_m is the volumetric flow rate of the mud and Q_c is the volumetric rate of the cuttings which depends on the bit size and the penetration rate. In addition, U_{mix} can be calculated from U_{plug} the average plug velocity and U_a the average annulus velocity in the equivalent pipe.

$$U_{mix} = U_a(1 - \lambda_{plug}^2) + U_{plug}\lambda_{plug}^2 \tag{2.12}$$

The feed concentration is defined as

$$C_o = \frac{Q_c}{Q_c + Q_m} \tag{2.13}$$

and the average concentration, C, of cuttings in a short segment with length, Δz, and cross-sectional area, A, can be calculated as

$$C = C_a(1 - \lambda_p^2) + C_p\lambda_{plug}^2. \tag{2.14}$$

Here Clark and Bickham [12] assume that the suspended cuttings concentrations are uniformly distributed across the area open flow, but indicate that this assumption affects in an ostensible manner the results. For this reason, they indicate that research is required to determine cuttings concentrations as a function of well-bore geometry, mud properties, cuttings properties, and operating conditions. *This statement is one of the main inspirations for this thesis.* From the previous assumption the following equation is obtained

$$U_{mix} = \frac{C\ U_s(1-C)}{C - C_o} \tag{2.15}$$

with

$$U_s = U_{sa}(1-\lambda_{plug}^2) + U_{splug}\lambda_{plug}^2, \tag{2.16}$$

where U_s is the average settling velocity in the axial direction, U_{sa} is the average settling velocity in the annular region and U_{sp} is the average settling velocity in the plug region. The components of the settling velocities in the annular and the plug regions can be calculated following a procedure by Perry and Chilton [14], where the drag coefficient of a sphere, the yield stress of the mud and the apparent viscosity of the mud at a shear rate resulting from the settling cutting between other parameters are taken into account.

The value calculated using eq. 2.15 is the minimum acceptable mixture velocity required for a cuttings concentration C. Piggot [15] recommended that the concentration of suspended cuttings be a value less than five percent. With this limit ($C = 0.05$), eq. 2.15 becomes

$$U_{mix} \geq \frac{0,0475\ U_s}{0,05 - C_o} \tag{2.17}$$

This implies that the penetration rate must be limited to a rate that satisfies this inequality.

2.1.2.2 Equilibrium Cuttings Bed Height Models

Clark and Bickham [12] depict a stationary cuttings bed formed in an inclined well with a wellbore angle α here showed in figure 2.2. They consider that when the well-bore complementary angle $90° - \alpha$ is less than the angle of repose ϕ_{rep}, a stationary bed forms and the cuttings can only be rolled or lifted.

The dynamic forces need to be calculated as a function of local drilling fluid velocity U, then the drilling fluid flow rate needed to take the particles away can be determined.

Lifting mechanism: The lifting mechanism is observed in intermediate well-bore angles. In this case, the cuttings are not moving while resting on the well-bore wall. Only when the lift force is sufficient, the cuttings move up into the region where the drilling

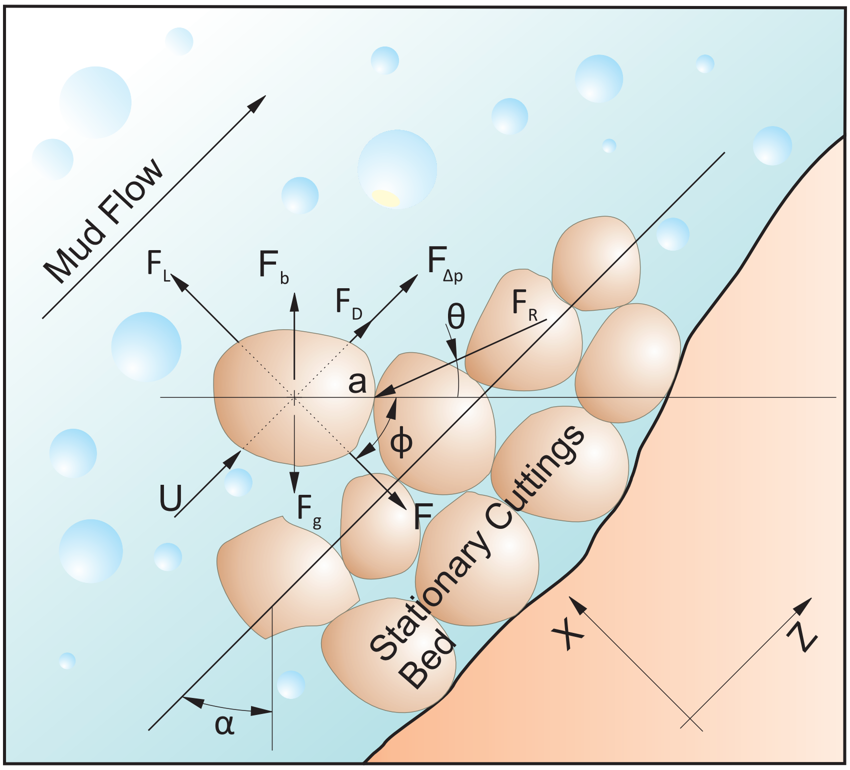

Figure 2.2: Forces acting on a settled cutting after Clark and Bickham [12].

fluid carries the cutting downstream. In order to find the necessary lift force, Clark and Bickham [12] developed the following force balance equation :

$$F_l - F_{pl} + (F_b - F_g)\ sin\ \alpha = 0 \tag{2.18}$$

where F_l is the lift force, F_{pl} is the plastic force, $F_{\Delta P}$ is the pressure gradient force, and F_g is the gravity force. As soon as the particle approaches the drilling fluid velocity, the lift force decreases and the particle settles back towards the well-bore. This process is periodically repeated.

Rolling-Mechanism: In the case of the rolling mechanism, a moment balance is required. The moments due to forces are summed around a support point a located between the considered cutting and the cuttings bed.

$$|x|(f_d + F_{\Delta P}) + |z|(F_l - F_{pl}) + l(F_b - F_g) = 0 \tag{2.19}$$

where length l is equal to

$$l = |z|(sin\ \alpha + cos\ \alpha / tan\ \phi) \tag{2.20}$$

The dynamic forces must exceed the static forces for rolling to take place. Several auxiliary equations are needed to solve the equations used for the lifting and rolling mechanism.

Some of these equations are commonly used in fluid mechanics with the correspondent coefficients: the drag force, the lift force, the buoyancy force and the gravity force. The rest is commonly used in soil erosion and slurry transport (e.g. the plastic force). A full definition of all the forces can be found in section 2.2.

2.1.2.3 Necessary parameters for the Clark and Bickham Model:

As mentioned earlier, these models are developed without considering eccentricity and rotation of the drilling pipe. Hence, these need to be validated for such cases. Furthermore, drag and lift coefficients need also to be worked further. More specifically, it would be interesting to obtain the previous coefficients for non-Newtonian moving fluids. Until now work has been done on drag coefficients in quiescent non-Newtonian fluids. Chabra [16] has extensive references on this matter. Lift coefficients are taken from works by Saffman [17]. However, good-quality experimental data is necessary for the models validation.

2.1.3 Two- and Three layer models

The two- or three layer modeling is an approach taken by several investigators working with cuttings transport problems. These models are based on the models proposed for solids transport in pipes by Doron *et al.* [18]. As stated by Kelessidis *et al.* [19]: "The models are based on mass-balance equations for solids and liquid together with momentum balance equations for the two or three layers, resulting in a system of coupled algebraic equations". In order to solve the equations, closure relationships describing the interaction of the two phases are needed. Kelessidis *et al.* [19] point out that the various approaches in the use of the closure relationships is the major difference between the models. Likewise, Pilehvari *et al.* [9] indicate difficulties in determining these closure relationships, but remind of the advantages of using phenomenological models. Furthermore, according to Ozbayoglu *et al.* [20] and Cayeux *et al.* [21] a mechanistic relation including the effects of rotation and inclination is still not available. Such relations could be developed with detailed numerical simulations. The two-layer model is briefly introduced in the following section according to the work of Naganawa and Nomura [22] to show which information is required.

2.1.3.1 Two-layer model:

The Two-Layer model considers a layer with suspended solids and a layer with particles on the bottom of the well bore that may be moving as shown in figure 2.3. Six mass and momentum equations described below are simultaneously solved for six unknown independent variables: velocity of the solid-liquid mixture in layer 1 U_{l1}, velocity of liquid in layer 2 U_{l2}, velocity of solid in layer 2 U_{s2}, pressure p, volume fraction of solid in layer 2 C_{s2} and layer 2 cross-sectional area A_2.

The mass balance for layer 1 of solid-liquid mixture is expressed as

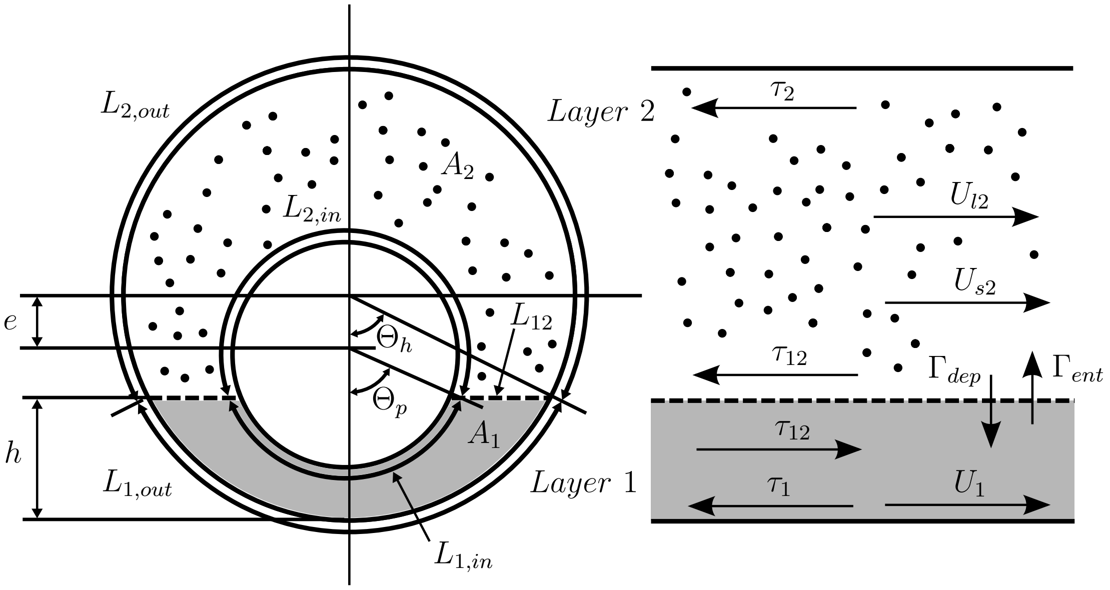

Figure 2.3: Schematic representation of the two-layer model.

$$\frac{\partial}{\partial t}(A_1\rho_1U_1) + \frac{\partial}{\partial s}(A_1\rho_1U_1) = (\Gamma_{dep,s} + \Gamma_{dep,l}) - (\Gamma_{ent,s} + \Gamma_{ent,l}), \tag{2.21}$$

for solid phase in layer 2,

$$\frac{\partial}{\partial t}(C_{s2}A_2\rho_s) + \frac{\partial}{\partial s}(C_{s2}A_2\rho_sU_{s2}) = \Gamma_{ent,s} - \Gamma_{dep,s}, \tag{2.22}$$

and for liquid phase in layer 2,

$$\frac{\partial}{\partial t}(C_{l2}A_2\rho_l) + \frac{\partial}{\partial s}(C_{l2}A_2\rho_lU_{l2}) = \Gamma_{ent,l} - \Gamma_{dep,l}, \tag{2.23}$$

where A_1 is the layer 1 cross-sectional area, ρ_1 is the density of solid-liquid mixture in layer 1, ρ_s is the density of the solid phase, ρ_l is the density of the liquid phase, s is the coordinate along the wellbore and $\Gamma_{ent,s}$, $\Gamma_{dep,l}$ and $\Gamma_{ent,l}$ are the mass transfer rates between layers. Naganawa and Nomura [22] propose preliminary mass transfer rates not including the effects of eccentricity and rotation. Considering the recognized significance of both parameters, it would be desirable to develop correlations able to include them.

Furthermore, the momentum equation for layer 1 of solid-liquid mixture is expressed as

$$\begin{aligned} \frac{\partial}{\partial t}(A_1\rho_1U_1) + \frac{\partial}{\partial s}(A_1\rho_1U_1U_1) = -A_1\left(\frac{\partial p}{\partial s} + \rho_1 g cos\ \alpha\right) - L_1\tau_1 \\ + L_{12}\tau_{12} - F_1 + U_{s2}\Gamma_{dep,s} + U_{l2}\Gamma_{dep,l} - U_l(\Gamma_{ent,s} + \Gamma_{ent,l}), \end{aligned} \tag{2.24}$$

for solid phase in layer 2,

$$\begin{aligned}\frac{\partial}{\partial t}(C_{s2}A_2\rho_s U_{s2}) + \frac{\partial}{\partial s}(C_{s2}A_2\rho_s U_{s2}U_{s2}) = -C_{s2}A_2\left(\frac{\partial p}{\partial s} + \rho_s g cos\ \alpha\right)\\ - C_{s2}(L_2\tau_2 + L_{12}\tau_{12}) + F_{sf} + U_1\Gamma_{ent,s} - U_{s2}\Gamma_{dep,s},\end{aligned} \tag{2.25}$$

and for liquid phase in layer 2,

$$\begin{aligned}\frac{\partial}{\partial t}(C_{l2}A_2\rho_l U_{l2}) + \frac{\partial}{\partial s}(C_{l2}A_2\rho_s U_{l2}U_{l2}) = -C_{l2}A_2\left(\frac{\partial p}{\partial s} + \rho_l g cos\ \alpha\right)\\ - C_{l2}(L_2\tau_2 + L_{12}\tau_{12}) - F_{sf} + U_1\Gamma_{ent,l} - U_{s2}\Gamma_{dep,l},\end{aligned} \tag{2.26}$$

where α is the wellbore angle, L_1 is the internal and external layer 1 wetted perimeter, τ_1 the shear stress of layer 1 against the wall, L_{12} the wetted perimeter of layer interface, τ_{12} the interfacial shear stress between layer 1 and 2, F_1 is the dry friction force per unit length, L_2 is the internal and external layer 2 wetted perimeter, τ_2 the shear stress of layer 2 against the wall and F_{sf} the multiparticle drag force per unit length. Again here, effects of eccentricity and rotation should be evaluated and eventually included in the constitutive equations.

2.1.3.2 Three-layer model:

The Three-Layer model adds one more stationary bed layer below the moving bed layer. Hence, adding one continuity and momentum equations with the corresponding stresses. The obtained equations need closure relations for both, the shear stresses and friction forces. A detailed example of an implemented transient three-layer model may be found in Guo *et al.* [23].

2.1.3.3 Necessary Parameters for the two- and three layer models:

In this case, it is also important to use experimental data to validate the models. However, the coefficients needed are different from the mechanistic models by Clark and Bickham [12]. In these models it is very important to measure the shear stresses between the non-Newtonian fluid and the cuttings bed and the stresses between the cuttings bed and the bore hole. Likewise, settling velocities for particles in non-Newtonian fluids and concentration distributions are variables, which need experimental data to validate the models. Some of the points where work is needed in order to improve the closure relations were pointed by Kelessidis *et al.* [19]:

- Solids distribution in the heterogeneous solid-liquid layer.
- Inter-facial-friction factor between the heterogeneous liquid layer and the moving bed of solids.

- Grain collision stresses in a granular flow known as Bagnold stresses.
- Terminal velocity of solids in Newtonian or non-Newtonian fluids, while taking into account the effect of hindered settling and the effect of walls.
- Fluid friction factors for fluid and walls of annulus.

2.1.4 Drift-flux model

First developments of the drift-flux model were proposed by Zuber and Findlay [24] and Wallis [25] for liquid-gas flows. The idea to model cuttings transport with the drift-flux model comes from other works (see Munkejord [26]), where this approach is used for gas-liquid flows, specially in the modelling of gas production. This treatment is justified by the fact that the liquid and gas phases have relatively large velocity differences. In previous modelling efforts the settling velocity was considered to be small enough to consider the suspension as an homogeneous flow. However as the particle size increases, larger velocity differences are also found in cuttings transport systems. This is the case in the drilling of deep hard rock formations where the cuttings may reach sizes up to 20 mm large. Furthermore, the drilling of HPHT formations involves an increase of the drilling fluid temperature and the consequent reduction in viscosity, which also results in larger settling velocities. On top of that, the use of low viscosity fluids recommended for drilling highly deviated sections has a detrimental side effect on the transport through the vertical sections.

The drift-flux model describes two-phase flows by coupling the motion of the dispersed phase to the average velocity of the mixture. In order to do so, constitutive equations describing the dispersed phase distribution across the section of a conduct and the average drift-flux of the dispersed phase with respect to the mixture are required. A derivation of this model starting from the more general two-fluid model was given by Brennan [27]. Its one-dimensional version solves two mass and one momentum equation for 3 unknowns: velocity of the mixture V_M, velocity of the dispersed phase V_d and pressure p.

The mass balance of solid-liquid mixture is expressed as

$$\frac{\partial A\rho_M}{\partial t} + \frac{\partial A\rho_M V_M}{\partial s} = 0, \tag{2.27}$$

for solid phase,

$$\frac{\partial A\rho_d}{\partial t} + \frac{\partial A\rho_d V_d}{\partial s} = 0 \tag{2.28}$$

and the momentum equation for the solid-liquid mixture,

$$\frac{\partial A\rho_M V_M}{\partial t} + \frac{\partial A\rho_m V_m^2}{\partial s} = -A\frac{\partial p}{\partial s} + A\rho_m\ g\ cos\ \alpha - A\Delta p_v, \tag{2.29}$$

where A is the cross-sectional area of the conduct, ρ_M the density of the mixture, V_M the average velocity of the mixture, ρ_d the density of the dispersed phase, V_d the average velocity of the dispersed phase and Δp_v the pressure loss due to viscous friction. In these set of equations, one closure is required to couple V_M with V_d and the other to supply Δp_v. The coupling is accomplished through the distribution coefficient C_0 and the drift-flux velocity of the particles V_{pj} as follows

$$V_d = C_0 \; V_M + V_{pj}. \tag{2.30}$$

C_0 and V_pj are empirical parameters dependent on the physical properties of the liquid and particles, volume fraction and geometric conditions, as eccentricity in the case of annular flows. These may be obtained as follows so far the local velocities and volume fractions of the flow are known

$$C_0 = \frac{\overline{\varepsilon_p J_M}}{E_p V_M} \tag{2.31}$$

$$V_{pj} = \frac{\overline{\varepsilon_p v_{pj}}}{E_p} \tag{2.32}$$

$$\overline{\varepsilon_p J_M} = \frac{1}{A}\int_0^A \varepsilon_p j_M dA = \frac{1}{A}\int_0^A \varepsilon_p(\varepsilon_p v_p + (1-\varepsilon_p)v_l)dA \tag{2.33}$$

$$\overline{\varepsilon_p v_{pj}} = \frac{1}{A}\int_0^A \varepsilon_p v_{pj} dA = \frac{1}{A}\int_0^A \varepsilon_p(v_p - (\varepsilon_p v_p + (1-\varepsilon_p)v_l))dA \tag{2.34}$$

$$E_p = \frac{1}{A}\int_0^A \varepsilon_p dA \tag{2.35}$$

$$V_M = V_{Sp} + V_{Sl} = \frac{1}{A}\int_0^A \varepsilon_p v_p dA + \frac{1}{A}\int_0^A \varepsilon_l v_l dA \tag{2.36}$$

In some cases it is possible to measure the local velocities and volume fractions through experimental set-ups. However, in the systems found in the drilling technique this is very difficult if not impossible and alternative methods are required. Detailed simulations at the wellbore diameter scale are becoming a real possibility at the time of developing the required empirical correlations. *This constitutes one of the main objectives of this thesis.*

With reference to the friction factors, the hydraulic calculation method of Pilehvari and Serth [28] constitutes the latest development and is able to consider non-Newtonian fluids and eccentric configurations. Effects of rotation should be integrated in the future. This is the subject of active research.

2.2 Forces acting on particles

This section is included to complement the models presented in the previous section. While the previous transport models are intended for the description of the transport along the complete wellbore, these are influenced by physical phenomena taking place at much lower scales. At the particle scale, several constitutive equations, mostly empirical, have been developed to predict forces acting on particles. Here, fundamental concepts and the latest developments are presented.

2.2.1 Body Force

Body forces result from the application of force fields on the complete volume of a body. Examples of these fields are electric or gravitational fields. In the modeling of cuttings transport, only gravitational fields are of importance and the force can be described as

$$F_g = m_p g, \tag{2.37}$$

where m_p is the mass of a particle and g the gravitational acceleration.

2.2.2 Buoyancy force

The Archimedes or Buoyancy force is due to the pressure distribution acting on an immersed body and is described as

$$F_A = V_p \rho_f g, \tag{2.38}$$

where V_p is the volume of the particle and ρ_f the density of the fluid. The force direction is contrary to the direction of increasing hydraulic pressure. The force is relevant in liquid-solid flows, where $\rho_f/\rho_p \approx 1$. In gas-solid flows, where $\rho_f/\rho_p << 1$ this force may be neglected.

2.2.3 Drag Force

In 1851, Stokes was able to solve the Navier-Stokes equations, for the flow past a sphere under the creeping flow assumption. With it, he was able to determine the stresses acting on the sphere as a function of fluid properties and by surface integration the forces acting on the same. The creeping flow assumption limits the validity of this result to very small particle Reynolds number (the viscous regime) defined as:

$$Re_p = \frac{\rho_f u_s d_p}{\mu}, \tag{2.39}$$

where ρ is the density of the fluid, u_s is the slip velocity between particle and continuous phase, d_p particle diameter and μ is the dynamic viscosity of the fluid. With it, the drag coefficient for flow past spherical particles may be computed analytically. The result is Stokes' law:

$$C_d = \frac{24}{Re_p}, Re_p \ll 1 \tag{2.40}$$

While the Stokes' solution may be applied to flows where viscous forces are predominant, further solutions based on first principles have only been able to solve the completely opposite case. Namely flows where inertial forces prevail and where the potential theory may be applied. Between these asymptotic cases, prediction of the drag forces acting on particles is only possible through the use of empirical correlations. Either developed on the basis of physical experiments or, as an emerging and increasingly validated methodology, on the basis of numerical experiments.

While drag forces acting on single spherical particles are now predicted with exactitude, there are still several complications, which make the prediction of drag in solid-liquid suspensions reluctant. Remaining in the field of Newtonian rheology of the carrying fluid, some important ones relate to the shapes of the particles, the effects of multiple particles and the effects of conduct walls, when they are present. For an extensive list and comments on them the book of Guazzelli and Morris [29] is recommended.

Previously, constitutive equations have been developed on the basis of physical experiments. These offer however a limited insight in the physical phenomena taking place and parametric studies become very complicated. For this reason, direct numerical simulation (DNS) where a limited amount of modelling is used is becoming an interesting alternative. Hill *et al.* [30] and [31] and Beetstra *et al.* [32] have used the lattice Boltzmann method (LBM) to develop drag correlations for bidispersed static suspensions. Furthermore, Yin and Sundaresan [33] have investigated the drag of solid particles in gas and pointed out the importance to consider the transfer of momentum from particle to particle through the interstitial fluid. Such transfer needs to consider the effects of lubrication forces, which apppear at very small scales below those resolved in the simulations. Koch introduced modeling of such forces in the LBM to be able to produce such correlations.

2.2.4 Lift force

"Particles moving in a shear layer experience a transverse lift force due to the non-uniform relative velocity over the particle and the resulting non-uniform pressure distribution." This is the description given by Sommerfeld *et al.* [34] of the Saffman lift force. Since the pioneering work by Segré & Silberberg [35], who described the migration of particles up to a certain equilibrium position, also known as the tubular pinch effect, several analytical, computational and experimental analysis have been carried out to uncover the underlying physics of this phenomena. It is well known that "the lateral forces acting on a spherical particle in a pipe flow are induced by the shear as well as by the interaction of the wall with the flow disturbances induced by the slip velocity and the shear" [36]. However, difficulties still exist in the accurate quantification of these forces in suspension in more complex flows, i.e. if multiple particles or poly-dispersity have to be considered. Yu *et al.* [37] made a comprehensive review of the work done on particle migration in a Poiseuille flow in the last 50 years. One of the milestones was the confirmation of the bilateral migration of neutrally buoyant particles towards an equilibrium position between the pipe axis and walls and the unilateral migration of non-neutrally buoyant particles towards the axis or the walls of the pipes. Aoki *et al.* [38] proposed the utilization of signed Reynolds particle numbers to denote if the particles were leading or lagging the flow. Moreover they measured displacements of the equilibrium position for particle Reynolds numbers from one to minus one. For values above those they were able to observe unilateral migration of the particles. Later analytical analysis further confirmed these appreciations and supplied interesting quantitative data for certain idealized cases at low Reynolds numbers. Further analytical analysis was limited because of cumbersome mathematical complications. With the increasing capabilities of computational power, numerical studies emerged in the nineties (Dandy & Dwyer (1990), McLaughlin & Dandy (1999) or Kurose & Komori (1999)). These studies mainly focused on the quantification of the lift force for fixed spherical particles in linear shear flows. However, to increase the range of microscopic and macroscopic information observed, it was necessary to develop dynamic simulation methods where the particle motions could also be included. Several methods also able to include the inertial effects of the flow were mainly developed in the late nineties and are being further improved till date. These methods can be mainly classified as non- and boundary-fitted methods. "The typical boundary-fitted methods are the Arbitrary Lagrangian-Eulerian (ALE) finite element method and the space-time finite element method. The non-boundary fitted method include the Lattice Boltzmann method (LBM), the fictitious domain method (FD), the immersed boundary method (IB), and the immersed interface method" [39]. The non-boundary fitted methods are simpler and more efficient than the boundary-fitted methods. Yu *et al.* [39] regard the FD method as more advantageous due to the ease of including constitutive equations for complex or non-Newtonian fluids.

2.2.5 Unsteady forces

The forces due to acceleration of the relative velocity can be divided into two parts: the virtual mass effect and the Basset force. The virtual mass effect relates to the force required to accelerate the surrounding fluid. The Basset term describes the force due to the lagging boundary layer development with changing relative velocity. Crowe *et al.* [40] also distinguish these forces in that the virtual mass force accounts for the form drag due to acceleration, while the Basset term accounts for the viscous effects.

2.2.5.1 Virtual or apparent mass force

The virtual mass force appears when a body is accelerated through a fluid. In order to accelerate the body, there is a corresponding acceleration of the fluid around the body, which is at the expense of work done by the body. This additional work relates to the virtual mass effect [40]. For inviscid fluids, Crowe *et al.* [40] give a nice derivation of the virtual mass force for a spherical particle

$$F_{vm} = \frac{\rho_f V_p}{2}(\frac{Du_f}{Dt} - \frac{du_p}{dt}), \tag{2.41}$$

where u_f is the fluid flow velocity, u_p is the spherical particle velocity, ρ_f is the mass density of the fluid, V_p is the volume of the particle and $\frac{D}{Dt}$ is the material derivative. For viscous fluids and larger particle Reynolds numbers, no analytical solution exists. Therefore, empirical correlations similar to those developed for drag are used. However, theses are less successful than in the drag case.

The correlations for the virtual mass force are based on the experiments of Odar and Hamilton [41]. They investigated the motion of a sphere in simple harmonic motion and gave the following description of the virtual mass force:

$$F_{vm} = 0.5\ C_{vm}\ \rho_f \frac{m_p}{\rho_p} \frac{d}{dt}(u_f - u_p). \tag{2.42}$$

Odar and Hamilton supplied the following correlation for the virtual mass coefficient

$$C_{vm} = 2.1 - \frac{0.132}{A_c^2 + 0.12}, \tag{2.43}$$

where A_c is the so called acceleration number defined as

$$A_c = \frac{|u_f - u_p|^2}{d_p \left| \frac{d|u_f - u_p|}{dt} \right|}. \tag{2.44}$$

2.2.5.2 Basset force

As described by Sommerfeld et al. [34]: "The Basset force is caused by the lagging of the boundary layer development on the particle while changing relative velocity, i.e. acceleration or deceleration". Reeks and McKee [42] proposed the following decription of the Basset force including the case where there is an initial velocity

$$F_B = 9\sqrt{\frac{\rho_f \mu_f}{\pi}} \frac{m_p}{\rho_p d_p} C_B \left\{ \int_0^t \frac{\frac{\mathrm{d}}{\mathrm{dt}}(u_f - u_p)}{(t - t')^{1/2}} dt' + \frac{(u_f - u_p)_0}{\sqrt{t}} \right\}, \tag{2.45}$$

where $(u_f - u_p)_0$ is the initial velocity difference, t is the current time, t' the time interval from the initiation of the acceleration to the present time and C_B the Basset empirical coefficient. Also here, the experiments of Odar and Hamilton [41] are the basis of the empirical coefficient C_B required to describe this force. Odar and Hamilton [41] proposed a coefficient dependant on the acceleration number A_C. However, a reinterpretation of the Odar and Hamilton data by Michaelides and Roig [43] suggests that the empirical coefficient C_B is a function of the particle Reynolds number and Strouhal number as follows

$$C_B = 1.0 - 0.527 \left[1 - exp(-0.14 Re_p St^{0.82})^{2.5}\right] \tag{2.46}$$

where the Strouhal number St is defined as

$$St = \frac{1}{2\pi f \tau_V} \tag{2.47}$$

This force is often neglected, because its calculation increases the computational costs by a factor of about ten as demonstrated by Sommerfeld [44]. However, when the rates of acceleration are high, this force becomes relevant and should not be ignored.

2.2.6 Collision forces

In dry granular flows, the influence of the interstitial fluid is negligible. Therefore, collision physics are basically dependent on the elastic properties of the materials. The amount of energy dissipated due to inelasticity of the contacts is normally characterized through a restitution coefficient, defined by the ratio of the rebound to impact velocity. On the other hand, collisions in viscous fluids are governed by several physical phenomena. Kempe and Fröhlich [45] decompose these collisions in three phases on the basis of experiments performed by Joseph et al. [46]: (a) The approach phase during which fluid forces govern the interaction. During this phase fluid pressure between the two colliding objects increases. Furthermore, the fluid squeezed between the objects produces viscous forces. (b) The collision phase, which takes place when the objects come in to contact. This phase is analogous to the contacts found in dry collisions. Therefore, the dominant mechanism is the deformation of the solid object. (c) The rebound phase, again dominated by the hydrodynamic interaction.

Davis et al. [47] showed that collisions in viscous fluids are dependent on the particle Stokes number defined as

$$St = \frac{1}{9} Re_p \frac{\rho_p}{\rho_f} \tag{2.48}$$

and an elasticity parameter, $\epsilon = 4\Theta\mu u_0 r_p^{3/2}/x_0^{5/2}$, where Θ is defined by Joseph et al. [46] as $\Theta = (1-\nu_1^2)/\pi E_1 + (1-\nu_2^2)/\pi E_2$ and depends on the Young's modulus and Poisson's ratio of the two bodies; x_0 is the position within the gap between the undeformed surfaces at which the velocity is u_0 and r_p is the particle radius. On the basis of these two parameters, Joseph et al. [46] investigated coefficients of restitution for particles in viscous fluids analogous to those used in dry collisions. The coefficients supplied by them accounted for the viscous dissipation and the kinetic energy needed to displace the fluid between the surfaces in addition to the inelasticity of the contact.

2.3 Measurement of multi-phase flows by optical methods

Research on momentum transfer has been usually executed in settling tanks, where the fluid is initially at rest. The time a particle takes to settle down is used to indirectly measure drag forces acting on that particle. The same experiment may be performed with multiple variations such as higher concentrations, bidisperse systems, particle shapes, non-Newtonian fluids. However, these experiments do not consider the effect of the mean shear if a flow field is imposed. In the case of polydisperse suspensions there is a major drawback in the use of settling tanks. This is the limited time span before particles of different species become separated in different regions. The use of recirculating experiments to maintain different species in continuous interaction allow obtaining averages of large amounts of data. In the past, several experiments have been performed to investigate the transport of solid-liquid mixtures in pipes and annular conducts. However, these are mostly concentrated on bulk parameters as the pressure gradient or delivered concentrations. This has been so, because of the inherent problems in the acquisition of local variables in solid-liquid mixtures.

The particle image velocimetry (PIV) is an optical non-intrusive method able to supply measurements of local flow variables. The functioning principle is based on the pulsed illumination through an appropriate light source of a plane situated in the flow under investigation. Microparticles with good tracking properties, quantified through the Stokes number, are seeded in the work fluids and scatter the light coming from the light source. The scattered light is acquired by a digital camera and in this way two images within a time interval Δt are obtained. The time interval needs to be high enough to allow displacement of the particles and small enough to keep the displacement of the particles within rectangularly distributed interrogation areas across the image. Through cross-correlation algorithms is then possible to evaluate the local velocities at every interrogation area through the capturing of the displacement of ensembles of particles.

The classic two dimensional velocity measurement in single phase flows allows with a relatively easy methodology an accurate quantification of the flow. The experimental set-up is applicable to multiple problems as long as the region under investigation is accessible for the light source and the camera. This requires transparency of the investigated systems. In pipe flows, one of the challenges is the refractive index adjustment to avoid light diffraction at the curved walls. However, the real challenges appear when multi-phase flows are investigated. Brücker [48] and Poelma [49] have given reviews of problems and solutions of PIV methods applied to dispersed phase measurements. The unequal scattering of light, the inadequacy of the conventional correlation algorithms and the eventually variable light intensities are some of the arising problems. In the study of multi-phase flows, the PIV method is typically combined with the particle tracking velocimetry. The main difference between both methods is the number of particles necessary to do the evaluation. While the PIV method works with ensembles of particles, the PTV method measures velocities of single particles.

In spite of the inconveniences caused by the inclusion of a dispersed phase, the PIV and

PTV methods have been successfully combined to obtain a crucial parameter in multiphase flows as the slip velocities between phases. This is accomplished through refractive index matching or phase separation techniques. In previous works, researchers have been able to measure spray jets [50], air bubbles in water flow [51], cavitation bubbles [52], pneumatic transport through vertical conducts [53] or solid particles in mixing tanks [54].

The first challenge appearing with increasing volume fractions is the dimming of the light intensity with increasing penetration depth of the light sheet. Particles located within the light sheet scatter light and consequently the intensity of the light diminishes in the direction of the light propagation. At low concentrations this effect is not significant. However, at high volume fractions the dimming of light may cause insufficient penetration depths. Zachos *et al.* [55] proposed a solution based on the substitution of the dispersed phase through glass particles with similar densities an adjusted refractive indexes.

The second challenge caused by higher volume fractions is the limited tracking ability of single particles. Merzkirch *et al.* [56] proposed a method to increase the tracking ability at high volume fractions by following ensembles of particles.

A further difficulty appears when trying to determine the relative velocity between phases. The continuous phase is seeded with enough particles to follow the movement of the fluid. However, the dispersed phase also scatters a certain amount of light. Conventional cross-correlation algorithms are not able to distinguish which phase is scattering the light. Therefore, information from the dispersed phase gets mixed with that of the continuous phase. This phenomena is termed cross-talking between phases. Hasan *et al.* [57], Gui and Merzkirch [58], Nishino *et al.* [59] and Lindken and Merzkirch [60] have offered solutions to these problem.

Hassan *et al.* [57] proposed a method in which the continuous phase was seeded with fluorescent tracking particles. To separate the information optical filters or image processing is necessary. The idea is to acquire only the information of the tracing particles. A second synchronised camera is then used to acquire the velocities of the dispersed phase.

The masking method of Gui and Merzkirch [58] is appropriate for dispersed systems, where a significant size difference exists. The method consists in the generation of masks covering the dispersed phase. The application of the cross-correlation algorithms considers subsequently only the positions not covered by the masks. The dispersed phase can be separately measured through application of PTV algorithms. The principal inconvenience of this method is the necessity to generate masks for every single image. When thousands of images are required, for example to obtain averaged variables of interest, the computational effort may become cumbersome.

Nishino *et al.* [59] combined the shadowgraphy method with PIV and PTV techniques. Their method consists in the recording of the shadows of the dispersed phase in two consecutive images. The PTV method is then used to measure the velocities. The continuous phase is measured through conventional PIV methods.

Lindken and Merzkirch [60] combined fluorescent dye with the shadowgraphy method to measure the position and shape of rising bubbles. They used a LED array back-illumination.

2.4 Multi-phase flow numerical models

According to Eskin and Derksen [61], the appropriate methods to model and simulate suspension flows are selected depending on the flow regime and the levels of detail and accuracy required. The flow regime is estimated based on Stokes numbers, Reynolds numbers, solids volume fraction, density ratios and possible particle shapes. The same allow an assessment of the forces relevant in the problem. Considering the levels of detail, the decision will affect if the forces acting on the particles are obtained from the solution of the flow fields around the particles or from force models also dependent on system parameters as the particle Reynolds number, shear rate or solids volume fraction. On the basis of this assessment it is then possible to select models able to consider the relevant physical phenomena.

2.4.1 Direct Numerical Simulation (DNS)

Methods resolving very small flow scales around the particles are known as fully-resolved Direct Numerical Simulation (DNS). Such methods rely on the Navier-Stokes equations to calculate the stresses acting on the particles and therefore little empirical modeling is required. They are commonly used for calibrating closure relations of turbulence models and particle forces. The high resolution of these methods is paid at the cost of having extremely high computational costs. Therefore, these methods are mostly used to perform fundamental research focused on small scale problems. The real-time capacity of these models is far from achievable at this time and in the near future. With the continuously increase in computational resources, solution of larger problems will be possible. In the suspension field, such methods are being used to generate correlations of drag or lift forces in polydisperse systems [31, 62, 63] and investigate the effects of particles on turbulent regimes [64]. Sommerfeld *et al.* [34] gave an extensive list of the most important DNS techniques developed in the last decade:

- Front Tracking
- Level Set
- Schock Capturing
- Marker Particle
- Simple Line Interface Calculation (SLIC) Volume of Fluid (VOF)
- Piecewise Linear Interface Construction (PLIC) VOF
- Immersed Boundary

The principal idea of all these methods is the solution of the continuous phase equations at scales lower than that of the dispersed phase. In addition, continuously changing boundary conditions originated by the displacement of the dispersed phase need to be handled conveniently. A main difference between the methods is the approach used to discretize the continuous phase. In most of the cases this is done through fixed cartesian grids. However, also dynamic grids have been used. In the case of fixed grids, a crucial task is the proper definition of the interfaces within the computational domain. On the other hand, dynamic grids spend a large amount of computational capacity in the generation of new suitable grids.

2.4.2 Discrete Particle Model (DPM)

Discrete element methods (DEM) have been applied to the simulation of particle problems since they were first proposed by Cundall and Strack [7]. These are able to consider the motion of particles based on the action of body and contact forces. A natural extension of these models is the DPM method, where also hydrodynamic effects are considered. The DPM method is also termed in the literature as the CFD-DEM method. This observation by Zhou *et al.* [65] points out the main advantage of the model in comparison to two-fluid methods explained later: "The main advantage of CFD-DEM is that it can generate detailed particle-scale information, such as the trajectories of and forces acting on individual particles, which is key to elucidating the mechanisms governing complicated flow behavior". As a consequence, these methods do not require knowledge of the rheological properties of the dispersed phase, which are dependent on volume fraction, particle size distribution, shape and roughness. Therefore, offer an increased level of predictive ability.

The crucial point of this method is the transfer of information between the continuous phase and the dispersed phase. Also here, fixed grids are used to solve the continuous phase equations. On the other hand, particle motion is solved in a Lagrangian framework with freedom of movement across the computational domain. The discretization of the continuous phase governing equations is based on the description developed for the two-fluid method. Briefly, the model formulation couples the dispersed phase with the continuous phase through the volume fraction field variable and the momentum transfer terms. The volume fraction is calculated on the basis of the positions of the particle within the computational domain. With respect to momentum transfer, this is calculated through closure relations and constitutes a basic difference in comparison to the DNS methods presented above, where forces are directly obtained by integration of stresses on particle surfaces.

Attention needs to be paid to the model formulation, since three appear in the literature. Zhou *et al.* [65] performed an analysis of the three different formulations. They clarified that formulation II corresponds to a model known in the literature as type A and that formulation III corresponds to model type B. On the basis of their analysis they recommended to perform further research with model type A, since model type B is conditionally correct. Such conditions require a steady fluid flow and the by them described residual force acting on the particle to be zero.

Analogous to DEM methods, DPM methods are mainly divided in the hard-sphere approach and the soft-sphere approach. Hoomans *et al.* [66] presented the first implementation of a DPM model based on the hard-sphere approach. As described by Deen *et* *al.* [67]: In the hard-sphere approach "trajectories of the particles are determined by momentum-conserving binary collisions. The interactions between particles are assumed to be pair-wise additive and instantaneous. In the simulation, the collisions are processed one by one according to the order in which the events occur. For not too dense systems, the hard-sphere models are considerably faster than the soft-sphere models". As pointed out by Deen *et al.* [67], the weakness of the hard-sphere models is its limitation to work in the range of low particle number densities and high coefficients of restitution. When working out of this range, the model suffers of a problem known as the inelastic collapse described by McNamara and Young [68]. With reference to the soft-sphere approach, the first implementation was presented in the literature by Tsuji *et al.* [69]. Again, as described by Deen *et al.* [67]: "Soft-sphere models use a fixed time step and consequently the particles are allowed to overlap slightly. The contact forces are subsequently calculated from the deformation history of the contact using a contact force scheme. The soft-sphere models allow for multiple particle overlap although the net contact force is obtained from the addition of all pair-wise interactions. The soft-sphere models are essentially time driven, where the time step should be carefully chosen in the calculation of the contact forces".

As explained in section 2.2.6, collisions in viscous fluids are characterized differently from those found in dry collisions. Therefore, solid material properties are not sufficient input parameters. Joseph et al. [46] provided coefficients of restitution measured on the basis of experiments studying the collision of different material particles in various fluids. Likewise, Xu and Yu [70], Yang *et al.* [71] or Apostolou and Hrymak [72] have tried to account for the viscous effects through reduction of the Young's modulus to a value lower than obtained with realistic material pairing. The flaw of these methods is the lack of predicting ability. Kempe and Fröhlich [45] have proposed a model called the adaptive collision time model (ACTM) considering the different phases of particle contact in viscous fluids. The model supplies and increased level of predicting ability, but has only been tested with immersed boundary approach. It would be interesting to test it with DPM methods and study its computational efficiency.

2.4.3 Eulerian-Eulerian

The Eulerian-Eulerian model is an approach where every phase in the system is considered through an Eulerian framework. That is, considering every phase as a continuous medium. This is done independently of the condition of the phase, continuous or disperse. As a consequence, the model is also called two-fluid method or multi-fluid method, if more than two phases are described. The model was initially introduced by Ishi [6] in 1975 but has been extensively used in the modeling of liquid-gas, gas-solid, liquid-solid and liquid-liquid flows. As in the DPM models, key-quantities are the volume fractions and the momentum transfer between phases. The Eulerian nature of the two-fluid model provides an averaged description of every involved variable. Several averaging approaches, including time-averaging, volume-averaging or ensemble averaging; have been proposed in the literature [6], [73] and [74] between others. A consequence of the averaging is loss of detail, which needs to be supplemented through closure relations, as the one used in turbulence modeling. These closure relations include the modeling of drag, lift, virtual mass and Basset forces.

The advantages of the model as described by Crowe [40] are: (1) The numerical scheme used for the continuous phase can be used for the dispersed phase. Therefore, the discretization of the equations follows analogous methodology and can be solved with the same methods for each phase. (2) The model can be used to simulate high volume fractions and at large scales, because the computational load does not depend on the number of dispersed particles.

Main disadvantages of the two-fluid method, also pointed out by Crowe [40], are: (1) The definition of the rheological properties of the dispersed phase. As already commented in the case of solid-liquid flows, these are dependent on volume fraction, particle size distribution and shape. Therefore, specially adapted descriptions of the rheology are required for every simulated system. (2) The boundary conditions for mass, momentum and energy are not straightforward. (3) The equations are not applicable as the flow becomes increasingly dilute.

3 Experimental setup and measurement equipment

"If you cannnot measure it, you cannot improve it"

- Lord Kelvin

This chapter is dedicated to the description of the experimental set-up and the experimental methods used for the determination of fluid and particle velocities and particle distributions for different operating conditions. It starts with the requirements to obtain a system with fundamental similarities to the cuttings transport problem and make the measurements of suspensions viable. After that, details on the solid-liquid system are given. The description and explanation of the experimental set-up follows. Finally the measurement system is explained.

3.1 Requirements

The experimental set-up was designed to carry out studies related to vertical transport of cuttings generated during drilling operations. This required determination of the characteristic hydrodynamic parameters found in this particular application and their replication in the experimental apparatus. That being said, the fundamental nature of the investigations allows to extract conclusions applicable to other fields of industrial technology. Optical non-intrusive methods were chosen to obtain fluid velocity fields and particle positions in laminar flow suspensions. This requires fluids and dispersed solids with appropriate optical properties. Searching and testing these materials was an important task during the design.

Dispersed system An important characteristic of cuttings transport is the fact that the dispersed phase is preferably transported under laminar flow conditions. Considering density ratios of order 2.5, commonly found in the drilling technique, and well diameters of up to 450 mm, this requires viscosities notably higher than the one of water at room temperature. Furthermore, it was desired to investigate particles with sizes falling within the range of fine gravel (2 to 6.3 mm according to the international scale soil classification ISO 14688-1), because such sizes are commonly generated in hard rock formation drilling.

Pipe diameter and length Determination of the pipe diameter is based on the necessary velocities to transport particles with the selected fluid, density ratios and particle diameters. The length of the pipe was limited by the height of the laboratory. Moreover, it was desired that the flow is fully developed.

Orientation Orientation of the pipe is crucial in the determination of the flow regimes appearing in the transport of solid-liquid suspensions. In the experiments it was desired that gravity effects should not influence the particle distributions. Therefore, a vertical orientation was used. Furthermore, analysis of drag in vertical pipes is far more practical than in horizontal test sections, since the direction of the main forces is concurrent.

Optical access The setting up of the particle image velocimetry (PIV) requires the prior optical adjustment of the two phases. It was necessary to find transparent fluid and particle materials with high refractive indexes. High refractive index fluids are often organic solutions of high viscosity. This limits the range of operation regimes to low Reynolds numbers, which in this case is a desired characteristic. Moreover, the settling velocities of particles in such fluids decrease in comparison to those of water. Therefore, transport of coarse particles may be performed at lower velocities. For the dispersed phase, usually glasses or polymers with refractive indexes close to 1.4 are selected.

Particles integrity and concentration control It was necessary to ensure the integrity of the particles to maintain stability of the particle properties. Therefore, design of a system to introduce particles after the pump outlet and to recollect them before the pump inlet was necessary. The aim of the system was to avoid particle collisions with high speed moving parts in the pump. At the same time this system should provide the methods to control concentration during the experiments and facilitate the injection and extraction of the particles in and out of the flow loop.

3.2 Solid-Liquid System

3.2.1 Solid phase

Spherical glass particles were selected to concentrate on the phenomena of interest and avoid possible interferences from more complex shapes. Likewise, spherical glass particles show more convenient optical properties and allow easier object recognition treatment. Two types of surfaces were tested: polished and matt finished. Although matt particles were much easier to recognize, the polished surface was selected due to its lower light absorption, which allowed to perform experiments with higher concentrations. As seen in table 3.1 two different glass types were used. For 2 millimeter particles soda lime with a density of 2580 kg m^{-3} and for 4, 5, 6 millimeter borosilicate with a density of 2230 kg m^{-3}. The different types of glasses respond to the impossibility to find 2 millimeter borosilicate (the prefered glass option) particles with polished surface. This translated in a concentration limitation for measurements considering 2 millimeter particles. The solid glass beads were Type P and Type S from the company Sigmund Lindner GmbH. Particle size distributions (PSD) obtained with the QICPIC-System developed by Sympatec GmbH are shown in section 3.4.2.2.

Soda Lime beads
$d_{p2} = 2050 \pm 100\ \mu\text{m}$ $\rho_p = 2580\ \text{kg m}^{-3}$ $n_D = 1.528$
Borosilicate beads
$d_{p4} = 4000 \pm 100\ \mu\text{m}$, $d_{p5} = 5050 \pm 100\ \mu\text{m}$ and $d_{p6} = 5900 \pm 200\ \mu\text{m}$ $\rho_p = 2230\ \text{kg m}^{-3}$ $n_D = 1.464$

Table 3.1: Particle properties

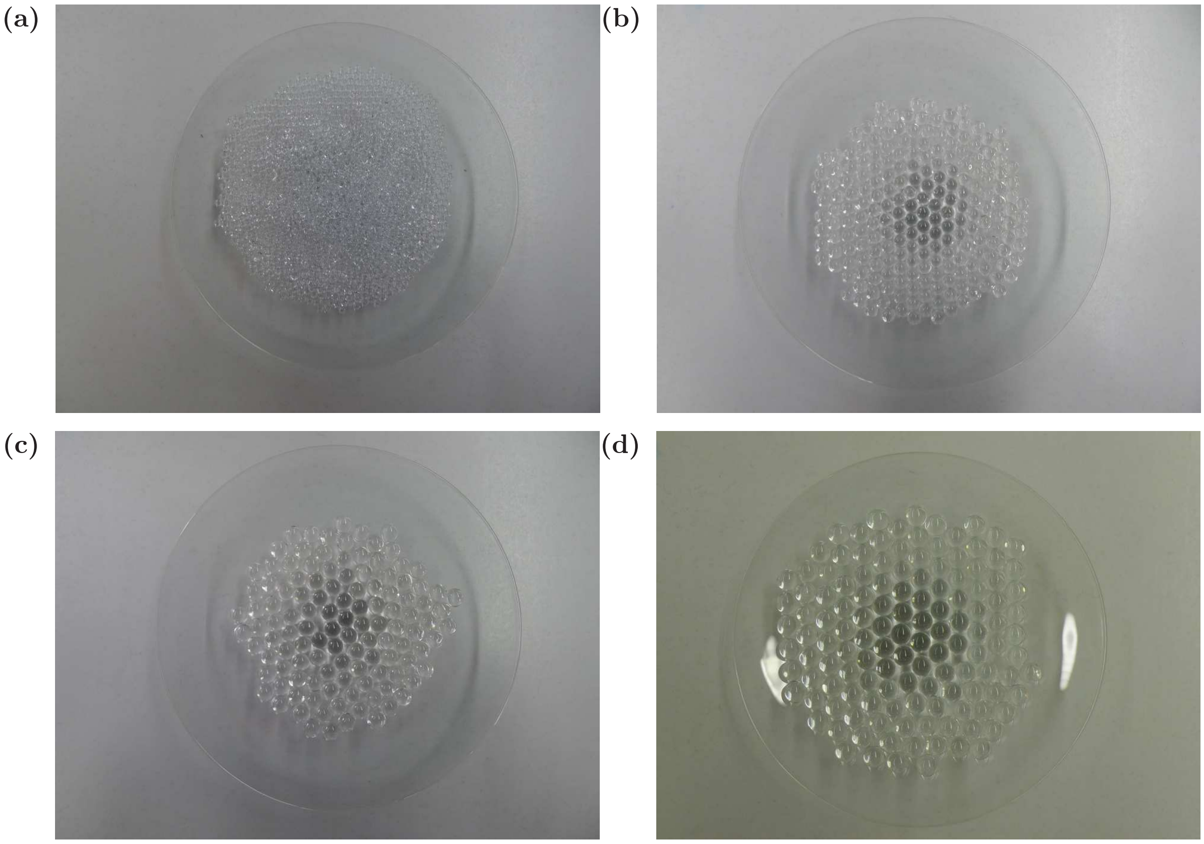

Figure 3.1: Glass particles used in the experiments: (a) 2 mm particles, (b) 4 mm particles, (c) 5 mm particles and (d) 6 mm particles.

3.2.2 Liquid phase

Due to its convenient refractive index (1.473 at 20 °C) light liquid paraffin (Shell Ondina 927) was selected as the working fluid. This fluid was selected to match the refractive index of the borosilicate particles (n = 1.464). According to a previous study conducted at our institute by Tchickango [75], the refractive index of Shell Ondina 927 at 30 °C (operating temperature) is 1.47. The slight difference produces clear delimitation of the particles, which was helpful for the particle location algorithm (CircularHough_Grd by Peng [76]). The temperature is measured electronically in order to monitor density and viscosity. Density at 15 °C is 865 kg m^{-3} and the volumetric expansion coefficient is $\beta_{exp} = 7.64 \times 10^{-4}$. The dynamic viscosity is correlated with temperature T within the range 20-40 °C using the following expression $\eta = -2.15\,T + 114.30$ mPa · s.

3.3 Experimental setup [1]

The Vertical Multiphase Flow Loop is shown schematically in Fig. 3.2. The construction follows concepts presented by Kriegel and Brauer [78]. Particles are added to the flow through a feeding device (eductor) and transported through the hoses and later through the test section to a separating container. In this container, particles are redirected to the feeding device while the fluid enters the pump. In figure 3.3, constructive details of the set-up are shown. Table 3.2 summarizes key parameters of the experimental setup.

test section length	2 m	working temperature	30 °C
test section diameter D	64 mm	viscosity	72 mPa · s
system Volume	30 dm^3		
total height			
flow velocity	0 - 0.6 m/s		
flow rate	0 - 30 l/min		
Re_D	150 - 300		
Re_p	10 - 20		

Table 3.2: Experimental setup characteristics

3.3.1 Test pipe

To allow optical access the test pipe needed to be constructed with a transparent material. Two options are normally considered: glass and plastic. Plexiglass® was selected because of its resistance properties. The flow loop was conceived to measure suspensions with different carrying media (Newtonian, pseudoplastic and yield-pseudoplastic). Therefore, an easy to handle material to perform cleaning operations was favored. The experimental test section consists of a Plexiglas® pipe with inner dimensions of Ø 64 x 2000 millimeters, which considering the work fluid selected allows pipe Reynolds numbers up to 300. The

---

[1] Part of this description was published in a paper for the International Journal of Multiphase Flow [77].

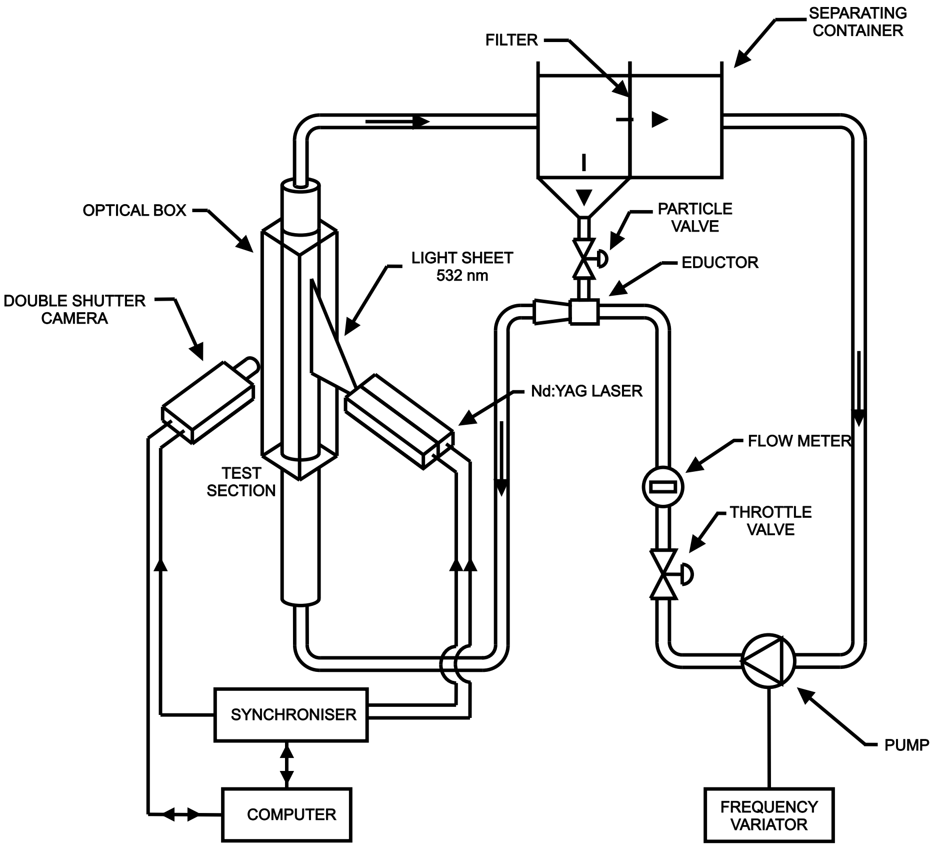

Figure 3.2: Diagram of the vertical multiphase flow loop.

entrance of the pipe has inner dimensions of Ø 28 mm, resulting in an expansion coefficient $\beta = 2.28$. Although Plexiglass® has a refractive index of 1.49, preliminary tests with single phase flows of Ondina 927 proved adequacy of the optical system. Strictly speaking, the walls of the pipe could be seen in the images, but reflections did not affect optical access to regions close to the walls.

To avoid optical distortions caused by the curved walls of the pipe a solution widely found in the literature [79] and [80] was used. This consists of a rectangular box of the same material of the pipe filled with light liquid paraffin. Other possible options are the drilling of a cylindrical cavity in a massive Plexiglas® rectangular piece. However, this presents the difficulty of the pipe joining points, which may affect the fluid flow just at the measuring positions.

3.3.2 Pump

The pump had to be able to move light liquid paraffin at velocities necessary to transport the particles selected. Due to the high viscosity of the fluid, this required the use of a multi stage pump (16 stages, nominal flow rate $0.0016\,\mathrm{l\,s^{-1}}$) from the company Grundfoss. An image of the pump and the inlet and outlet hoses is shown in figure 3.5.

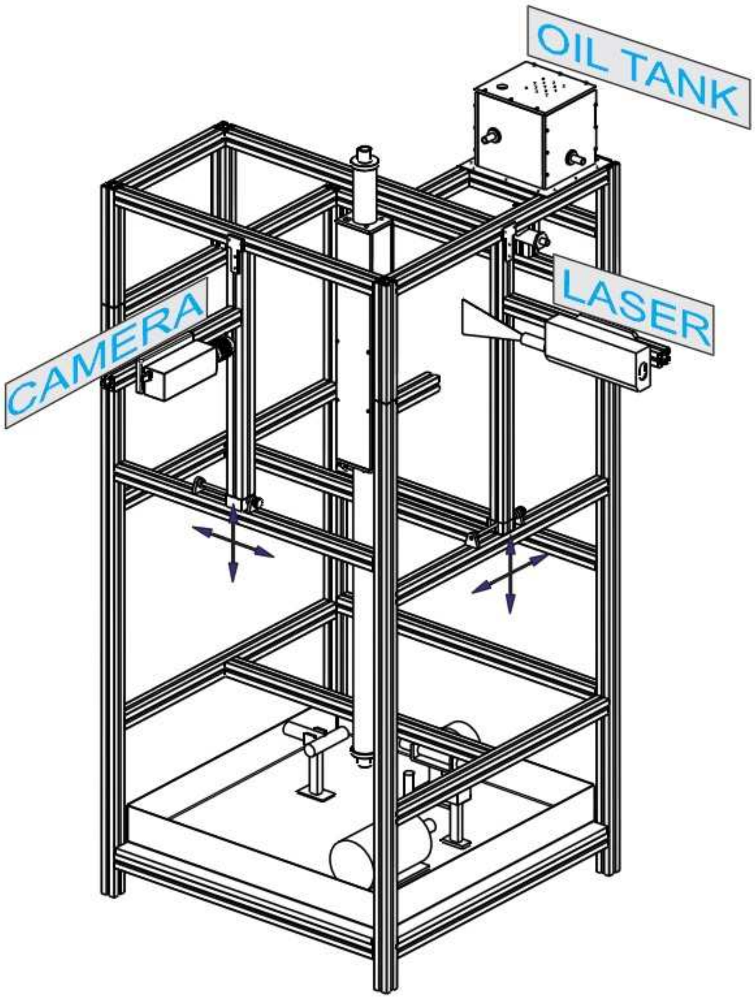

Figure 3.3: CAD figure of the vertical multiphase flow loop.

3.3.3 Eductor

The eductor shown in figures 3.6 and 3.7 was designed to avoid the circulation of the particles through the pump and avoid in this way attrition of the particles and damaging of the pump. The design was based on simulations with the software COMSOL to predict operation with high viscous fluids. The different parts of the eductor were manufactured at the institute.

The eductor is formed by three parts: the nozzle, the main body and the venturi. The nozzle accelerates the fluid coming from the pump to decrease the static pressure in the nozzle exit region. The reduction in pressure is used to suck the particles contained in the separating container located above. The main body supports the nozzle and the venturi and connects the eductor to the container where the particles are separated from the fluid. The venturi is installed to mix the particles with the fluid and obtain a homogeneous mixture. This was used in low concentration measurements. To allow measurements with higher concentrations it was necessary to dismantle it.

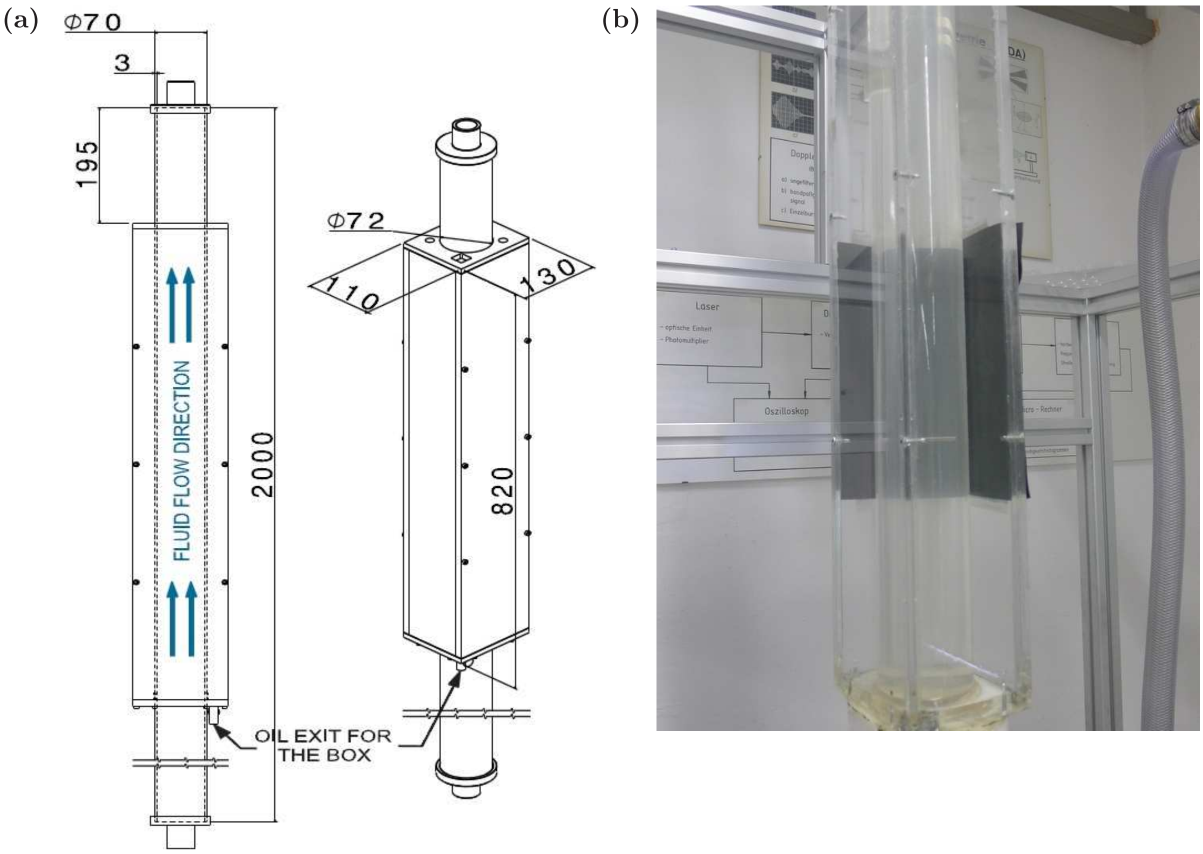

Figure 3.4: Optical box: (a) CAD drawing and (b) picture.

Figure 3.5: Driving pump

Figure 3.6: Picture of the eductor.

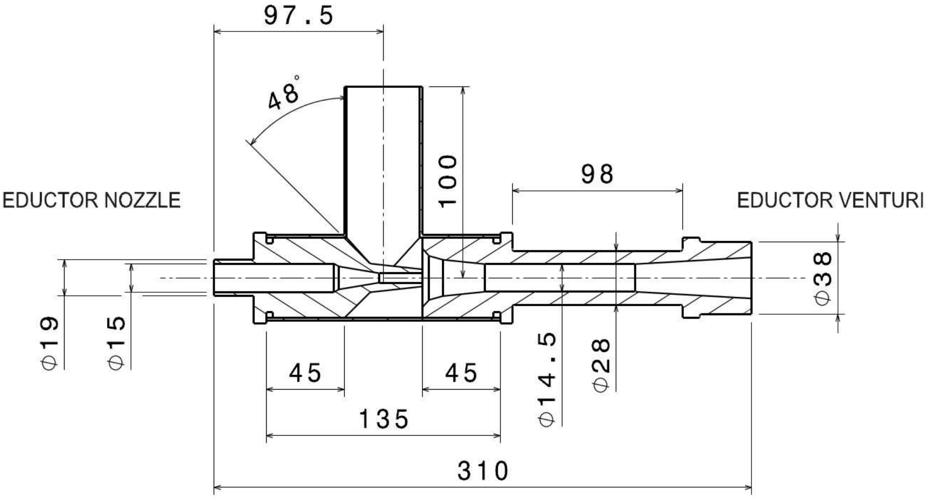

Figure 3.7: CAD drawing of the eductor.

3.3.4 Separating container

The separating container was designed considering two requirements: recirculation of the particles and their easy introduction and extraction. The first one was fulfilled by situating the separating container right above the eductor. Likewise, it was necessary to directly connect them through a valve. The second requirement was accomplished with a removable container cover.

The fluid level in the separating container is an important factor to operate the eductor. Since the studies were conducted in a vertical pipe, it was necessary to place the container on an elevated position. In this way, the pressure in the system was set for optimal operation of the eductor.

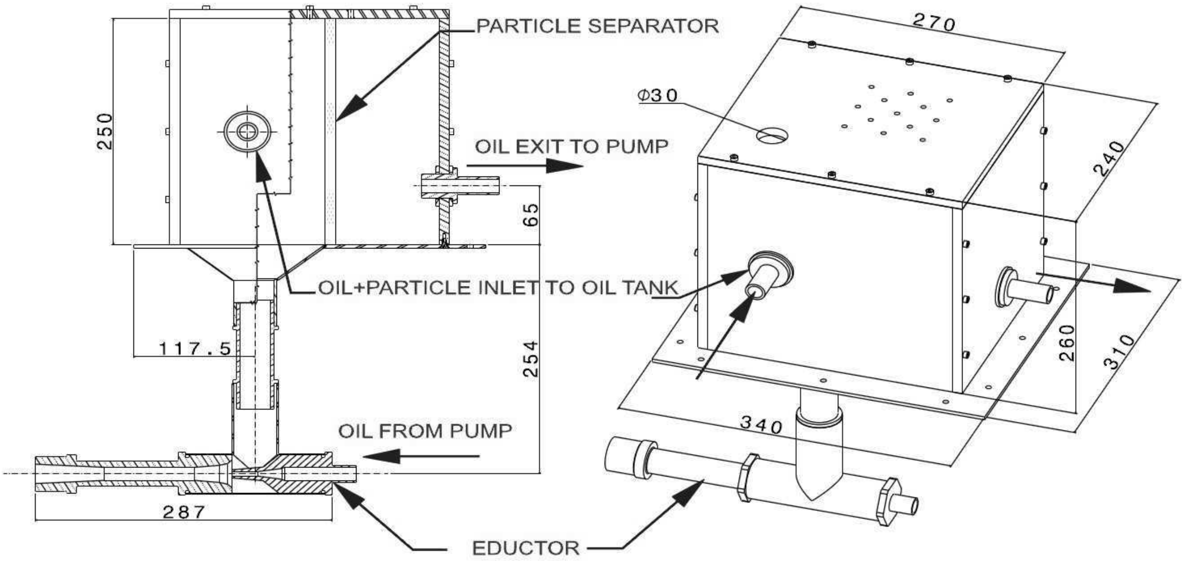

Figure 3.8: Eductor

3.4 Measurement system

The measuring system was conceived to measure velocities of dispersed solids and suspending liquid and characterize the physical properties of the system for every experiment. Since different methods were necessary for each phase, the measurement system is explained in two subsections: (1) measurement of suspending liquids and (2) measurement of dispersed particles.

3.4.1 Measurement of suspending liquids

3.4.1.1 Temperature

For all measurements, the temperature in the separating container was used to determine density and viscosity of the operating fluid. A calibrated thermocouple type K with 0.01 K resolution was used. The thermocouple was connected to an analogical/digital signal converter and the digital signal was directly fed to the measurement PC.

The flow of the liquid through the pump caused an increase of temperature of the fluid reaching equilibrium temperature around 30°C. During the measurements, the temperature was continuously recorded. No tempering system was necessary due to the stability of the temperatures reached after around 30 minutes of the pump operation.

3.4.1.2 Flow meter

The flow meter was used in a preliminary phase to calibrate the PIV system. Once the eductor was opened, the flow meter was no longer able to supply correct flow rates because the eductor entrained additional fluid not flowing through the flow meter. The flow meter installed in the ITM flow loop was manufactured by Badger Meter Europa GmbH, which works on the principle of positive displacement pumps.

3.4.1.3 Particle image velocimetry

The Particle Image Velocimetry (PIV) is a non intrusive method to obtain instantaneous measurements of velocity fields. The flow is illuminated by a thin light sheet, predominantly from laser sources. The measurement principle consists in the determination of the displacement of micro-particles or groups of them within a specified time interval. The Stokes number of the particles-flow system should be minimized in order to guarantee close following of the fluid. Furthermore, particles should possess the capacity to reflect the light of the light sheet. The displacement of the particles is calculated through cross-correlation algorithms applied on interrogation windows distributed on a regular mesh. This allows the measurement of velocities along the light sheet. A more extensive and complete description of the method can be found in the book by Raffel et al. [81].

Refractive index matching: Refractive index matching is commonly used in the PIV technique to avoid reflections of the immersed boundaries. Budwig [82] provided several solid-liquid combinations and the pros and cons of using them. In two-phase measurements, this matching allows to capture liquid velocities with relatively dense solid-liquid suspensions. Also in this case, there are several authors [83, 84, 85, 86] who have used this approach to obtain flow fields of liquids carrying solid dispersed particles.

In this work a very close matching of the refractive indexes was accomplished. However, the index matching was not perfect. Although this limited the working concentrations up to 4%, it had a beneficial side effect. Namely, the possibility to clearly identify particle sizes in polydisperse suspensions. A perfect matching of the refractive indexes would not allow clear identification, since the particles not falling exactly under the light sheet would present smaller diameters. Complicating discrimination of particle species in bidisperse suspension experiments. This is graphically shown in figure 3.9. Therefore, a slight difference in the refractive indexes helped to locate the particles with image processing algorithms.

The quality of the fluid phase images suffered heavily from the presence of the particles. In figure 3.10 raw images for increasing concentrations are shown. Although the edges of the particles are clearly seen, this is done at the cost of loosing light intensity.

PIV equipment The PIV technique was used to obtain two dimensional-two components (2D2C) suspending fluid velocity fields. Rather than choosing a two-cameras set-up, as the one described by Poelma [49], a single camera set-up with alternative fluid and particle measurements was chosen. This results in an optical setting easier to implement, but more complicated to operate because of the alternation in the settings of the camera-laser synchronizer and the laser power.

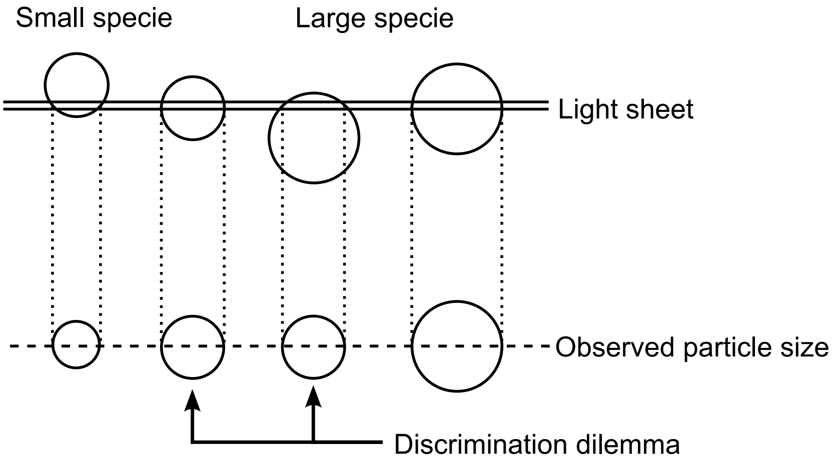

Figure 3.9: Particles falling at different positions with respect to the center of the laser light sheet.

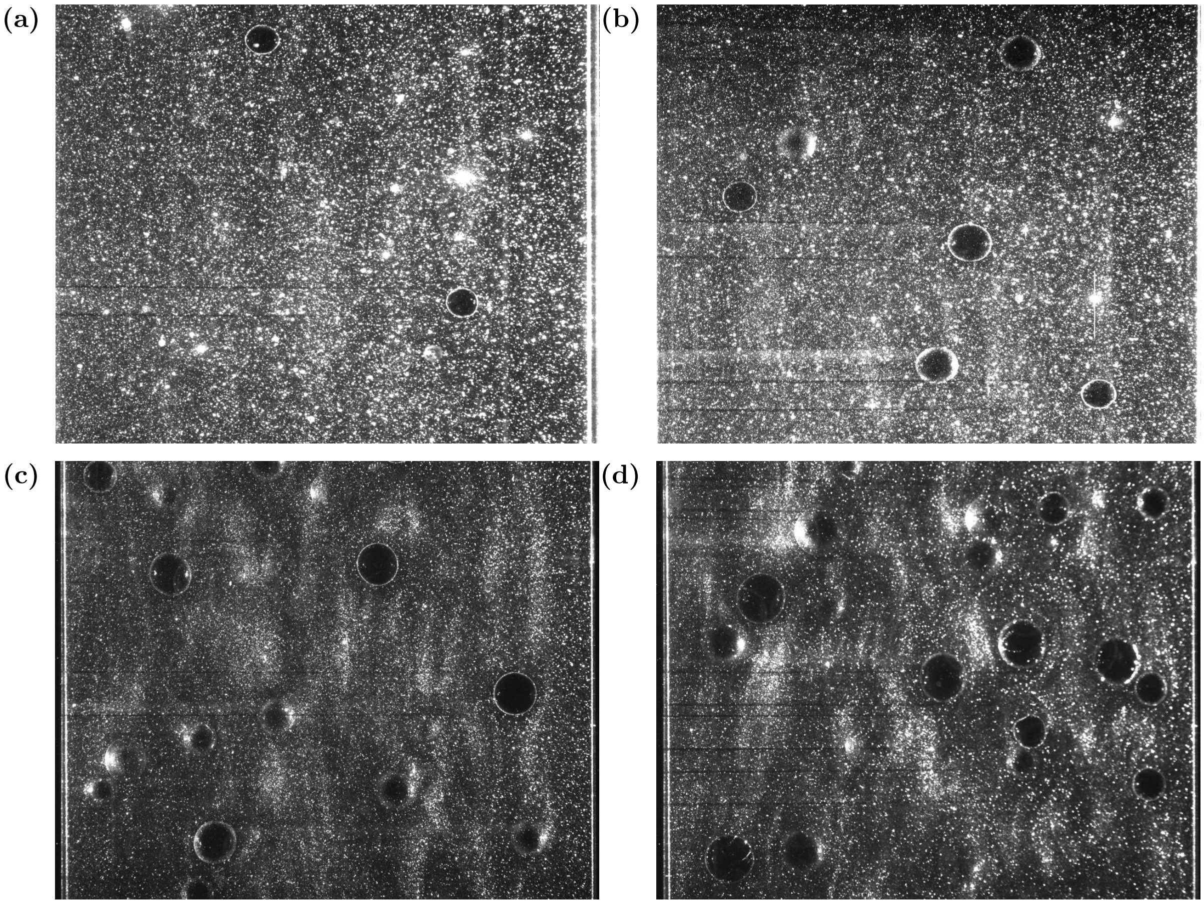

Figure 3.10: Raw images at different concentrations: (a) exp. 10, $\phi_4 = 0.50\%$, (b) exp. 20, $\phi_4 = 0.62\%$ and $\phi_5 = 0.50\%$, (c) exp. 37, $\phi_4 = 1.50\%$ and $\phi_5 = 1.50\%$ and (d) exp. 62, $\phi_4 = 2.00\%$ and $\phi_6 = 2.00\%$.

The working liquid was seeded with hollow glass spheres (Sphericel 110P8, from Potters Industries Inc.) with mean diameters of 9-18 μm and an average density of 1100 kg m-3. The parameter that quantifies traceability of the seeding particles is the Stokes number ($St = 1/18\ \rho_s\ d_s^2/\mu_f\ U/d_p$, where ρ_s is the density of the seeding particles, d_s is the diameter of the seeding particles, μ_f is the dynamic viscosity of the fluid, U is the average velocity of the fluid and d_p is the diameter of the dispersed particles). In our experiments the largest Stokes number was 1.6×10^{-6}, assuring good traceability of the seeding particles. Illumination was accomplished with a double-cavity pulsed Nd:YAG laser with wavelength of 532 nm and light pulse duration of 5 ns. Pulse separation was adjusted to 2.5 ms and the laser head energy is set to 80% of the maximum energy (30 mJ). A double-concave lens f = 20 mm to spread the laser beam, a focal distance adjustment to set the light sheet thickness in the illumination plane and a 16° cylindrical lens f = 25 mm transform the laser beam into a thin vertical light sheet of about 1 mm thickness. The light scattered by the particles was recorded on the charge coupled device (CCD) sensor of a camera (PCO sensicam qe with 1376 x 1040 pixels and 12-bit resolution), which was placed perpendicular to the region of interest. In order to capture the image pairs, the camera was used in the double exposure frame-triggering mode with an acquisition frequency of 4 Hz. A lens (Nikon Micro-NIKKOR 55 mm) was mounted at the camera with the F-number adjusted to 2.8.

The camera and the laser were mounted on aluminum profiles fixed to the flow loop structure. The separation between the region of interest and the camera sensor was approximately 80 cm. As previously commented, a flat-faced Plexiglas® optical box positioned over the pipe was installed to minimize distortions in the optical measurements. Light liquid paraffin was also used as the liquid medium between the Plexiglas® optical-box and the pipe wall. Recordings were taken at a location 1.6 m (25 diameters) downstream of the inlet of the test section. In the measurements, the axis of the pipe was coplanar to the light sheet.

3.4.2 Measurement of dispersed particles

3.4.2.1 Particle load

Bulk volume fractions ϕ_i were determined by weighting the amount of particles introduced in the system and assuming homogeneous distribution of the particles in the two-phase section of the flow-loop. An electronic mass balance was used for such purpose. This one had an accuracy of 1 milligram.

3.4.2.2 QICPIC

In order to give an accurate characterization of the dispersed particles, their size distributions were obtained with the QICPIC analysis by Sympatec GmbH. The analysis is based on image processing and allows obtaining highly resolved particle size distributions and sphericity of the particles. In the analysis particles are dispersed at a very high velocity in order to keep the particles far from each other. This avoids superposition of the particles, which would complicate the image processing. Due to the high velocities of the particles, a flash lamp with a pulse duration of less than 1 ns is used. With such a pulse duration the moving unsharpness is about 100 nm. Far from the smallest particle size of 2 mm. Histograms of the particle sizes obtained with the QICPIC system are displayed in figure 3.11.

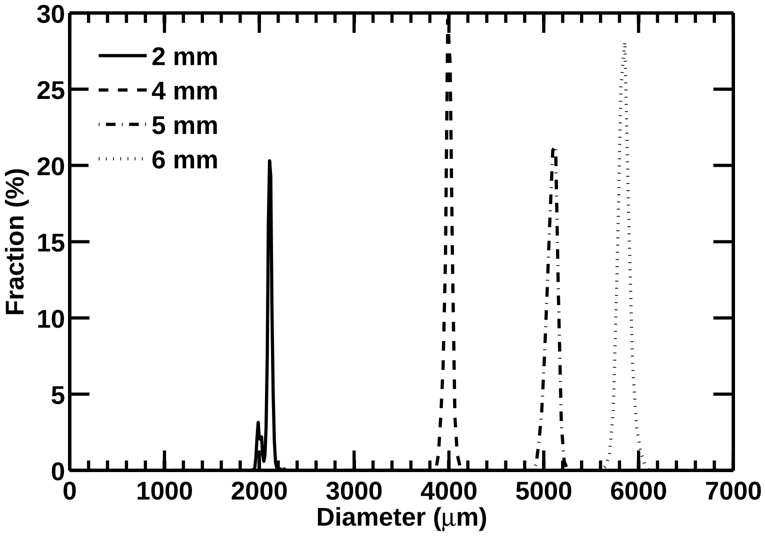

Figure 3.11: Particle size distributions for the used particles

3.4.2.3 Particle Tracking Velocimetry (PTV)

Measuring the particle velocities was made possible by the implementation of a particle tracking algorithm. The PTV method is based on a Lagrangian frame of reference. Essentially determining the displacement of a single particles by locating the same particle in two consecutive frames. The velocity is recovered by determining the displacement of the particle and dividing it through the time between the two frames. The implementation used in this work was based on the nearest neighbour algorithm adapted to search particles within a maximum radius. The location of the particle was performed through the Hough transformation algorithm (CircularHough_Grd by Peng [76]) able to locate circular shapes.

4 Multi-phase flow models

In this chapter, the two numerical formulations selected for the simulation of solid-liquid suspensions are presented. Firstly, the Two-Fluid method based on an Eulerian-Eulerian approach is introduced. The CFD-DEM implementation based on an Eulerian-Lagrangian approach is described afterwards.

4.1 Two-Fluid method

In the Two-Fluid Method, equations of mass and momentum are solved for both phases. Constitutive equations describing phenomena at sub-grid scales are used to close the conservation equations. Basics of the method are outlined here. Discussions on the same are extensive and may be found in the PhD Thesis of Rusche [87] or the paper by van Wachem and Almstedt [88]. Each phase is described using the volume-averaged, incompressible, transient Navier-Stokes equations. The volume-averaged continuity equation is given by (ph = liquid, solids):

$$\frac{\partial}{\partial t}(\phi_{ph}\rho_{ph}) + \nabla \cdot (\phi_{ph}\rho_{ph}u_{ph}) = 0, \tag{4.1}$$

where u_{ph} is the velocity vector, ρ_{ph} is the density and the volume fraction of each phase ϕ_{ph}, satisfies the constraint:

$$\phi_l + \phi_s = 1. \tag{4.2}$$

The momentum balance for for the liquid phase is given by the Navier-Stokes equation, modified to include an inter-phase momentum transfer term:

$$\frac{\partial}{\partial t}(\phi_l\rho_l u_l) + \nabla \cdot (\phi_l\rho_l u_l u_l) = -\phi_l\nabla p + \nabla \cdot \tau_l + \phi_l\rho_l g - F_{tot}, \tag{4.3}$$

where p is pressure, g is the gravitational acceleration vector, τ_l is the liquid phase stress tensor and F_{tot} is the interfacial momentum transfer per unit volume made up of the drag force F_d, the lift force F_l and the virtual mass force F_{vm}. Depending on the relevant interactions, other sources of force may be added.

The solids phase momentum balance is given by

$$\frac{\partial}{\partial t}(\phi_s \rho_s u_s) + \nabla \cdot (\phi_s \rho_s u_s u_s) = -\phi_s \nabla p + \nabla \cdot \tau_s + \phi_s \rho_s g + F_{tot}. \tag{4.4}$$

The solid phase stress tensor τ_s, can be expressed in terms of the solids pressure P_s, bulk solids viscosity ζ_s, and shear solids viscosity μ_s:

$$\tau_s = (-P_s + \zeta_s \nabla \cdot u_s)I + \mu_s \left\{ [\nabla u_s + (\nabla u_s)^T] - \frac{2}{3}(\nabla \cdot u_s)I \right\}. \tag{4.5}$$

4.1.1 Closure equations

The interphase momentum transfer between solids and liquid due to drag force is given by

$$F_d = \frac{3}{4}\; C_D\; \phi_s\; \rho_f \frac{1}{d_p} \left| u_l - u_s \right| (u_l - u_s) \tag{4.6}$$

The drag coefficient, C_D is modeld with the Gidaspow [89] variation of the Schiller-Naumann [90] correlation.

The model developed by Mei [91] on the basis of the Saffman's [92] theory and Dandy & Dwyer's [93] simulations is used to predict the lift force acting on single particles immersed in a shear flow. This model correlates the forces caused by the non-uniform distribution of pressures resulting in the transport of particles within a sheared flow. The same is a function of the particle Reynolds number as defined in equation 4.7 and the shear flow Reynolds number defined in equation 4.8:

$$Re_p = \frac{\rho_l\; d_p\; |u_l - u_p|}{\mu_l}, \tag{4.7}$$

$$Re_S = \frac{\rho_l\; d_p^2\; |\omega_l|}{\mu_l}. \tag{4.8}$$

The lift force is defined in equation 4.9

$$F_{LS} = \frac{\rho_l}{2}\frac{\pi}{4}\; d_p^2\; C_{LS}\; d_p\; ((u_l - u_p) \times \omega_l), \tag{4.9}$$

where the lift coefficient takes the form of equation 4.10

$$C_{LS} = \frac{4.1126}{Re_S^{0.5}} f(Re_p, Re_S) \tag{4.10}$$

and $f(Re_p, Re_S)$ is the correction function developed by Mei [91], which takes the following form:

$$f(Re_p, Re_S) = \begin{cases} (1 - 0.3314\ \sqrt{\beta_{LS}})e^{-Re_p/10} + 0.3314\ \sqrt{\beta_{LS}} & \text{if } Re_p \leq 40, \\ 0.0524\sqrt{\beta_{LS}\ Re_p} & \text{if } Re_p > 40, \end{cases} \tag{4.11}$$

where β (eq. 4.12) is half the ratio of the shear flow Reynolds number and the particle Reynolds number

$$\beta = 0.5\frac{Re_S}{Re_p}. \tag{4.12}$$

4.2 CFD-DEM method

The CFD-DEM approach is based on an Eulerian-Lagrangian description of the liquid and particle phases, where the liquid phase is solved through a finite volume method discretization of the Navier-Stokes equations and the solid phase is modelled by applying Newton's laws of motion to discrete particles. The basis implementation used here is the one developed by Goniva at al. [94] and also available in the open-source code CFDEM version 2.6.1. Particles are considered to be smooth and perfectly spherical. Constitutive equations describing phenomena at sub-grid scales are used to close the conservation equations analogously to the Two-Fluids method. Since the transport of cuttings may eventually present concentrations above those observed in semi-dilute suspensions, i.e. in particle accumulations or deviated sections, it is deemed convenient to use models also describing particle interactions. Such description is known as four-way coupling and it is a more exhaustive way to consider momentum transfer in suspensions in comparison to other approaches.

The liquid phase is described using volume-averaged, incompressible, transient Navier-Stokes equations, analogous to the description of the liquid phase in the two-fluid method. Indeed the part modelling the liquid is based on the same continuum approach as the one used in the two-fluids formulation. The volume-averaged continuity equation is given by:

$$\frac{\partial}{\partial t}(\phi_l \rho_l) + \nabla \cdot (\phi_l \rho_l u_l) = 0, \tag{4.13}$$

where u_l is the liquid velocity vector, ρ_l is the density and the concentration of the liquid phase, ϕ_l, satisfies the constraint:

$$\phi_l + \phi_s = 1, \tag{4.14}$$

where ϕ_s is the concentration of the solid phase. The momentum balance for for the liquid phase is given by the Navier-Stokes equation:

$$\frac{\partial}{\partial t}(\phi_l \rho_l u_l) + \nabla \cdot (\phi_l \rho_l u_l u_l) = -\phi_l \nabla p + \phi_l \nabla \cdot \tau_l + \phi_l \rho_l g - F_{tot}, \tag{4.15}$$

modified to include an inter-phase momentum transfer term, also analogous to the description of the liquid phase in the two-fluid method. In this case, we follow the recommendations by Zhou et al. [65] explained in section 2.4.2 and only present the model type A, where the pressure source term is shared by both the the liquid and solid phases. In equation 4.15, p is pressure, g is the gravitational acceleration vector, τ_l is the viscous stress tensor and F_{tot} is the total interfacial momentum transfer per unit volume made up of the drag force, F_d, the lift force, F_l and the virtual mass force F_{vm}. Also in this case, depending on the relevant interactions, other sources of force may be added.

On the other hand, we have the Lagrangian formulation of the discrete phase. As described by Zhou et al. [65], at any time t, "the equations governing the translational and rotational motions of particle i with radius R_i, mass m_i and moment of inertia I_i can be written as

$$m_i \frac{dv_i}{dt} = f_{pf,i} + \sum_{j=1}^{k_i} (f_{c,ij} + f_{d,ij}) + m_i g, \tag{4.16}$$

$$I_i \frac{d\omega_i}{dt} = \sum_{j=1}^{k_i} (M_{t,ij} + M_{r,ij}), \tag{4.17}$$

where v_k and ω_k are, respectively, the translational and angular velocities of the particle, k_c is the number of particles in interaction with the particle. The forces involved are: the particle-fluid interaction force $f_{pf,i}$, the gravitational force $m_i g$, and inter-particle forces between particles that include the elastic force $f_{c,ij}$ and viscous damping force $f_{d,ij}$. The torque acting on particle i by particle j includes two components: $M_{t,ij}$, generated by the tangential force, and $M_{r,ij}$, commonly known as the rolling friction torque." Morevover, Zhou et al. [65] define the particle-fluid interaction forces $f_{pf,i}$ as "the sum of all types of particle-fluid interaction forces acting on individual particles by fluid including the drag force f_d, pressure gradient force $f_{\nabla p}$, viscous force $f_{\nabla \cdot \tau}$ due to the fluid shear stress or deviatoric stress tensor, virtual mass force f_{vm}, Basset force f_B and lift forces such as the Saffman force f_{Saff} and Magnus force f_{Mag} [95]. " The total particle-fluid interaction force for particle i is then expressed as

$$f_{pf,i} = f_d + f_{\nabla p} + f_{\nabla \cdot \tau} + f_{vm} + f_B + f_{Saff} + f_{Mag}. \tag{4.18}$$

Whereas the total interfacial momentum transfer F_{tot} is obtained by adding the total particle-fluid interaction forces $f_{pf,i}$ of all the particles found in a cell described as

$$F_{tot} = \frac{1}{\Delta V} \sum_{i=1}^{n} (f_{d,i} + f_{\nabla p,i} + f_{\nabla \cdot \tau,i} + f_{vm,i} + f_{B,i} + f_{Saff,i} + f_{Mag,i}), \tag{4.19}$$

where ΔV is the volume of a computational cell and n is the total number of particles in that particular cell.

4.2.1 Inter-phase coupling

The CFDEM solver brings together information coming from the liquid side and information coming from the particle side. This coupling is performed through the volume fraction and the inter-phase momentum exchange. In this section, the default models available in CFDEM are presented and commented in relation to the relevant parameters for simulations of cuttings transport.

4.2.1.1 Volume fraction models

The volume fraction models in CFDEM are described as void fraction models. Other authors [65, 67, 96] call them porosity models. The objective of these models is to transfer the information about the particle locations from the Lagrangian representation to the Eulerian representation. This is done through the volume fraction calculation, which is a scalar field of the Eulerian part of the solution.

The most straightforward option is the "centred" volume fraction calculation, which receives the name `centreVoidFraction` in the CFDEM library. In this model, the complete volume of the particle is assigned to the cell occupied by this particle's center and is calculated as follows:

$$\phi_{l,cell} = 1 - \frac{1}{V_{cell}} \sum_{\forall \in cell} V_p^i. \tag{4.20}$$

where V_{cell} is the volume of the cell and V_p is the volume of the particle. According to Goniva et al. [97] this approach can lead to erroneous results due to artificially inhomogeneous volume fraction field when particle size approaches cell size.

To produce smoother exchange fields, the `dividedVoidFraction` model is recommended. In this approach, firstly introduced by Hoomans *et al.* [66], the volume of the particle is divided between all cells covered by the particle. This is accomplished through resolution of the particle by a series of distributed marker points. The liquid volume fraction is calculated then as:

$$\phi_{l,cell} = 1 - \frac{1}{V_{cell}} \sum_{\forall \in cell} f_{cell}^i V_p^i, \tag{4.21}$$

where f_{cell}^i is the fractional volume of particle i residing in the cell under consideration. The method works well when the size of the grid cells is much larger than that of the particles.

Sometimes it is desirable to use small computational cells to resolve all relevant details of the fluid field and obtain a grid-independent solution. This is, in principle, contradictory to the requirement of working with cells larger than the particle size. To overcome this problem, the `bigParticleVoidFraction` oder the `GaussVoidFraction` models are indicated. On one hand, the `bigParticleVoidFraction` model sets the void fraction of the cells with centres within the particle to null. This produces a stairstep representation of the of the bodies, which requires eight cells per diameter resolution to obtain accurate results. On the other hand, the `GaussVoidFraction` model distributes the volume of the particle in cells whose centres are inside the particle.

For the `dividedVoidFraction`, the `bigParticleVoidFraction` and the `GaussVoidFraction`, as described in the CFDEM manual: "the region of influence of a particle can be increased artificially by porosity, which blows up the particles, but keeps their volume constant" [98]. This is similar to a method introduced by Link et al. [99], where they artificially distribute the volume of the particle on cells located within a porous cube with a volume equal or larger to particle under consideration. By doing this, the presence of the particle is felt relatively weakly in a larger portion of the flow domain and consequently, grid refinement does not lead to local extremes in the liquid fraction around the center of mass of the particle [67].

4.2.1.2 Inter-phase momentum exchange

In a non-resolved approach, the inter-phase momentum exchange requires parameter models to calculate the particle-fluid interaction forces $f_{pf,i}$. Several correlations have been proposed for the drag force, the lift force or the virtual mass force as already introduced in section 2.2. In this section, the ones offered in the CFDEM library are reviewed and commented with respect to the use in simulations of coarse settling suspensions.

Drag Force The drag force acting on a suspended particle is proportional to the relative velocity between the phases and has the following form:

$$f_d = \frac{1}{2} C_d \rho_l A_p |u_l - u_p| (u_l - u_p), \tag{4.22}$$

where A_p is the cross-sectional area of the particle to the direction of the incoming flow and C_d is the drag coefficient. CFDEM offers different default correlations to obtain the effective drag coefficient: Schiller & Naumann [90], Gidaspow [89], Koch & Hill [62] and Di Felice [100]. The selection of the different correlations available is mostly dependent on the similarity of the investigated experimental systems and the simulated system.

According to Sommerfeld et al. [101] the Schiller & Naumann [90] correlation fits experimental data of a single spherical particle settling in a quiescent fluid for Re_p up to 1000 reasonably well

$$C_d = \frac{24}{Re_p}(1 + 0.15 Re_p^{0.687}). \tag{4.23}$$

Therefore, it is commonly used in the dilute suspension regimes defined by Michaelides [102] as those where particle average separation is greater than two diameters. The Schiller & Naumann [90] correlation is commonly combined with the solution of the Stokes-regime

$$C_d = \frac{24}{Re_p} \tag{4.24}$$

and the asymptotic value reached above $Re_p = 1000$

$$C_d \approx 0.44, \tag{4.25}$$

known as the Newton-regime. In the CFDEM library, the default implementation calculates both the Schiller & Naumann [90] drag and the value of the Newtonian-regime and takes the largest value of the two.

For dense suspension regimes, the drag exerted by a single particle on the continuous phase needs to consider the effects of concentration. In some cases, this is done through the inter-phase momentum transfer coefficient β_{MT}. This coefficient can be analytically derived for spherical particles. Considering the drag exerted by a single particle on the continuous phase given in equation 4.22, the area A_p and volume V_p of a spherical particle

$$A_p = \frac{\pi d_p^2}{4}; \tag{4.26}$$

$$V_p = \frac{\pi d_p^3}{6}, \tag{4.27}$$

and the number of spherical particles per unit volume

$$n_p = \frac{\phi_s}{V_p} = \frac{6\phi_s}{\pi d_p^3}, \tag{4.28}$$

the total inter-phase momentum transfer due to drag per unit volume can be expressed as

$$F_d = n_p f_d = \frac{3}{4}\frac{C_d}{d_p}\phi_s \rho_f |u_{pi} - u_l|(u_{pi} - u_l). \tag{4.29}$$

This inter-phase momentum transfer is also defined as

$$F_d = \beta_{MT}(u_{pi} - u_l). \tag{4.30}$$

Therefore, the inter-phase momentum transfer coefficient takes the following form

$$\beta_{MT} = \frac{3}{4}\frac{C_d}{d_p}\phi_s \rho_f |u_{pi} - u_l|. \tag{4.31}$$

Combining equations 4.29 and 4.31, the drag force exerted by a single particle on the continuous phase as a function of β_{MT} is obtained

$$f_d = \frac{V_p \beta_{MT}}{\phi_s}(u_{pi} - u_l). \tag{4.32}$$

The Gidaspow [89] and the Koch & Hill [62] are drag models implemented in CFDEM correlating β_{MT} with solid volume fraction ϕ_s and particle Reynolds number Re_p. The Gidaspow [89] drag model is a widely used combination of the Ergun [103] equation for dense regimes ($\phi_s > 0.2$)

$$\beta_{MT} = 150\frac{\phi_s^2 \mu_f}{(1-\phi_s)d_p^2} + 1.75\phi_s \rho_f |u_{pi} - u_l|, \tag{4.33}$$

and the correlation proposed by Wen & Yu [104] for more dilute regimes ($\phi_s < 0.2$)

$$\beta_{MT} = \frac{3}{4}C_d \frac{\phi_s(1-\phi_s)\rho_f}{d_p}|u_{pi} - u_l|(1-\phi_s)^{-2.65}, \tag{4.34}$$

where the drag coefficient C_d is obtained from the Schiller & Naumann [90] correlation for $Re_p < 1000$ and from equation 4.25 for $Re_p > 1000$.

The correlation of Koch & Hill [62] is a more recent model based on lattice-Boltzmann simulations:

$$\beta_{MT} = \frac{18\mu_f(1-\phi_s)^2\phi_s}{d_p^2}(F_0(\phi_s) + \frac{1}{2}F_3(\phi_s)Re_p), \tag{4.35}$$

with:

$$F_0(\phi_s) = \begin{cases} \dfrac{1 + 3\sqrt{\frac{\phi_s}{2}} + \frac{135}{64}\phi_s ln(\phi_s) + 16.14\phi_s}{1 + 0.681\phi_s - 8.48\phi_s^2 + 8.16\phi_s^3} & \text{if } \phi_s < 0.4 \\ \dfrac{10\phi_s}{\phi_f^3} & \text{if } \phi_s \geq 0.4 \end{cases}; \tag{4.36}$$

$$F_3(\phi_s) = 0.0673 + 0.212\phi_s + \frac{0.0232}{\phi_s^5}. \tag{4.37}$$

Di Felice's [100] drag model also considers the effect of concentration. However, differently from the models by Gidaspow [89] and Koch & Hill [62], this is done through the modification of the single particle drag coefficient C_{d0} by a correlation term dependent on the solid volume fraction

$$C_d = C_{d0}(1-\phi_s)^{-K} \tag{4.38}$$

with

$$K = 3.7 - 0.65e^{[-\frac{(1.5-logRe)^2}{2}]}. \tag{4.39}$$

This is a more modern version of the Richardson & Zaki [105] term considering several sets of experiments, including those by Richardson & Zaki [105] and Wen & Yu [104]. In the CFDEM implementation, C_{d0} is calculated through the Dallavalle correlation [100]

$$C_{d0} = (0.63 + \frac{4.8}{Re_p^{0.5}})^2. \tag{4.40}$$

The selection of one of the previous drag models is based on the similarity between experiments used to perform the fittings and the simulated system. When this similarity is not given, it is necessary to perform a validation analysis and evaluate if the available models represent reality with the desired accuracy. If this is not the case, one still has the option to implement more recent drag models as the one by Beetstra et al. [63], where bidisperse suspensions are also considered. In any case, this is currently a subject of great research interest and new drag models considering complex situations closer to those found in reality are expected.

Lift force The CFDEM library offers two possibilities in relation to the lift force. Either no modelling or the Mei [91] implementation. The latter is analogous to the one already introduced in section 4.1.1. The activation of the lift force model needs to be evaluated based on the relevancy of this force.

Unsteady forces Of the two unsteady forces appearing in particle transport, the CFDEM library only offers the virtual mass force. Moreover, the available model is only valid for inviscid fluids. Therefore, the default implemented solution cannot be applied to the liquids investigated. On the other hand, it is necessary to evaluate if the virtual mass force is relevant in the simulated systems. This is so when the dispersed objects (particles, drops or bubbles) present lower densities than those of the fluids or the dispersed particles suffer large accelerations. For example in the case of bubbles. For the systems at hand, particles with slightly higher densities than the particles are considered. Likewise, no strong accelerations are expected once the particles reach the transport velocity. Considering the cuttings transport lengths, this is considered to happen in a relatively short time. Therefore, the virtual mass force is deemed as non-relevant in this case.

Archimedes or Buoyancy force The CFDEM library requires modeling of the Buoyancy force because hydraulic pressure is not considered in the discretized equations. In model *type B* the force is also accounted on the CFD side. On the other hand, model *type A* does not account for it. The solver calculates the force by identifying the volume of a specific particle and the density of the fluid at the particle location:

$$f_{buoyancy} = \frac{\pi d_p^3}{6}\rho_f g. \tag{4.41}$$

Depending on the formulation of the drag model selected, this force may be already included. For example Hill, Koch and Ladd [31] define the drag force as the total force on the particle including pressure gradients.

4.2.2 Numerical implementation

As previously commented, the numerical implementation used for the simulations is the open-source code CFDEM described by Goniva et al. [94]. This one couples the LIGGGHTS DEM solver for the particles side with the pisoFOAM CFD solver included in the openFOAM CFD library for the fluid side. LIGGGHTS stands for 'LAMMPS Improved for General Granular Heat Transfer Simulations' and is based on LAMMPS ('Large Atomic and Molecular Massively Parallel Simulator'). On the other side, the pisoFOAM solver is based on a well established pressure -velocity coupling algorithm named "Pressure-Implicit Split-Operator" (PISO) [106]. The coupling routine as described by Goniva el al. [94] is based on the soft-sphere collision model introduced in section 2.4.2 and consists of the following steps:

1. The DEM solver calculates the particle positions and velocities.
2. The particle positions, velocities and other necessary data are passed to the CFD solver.
3. For each particle, the corresponding cell in the CFD mesh is determined.
4. For each cell, the particle volume fraction as well as a mean particle velocity are determined.
5. Based on the particle volume fraction, the fluid forces acting on each particle are calculated.
6. Particle-fluid momentum exchange terms are assembled from particle-based forces by ensemble averaging over all particles in a CFD cell.
7. The fluid forces acting on each particle are sent to the DEM solver and used within the next time step.
8. The CFD solver calculates the fluid velocity taking into account local particle volume fraction and momentum exchange.
9. The routine is repeated from (1).

The routine progresses in time considering time scales of the flow, of the inter-phase coupling and of the particles. These requires a definition of the corresponding time steps. The time-step of the flow, Δt_{flow}, needs to satisfy the Courant-Friedrichs-Lewy (CFL) condition

$$C = \Delta t_{flow} \sum_{i=1}^{3} \frac{u_{x_i}}{\Delta x_i} \leq C_{max}, \tag{4.42}$$

where u_{x_i} is the velocity along every coordinate , Δt_{flow} is the time step of the flow, Δx_i is the length interval or size of the cell along every coordinate and C_{max} is the maximum Courant number. The value of this number depends on the method used to solve the discretized equations. For an explicit (time-marching) solver C_{max}=1 is typically used. Moreover, Δt_{flow} is kept constant to avoid complications in the numerical implementation. The inter-phase coupling, defined by $\Delta t_{coupling}$, is normally performed with the same time-step as the flow. However, this can be done at higher intervals. Finally, in the soft-sphere model also a constant time-step, Δt_{soft}, to update the particle velocities is used. The time-step Δt_{soft} should be sufficiently small to satisfy two criterion: (1) avoiding problems with energy conservation caused by the numerical integration and (2) minimising the propagation of disturbance waves [107].

According to Deen et al. [67], the satisfaction of the first criterion requires examination of the normal and tangential stiffness'. They offer the following justification, where the contact time in the normal and tangential direction need to be considered. Contact time in the normal direction can be determined using

$$t_{contact,n} = \sqrt{m_{ab} \frac{\pi^2 + ln^2(e_n)}{k_n}}, \tag{4.43}$$

where m_{ab} is the reduced mass of two particle and e_n the coefficient of normal restitution. Furthermore, a contact time in the tangential direction is determined using

$$t_{contact,t} = \sqrt{\frac{2}{7} m_{ab} \frac{\pi^2 + ln^2(\beta_0)}{k_t}}, \tag{4.44}$$

where β_0 is the tangential restitution coefficient. To maintain the energy balance, Denn et al. [67] point out the necessity of both contact times to be the same. This requires the satisfaction of the following relation between k_t and k_n:

$$\frac{k_t}{k_n} = \frac{2}{7} \frac{\pi^2 + ln^2(\beta_0)}{\pi^2 + ln^2(e_n)}. \tag{4.45}$$

The normal stiffness k_n is determined from the Young modulus of the material. However, it supplies very high values resulting in very small time steps. Therefore, in common practice lower k_n values providing normal overlap below 1% of the particle diameter are applied.

The satisfaction of the second criterion is satisfied when the chosen time step Δt_{soft} is smaller than a certain fraction of the Rayleigh time defined as

$$T_r = \pi r_p \frac{\sqrt{\rho_p/G}}{0.163\nu + 0.8766}, \tag{4.46}$$

where r_p is the particle radius, ρ_p is the density of the particle, G is the shear modulus and ν_2 is the Poisson ratio. The common guideline is to use around 20% of Rayleigh time. However, no definitive definition exists. Several authors [108], [109], [110], [111] and [112] have proposed fraction of the Rayleigh time, which go from lower than 10% to lower than 40%. The selection of one or the other depends on the velocities of the particles.

5 Experimental results

In this chapter, the measurements performed with Newtonian carrying liquids are explained. It starts with the description of the experimental procedure applied in the vertical multiphase flow-loop, where the necessary steps to acquire experimental data at a stationary state are described. Later on, the processing methods used to extract the necessary information from the acquired data are introduced. In it, the steps necessary to obtain fluid velocity fields and discrete velocities of the particles are explained. Furthermore, the manipulation of the acquired velocities, as well as the particle positions, to obtain locally averaged slip velocities and particle position histograms is introduced. Finally, results are presented in two sections: one dedicated to the experiments performed with monodisperse suspensions and the second one dedicated to experiments with bidisperse suspensions. Conclusions are given in the last section of this chapter.

5.1 Experimental procedure

The experimental procedure consisted of a series of steps to bring the flow loop to a stationary state, where the boundary conditions were characterized in the best possible way. This started by the selection of the particle size and concentration to be introduced in the flow-loop. The necessary amount of particles to obtain the required particle volume was determined with the necessary weight for every particle concentration and species. The electronic mass balance, presented in section 3.4.2.1, was used to perform the measurement. Once this was done, the pump was turned on and a flow rate able to transport the particles was selected. The particles were then introduced and mixed in the section of the flow-loop where multiphase flow takes place. The fluid was circulated until a constant stable temperature was reached and the particles were homogeneously distributed. The temperature was monitored through the thermocouple type K presented in section 3.4.1.1. The normal temperature reached during the experiments, due to friction and heat diffusion from the pump, was around 30 °C. The homogenoeus distribution of the particles was determined acoustically through impacts of the particles flowing through the eductor. A stationary state was assumed once the impacts denoted a stable frequency. At this point, the acquisition of images started by taking 40 images with a frequency of 4 Hz and a pulse separation adapted to the velocity of the fluid at a distance of 1,600 mm from the sudden expansion as shown in figure 5.1. The selection of the pulse separation time was performed in the synchronizer graphical user interface (GUI). After these images were taken, they were saved on the computer to free space from the camera memory. These allowed the acquisition of new images, which this time were acquired at a pulse separation time convenient for the particles velocities. In this case 200 images are acquired. These procedure was carried on until 200 fluid velocity adapted images and 1000 particle velocity adapted images were obtained.

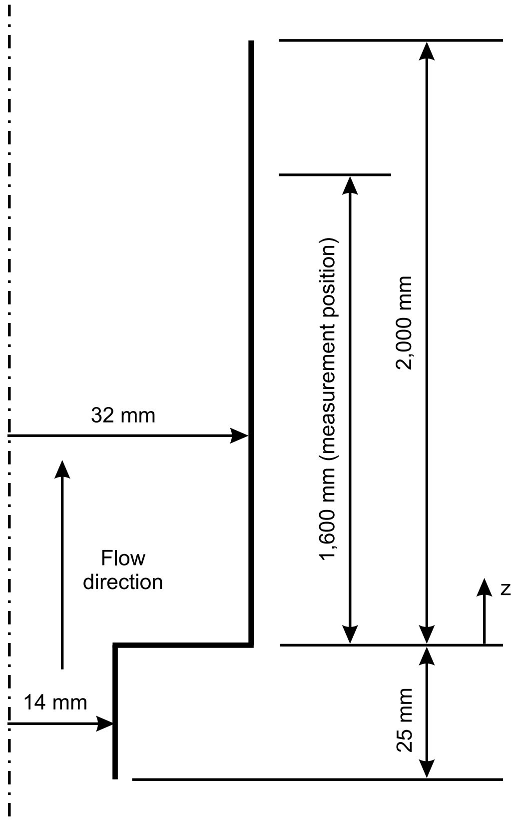

Figure 5.1: Sudden-expansion geometry

The performance of new experiments required either the extraction of the particles in the loop or the addition of new particles. To extract the particles, a higher flow rate to speed the transport of the particles was used. An aquarius fish net was situated at the entrance of the separating container to collect the particles.

5.2 Data processing

5.2.1 Liquid velocity flow-fields

The liquid velocity flow fields were obtained from PIV recordings as the one shown in figure 5.2. In this figure, the laser light propagation is towards the left side of the image and the flow is upwards. The image looks like a typical PIV recording with the only difference being the inclusion of dispersed particles. A cross-correlation algorithm was applied to the PIV recordings of 992 × 864 pixels with a pixel resolution of 65 μm/pixel. The algorithm works on the basis of the direct Fourier transform correlation with multiple passes and deforming windows (PIVlab by Thielicke and Stamhuis [113]). Three passes with three corresponding interrogation windows (64, 32 and 16 pixel) allowed obtaining flow fields consisting of $I = 62$ positions in the radial direction and $J = 54$ positions in the streamwise direction with a maximum average particle displacement of 5.7 pixels/frame. The smallest interrogation window of 16×16 pixels corresponds to an area of approximately 1.04×1.04 mm^2 in the region of interest. For each flow condition $B = 200$ images were taken to obtain the fluid local average vertical velocity at a radial position given by

$$\overline{v_f(r/R)} = \frac{1}{B} \sum_{b=1}^{B} \frac{1}{J} \sum_{j=1}^{J} v_f(r/R)_{(j,b)} \tag{5.1}$$

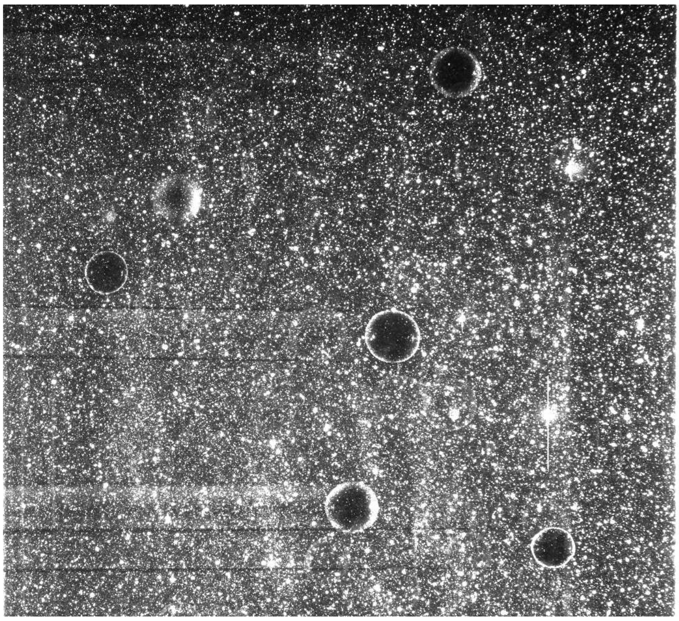

Figure 5.2: Raw image of the exemplary flow field.

The results of the vertical velocities obtained for the exemplary PIV recording presented in figure 5.2 are shown through a contour plot in figure 5.3(a). In the contour plot, velocities close to null on the left and right sides are observed. These correspond to the pipe wall positions . Likewise, it can be seen how the presence of particles notably affects the liquid velocity-fields and produces low velocity regions known as wakes. The intensity of these wakes is also quantified in figure 5.4, where velocity profiles at four different axial positions are shown. In the contour plot, between x = 30 and 40 mm, it is also observed how the flow-field modification caused by one particle intersects with the wake produced by a second particle. While in dilute flows these interactions are not common, in more concentrated ones, interactions between more than two particles are frequent.

The PIV processing of the raw images is affected by the presence of the dispersed particles. Namely, information from the liquid phase velocities is perturbed by dispersed phase velocity information. Such phenomenon is known in the multiphase measuring technique as cross-talking between phases and can affect the accuracy of the measurements. Gui

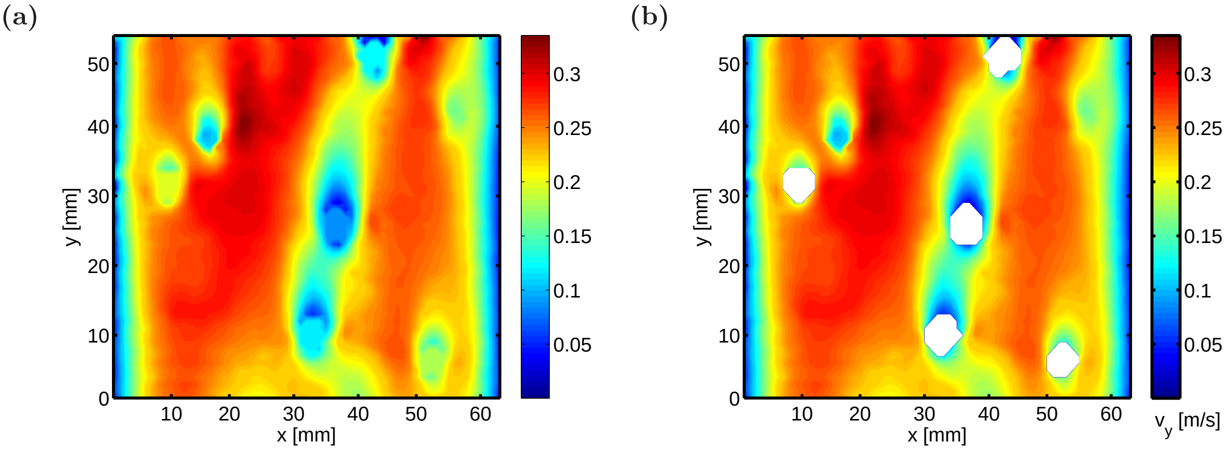

Figure 5.3: Velocity contour plot of the exemplary flow field: (a) without mask and (b) with masks.

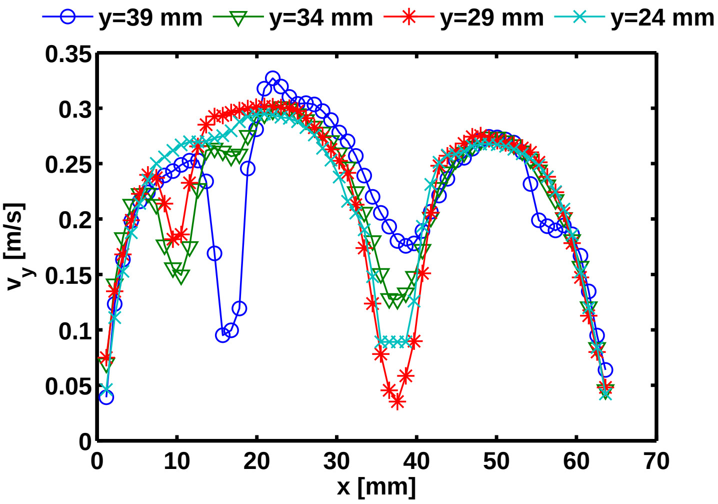

Figure 5.4: Velocity profiles at different positions of the exemplary flow field.

and Merzkirch [58] introduced masking techniques to reduce the effects of cross-talking. However, these techniques are computationally very intensive, because particle positions need to be found for every image and masking images need to be generated and imported during the PIV calculation runs. Considering the amount of images to be processed, it was opportune to evaluate the relevancy of the cross-talking effect. In figure 5.5, a comparison of the average velocity profile obtained with the contour plots of 5.3(a and b) is shown. The differences between the velocity profiles with and without mask are residual in comparison to the velocity fluctuations caused by the particle presence. In figure 5.6, a further evaluation was performed with ten profiles, each corresponding to the average velocity profile obtained from ten images. Also in this figure the relevance of the cross-talking effect can be qualified as unimportant. Therefore, processing of the images was performed without masking techniques.

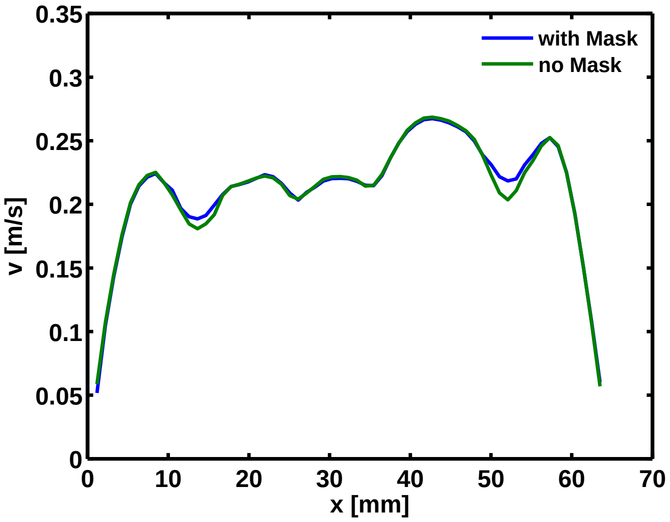

Figure 5.5: Comparison of the average velocity profile obtained from one image with and without mask.

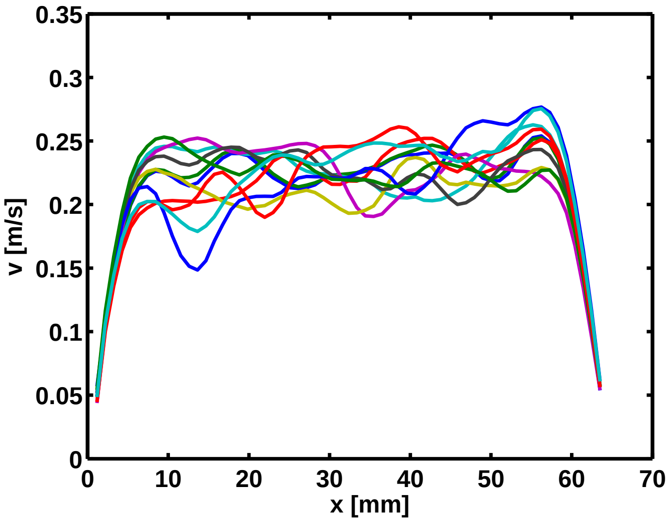

Figure 5.6: Comparison of ten averaged velocity profiles obtained from ten images.

5.2.2 Dispersed particle velocities

The same optical set-up was used for the measurement of the particle positions and velocities. However, in this case longer light pulse separation of 30 ms was necessary to allow larger displacements of the dispersed particles and laser head energies around 50% were sufficient. The images were also taken with an acquisition frequency of 4 Hz.

To obtain the positions of the dispersed particles, an object identification algorithm based on the Hough transform (CircularHough_Grd by Peng [76]) was used. The algorithm output are the center coordinates and diameter of the particles. The settings of the algorithm were selected to recognize only particles showing clear thin edges. As may be observed in figure 5.7, particles falling exactly under the light sheet show clear thin edges. Particles not falling exactly under the center of the light sheet may also be seen. However, these show thicker irregular edges. This difference is used to clearly discriminate the size of the particles. In the same figure 5.7, particle displacement perpendicular to the light sheet is observed through new appearance, disappearance or change of the edge optical condition in the comparison between the frames. Only particles conserving edge optical condition, that is remaining under the center of the light sheet, were tracked. Once coordinates of the particles were known, a PTV algorithm was applied to obtain the velocities of the dispersed phase. Only the particles, which supplied velocity vectors, were used in the data. In other words, only particles detected by the PTV algorithm were used to supply data of the particle positions and velocities. The particle positions were measured from 1000 images obtained in alternating order to the PIV recordings. Particle detection depended very much on the particle concentration. For the lowest concentrations around 500 particles were detected. In case of higher concentrations, quantities around 1500 particles were identified.

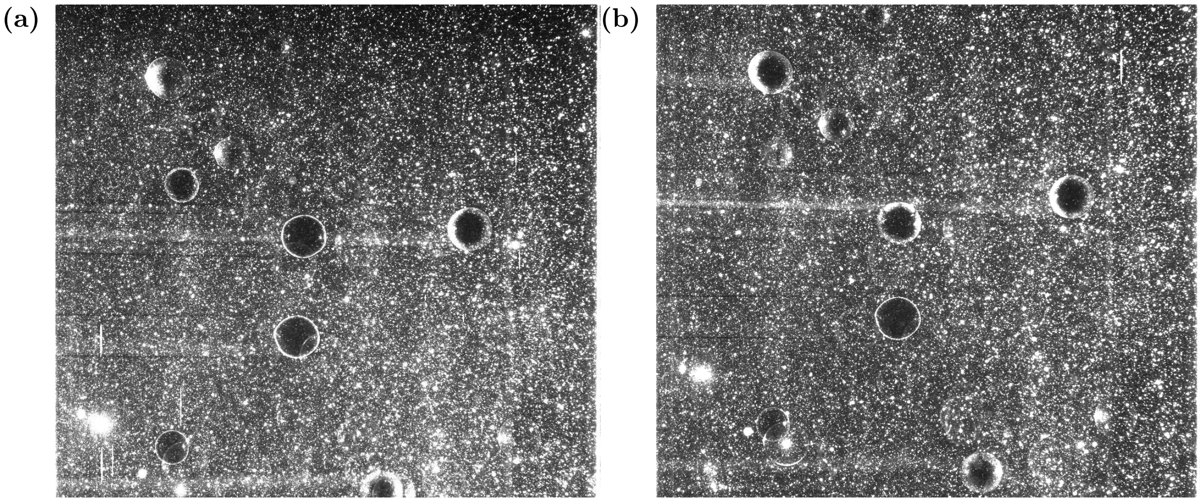

Figure 5.7: Raw images of the exemplary flow field for PTV measurements (a) first frame and (b) second frame.

Local particle average velocities were obtained by averaging at 25 binned positions along the radial coordinate (see also Koh et al. [114]). In the selection of the bin sizes, Crowe [4] gives the following observation: bin sizes must be “large enough to contain many particles, yet small enough to obtain sufficient detail”. The particle local vertical velocities are given by

$$\overline{v_{pi}(r/R)} = \frac{1}{N}\sum_{k=1}^{N} v_{pi}(r/R)_k \tag{5.2}$$

and the standard deviation of the velocities is

$$\sigma_{pi}(r/R) = \frac{(\sum_{k=1}^{N}[(v_{pi}(r/R)_k - \overline{(v_{pi}(r/R)})^2]^{1/2}}{N-1}. \tag{5.3}$$

The standard deviation of the average local velocities is also an indication of the velocity fluctuations of the particles.

5.2.3 Particle distributions

To quantify the particle distributions in the radial direction, histograms of the particle positions were obtained. These histograms were formed by the radial probabilty function of all the measured radial postions r on the longitudinal section and were binned at 25 positions (see Matas et al., [115]), as in the case of the local average particle velocities.

5.3 Experiments performed

The results presented in this work concentrate on mono- and bidisperse suspensions of 2, 4, 5 and 6 mm spherical glass particles. The size of the particles was selected to obtain particle Reynolds numbers (Re_{pi}) in the lower end of the intermediate flow regime around a sphere ($0.2 < Re_p < 500$). The list of experiments, presented in table 5.1, was prepared taking the 4 mm particles for reference. The experiment numbers were assigned chronologically during the measuring campaign. That means experiments shown in the work with 2 and 4 mm particles were performed before the monodisperse experiments with 4 mm particles. The relevant dimensionless parameters are the bulk volume fractions (ϕ_i), where i stands for the size of the particle, the pipe Reynolds number (Re), and the particle Reynolds number (Re_{pi}). These parameters are defined as follows:

$$\phi_i = \frac{\text{particle volume}_i}{\sum \text{particle volume}_j + \text{liquid volume}} \tag{5.4}$$

$$Re = \frac{\rho_f v_n D}{\mu_f} \tag{5.5}$$

$$Re_{pi} = \frac{\rho_f v_s d_{pi}}{\mu_f} \tag{5.6}$$

The pipe Reynolds number is based on the average velocity of a Newtonian fluid at equal flow rate (v_n), D is the pipe diameter, ρ_f is the density of the fluid, μ_f is the dynamic viscosity of the fluid, v_s is the single particle slip velocity evaluated with the Schiller & Naumann drag correlation (eq. 5.7) and d_{pi} is the particle diameter.

$$c_{di} = \frac{24}{Re_{pi}}(1 + 0.15 Re_{pi}^{0.687}) \tag{5.7}$$

Exp.	ϕ_2[%]	ϕ_4[%]	ϕ_5[%]	ϕ_6[%]	*Temp.[°C]*	*Re*	Re_{p2}	Re_{p4}	Re_{p5}	Re_{p6}
7	-	0.12	-	-	29.8	289	-	10.9	-	-
8	-	0.25	-	-	29.8	271	-	10.9	-	-
9	-	0.37	-	-	29.8	270	-	10.9	-	-
10	-	0.50	-	-	29.8	261	-	10.9	-	-
11	-	0.62	-	-	29.3	143	-	10.5	-	-
12	-	0.62	-	-	27.0	183	-	8.8	-	-
14	-	0.62	-	-	27.9	247	-	9.4	-	-
15	-	0.62	-	-	28.3	270	-	9.7	-	-
2	0.25	0.25	-	-	24.5	130	1.4	7.1	-	-
4	0.25	0.50	-	-	26.3	160	1.7	8.3	-	-
5	0.25	0.62	-	-	26.8	169	1.8	8.6	-	-
6	0.37	0.62	-	-	27.4	177	1.9	9.0	-	-
20	-	0.62	0.50	-	30.2	257	-	11.2	18.5	-
21	-	0.62	0.62	-	30.2	257	-	11.2	18.5	-
30	-	1.00	1.00	-	30.9	219	-	11.8	19.4	-
37	-	1.50	1.50	-	30.1	203	-	11.1	18.4	-
46	-	1.00	-	0.25	30.2	246	-	11.2	-	27.5
48	-	1.00	-	0.50	30.1	240	-	11.1	-	27.3
52	-	1.00	-	1.00	30.2	224	-	11.2	-	27.4
55	-	1.50	-	1.00	30.0	219	-	11.0	-	27.1
62	-	2.00	-	2.00	30.7	235	-	11.6	-	28.4

Table 5.1: List of experiments presented

Experiments 7 to 15 are related to monodisperse suspensions of 4 mm particles, whereas experiments 7 to 10 were performed keeping constant pump velocity and varying the bulk volume fraction (φ_4), and experiments 11 to 15 were performed keeping a constant bulk concentration $\varphi_4 = 0.62\%$ and varying volumetric flow rates. These experiments were performed to evaluate the validity of the measurement technique and to supply reference results which may be compared to the results with bidisperse suspensions. Correspondingly, experiments 2 to 6 were performed with 2 and 4 mm particles, experiments 16 to 38 correspond to bidisperse suspensions of 4 and 5 mm particles and experiments 39 to 62 were performed with 4 and 6 mm particles.

5.4 Results of monodisperse flow [1]

The main objective of the monodisperse results was to validate the measuring technique used to obtain average settling velocities in dynamic fluids. The four particle sizes were measured at dilute concentrations to compare the results with available state-of-the-art correlations. For an accurate comparison, particle sizes and sphericities were measured with the QICPIC method. The results were already shown in subsection 3.2.1. Furthermore, several analysis were performed to investigate the behaviour of monodisperse suspensions in the experimental set-up. This was used to supply a reference for the bidisperse suspension experiments.

---

[1] Preliminary results were published in a paper for the International Journal of Multiphase Flow [77].

5.4.1 Concentration variation

The first set of experiments is focused on the analysis of 4 mm particles. In these experiments the pump velocity was set constant. Figures 5.8(a and c) show the average vertical velocity of the fluid and the discrete vertical velocities of the acquired particles non-dimensionalized with the centerline velocity of a Newtonian fluid at the volumetric rate obtained in the experiment (v_{n0}). A comparison of the figures allows the observation of blunter velocity profiles for higher particle concentrations. In addition, it can be observed how the increase in concentrations causes the particles to occupy wider spaces in the radial direction. The histograms showing the probability distribution function $P(r/R)$ can be found in figures 5.8(b and d). Here, a marked concentration of the particles into a central core with clear surrounding annulus of the liquid is observed. This is in agreement with observations made by Newitt et al. [116] and Toda et al. [117] for pebbles flowing in water at high velocities and with other previous experimental and theoretical studies for particles lagging the flow; cf. (Jeffrey & Pearson [118], Aoki et al. [38] or Hogg [119]). The migration of the particles away from the walls is due to the higher shear rates found close to the walls. Quantification of the absolute value of the shear rate is included in the histograms for direct comparison. On the other side, the increase in concentrations flattens the velocity profiles and allows particles to reach positions closer to the walls.

Figures 5.9(a-d) show average velocities and the corresponding standard deviations. In table 5.2, averages of the local standard deviations are listed for every experiment. For this particular analysis no consistent trend can be recognized. However, comparison with bidisperse suspension systems clearly indicates a lower fluctuating degree in the case of monodisperse systems. The particle velocity profiles display slight curvature for low concentrations and become flattened as the concentration is increased following the flattening of the liquid profiles. No significant features are observed in the representation of the fluctuations.

5.4.2 Constant concentrations and varying flow rate

Figure 5.10 shows results obtained in the experiments focused on the analysis of the effects of flow rate variation. In this figure, the vertical velocities are non-dimensionalized with the centreline velocity of a Newtonian fluid at the volumetric rate obtained in experiment 15, the maximum flow rate in this series. Figure 5.10(a) corresponds to the fluidized state flow rate. In this figure a relatively wide distribution of the particles is observed. Moreover, particles with velocities clearly higher than the average ones were also found. More details on the particle distribution of this system are shown on figure 5.10(b), where a homogeneous distribution of the particles is observed. Peaks on the extreme positions are also identified. In figures 5.10(c and d) the effect of an increase in the flow rate is clearly seen in the velocity profiles. Although these are still blunted, the plateau decreases its radius. Consequently, larger regions of the cross section resemble the Newtonian parabolic profile. This also results in lift forces able to push the particles to more concentrated central cores.

As in the case of constant pump velocity experiments, binned particle average velocities

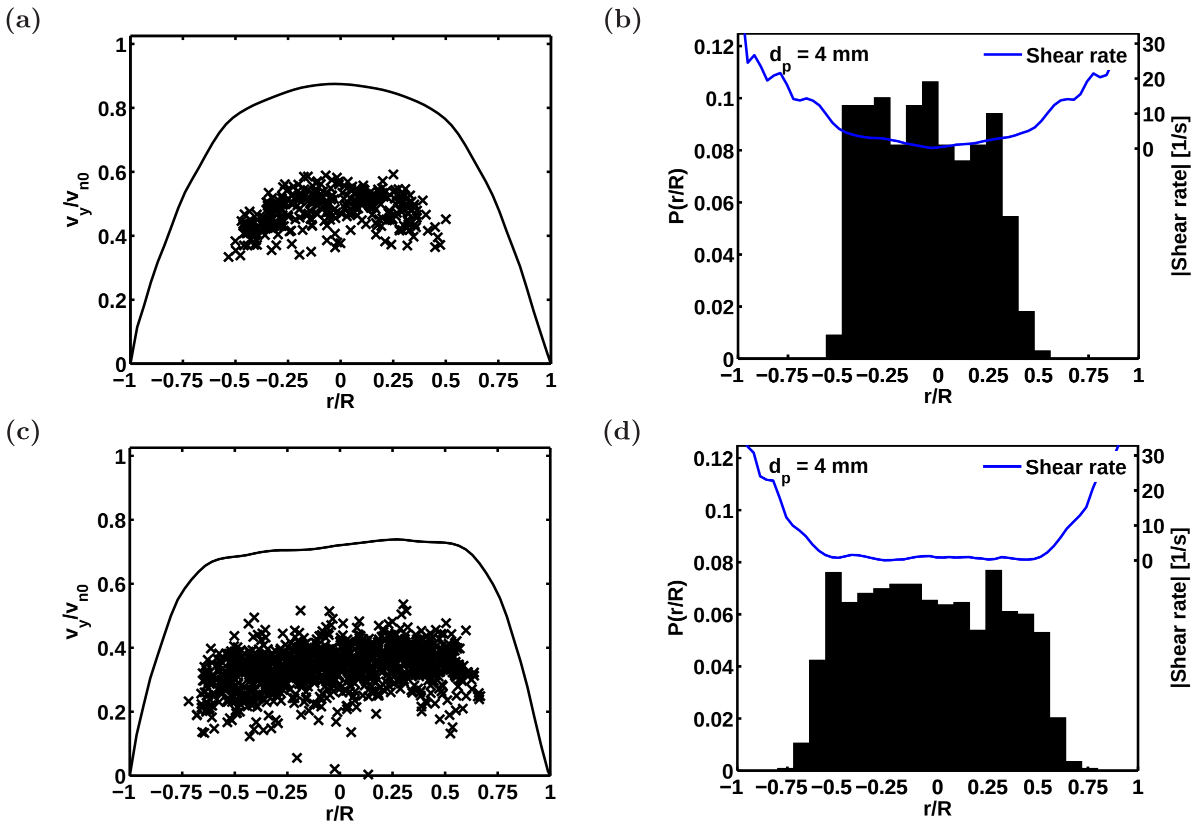

Figure 5.8: Vertical velocities of the 4 mm particles and normalized histograms of the particle positions for varying concentrations and constant pump velocity. ×, vertical velocities of the 4 mm particles, —, locally averaged fluid velocity profile: (a and b) exp. 7, $\phi_4 = 0.12\%$, (c and d) exp. 10, $\phi_4 = 0.50\%$.

and its standard deviations were obtained. In figure 5.11(a) average particle velocities close to 0 are observed, with significant fluctuations in both the upward and downward direction. Results for increasing flow rates are shown in figures 5.11(b-d), where flattened particle velocity profiles are observed. Regarding the quantitative values of the fluctuations, in table 5.2 no significant differences to the values obtained for the concentration analysis of the monodispere systems may be observed. Furthermore, fluctuations for a constant concentration remain essentially constant independently from the fluid flow rate.

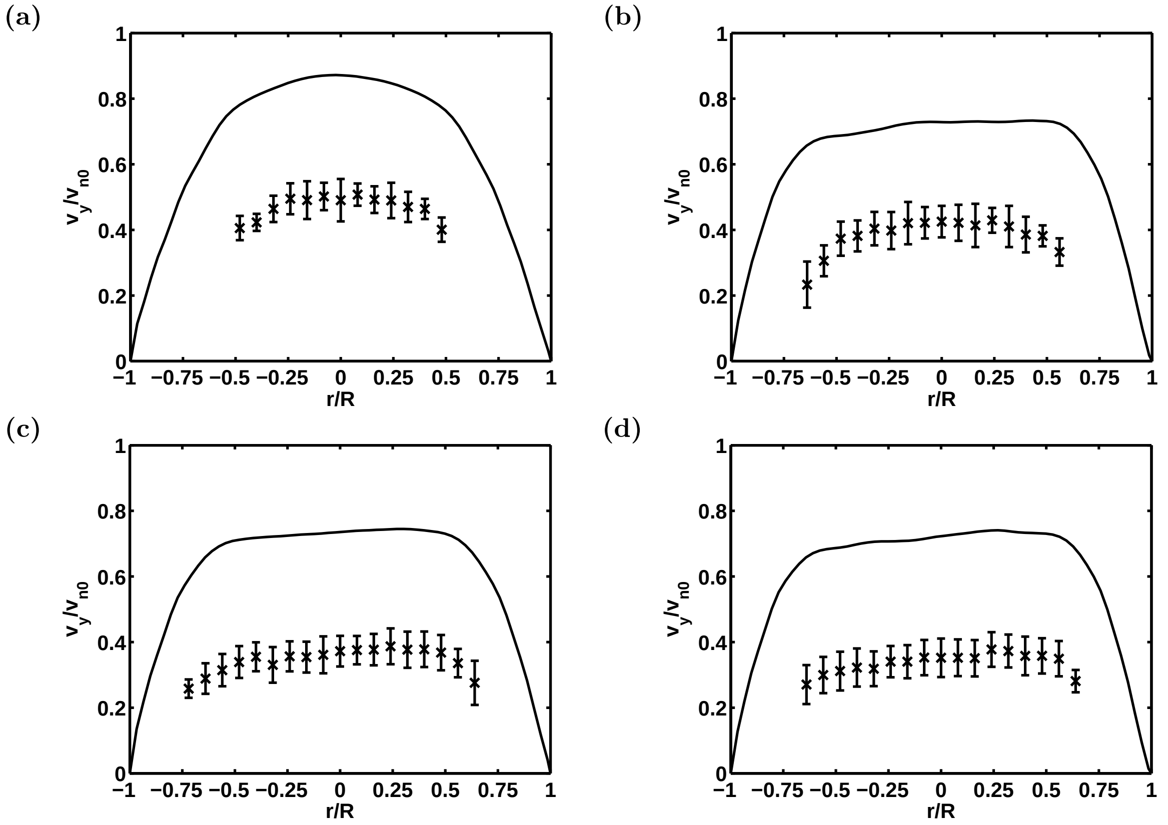

Figure 5.9: Fluid and particle velocity profiles for varying concentrations and constant pump velocity. ×, average vertical velocities of the 4 mm particles, I, standard deviation for particles velocity, —, fluid velocity profile: (a) exp. 7, $\phi_4 = 0.12\%$, (b) exp. 8, $\phi_4 = 0.25\%$, (c) exp. 9, $\phi_4 = 0.37\%$, and (d) exp. 10, $\phi_4 = 0.50\%$.

Exp.	ϕ_2[%]	ϕ_4[%]	ϕ_5[%]	ϕ_6[%]	$\overline{\sigma_{p2}}$ [m/s]	$\overline{\sigma_{p4}}$[m/s]	$\overline{\sigma_{p5}}$[m/s]	$\overline{\sigma_{p6}}$[m/s]
7	-	0.12	-	-	-	0.015	-	-
8	-	0.25	-	-	-	0.021	-	-
9	-	0.37	-	-	-	0.018	-	-
10	-	0.50	-	-	-	0.019	-	-
11	-	0.62	-	-	-	0.021	-	-
12	-	0.62	-	-	-	0.019	-	-
14	-	0.62	-	-	-	0.021	-	-
15	-	0.62	-	-	-	0.022	-	-
2	0.25	0.25	-	-	0.021	0.025	-	-
4	0.25	0.50	-	-	0.027	0.023	-	-
5	0.25	0.62	-	-	0.033	0.021	-	-
6	0.37	0.62	-	-	0.040	0.026	-	-
20	-	0.62	0.50	-	-	0.035	0.028	-
21	-	0.62	0.62	-	-	0.041	0.030	-
30	-	1.00	1.00	-	-	0.057	0.041	-
37	-	1.50	1.50	-	-	0.043	0.045	-
46	-	1.00	-	0.25	-	0.042	-	0.029
48	-	1.00	-	0.50	-	0.049	-	0.030
52	-	1.00	-	1.00	-	0.069	-	0.037
55	-	1.50	-	1.00	-	0.055	-	0.037
62	-	2.00	-	2.00	-	0.077	-	0.049

Table 5.2: Average of the local standard deviation of the particle velocities

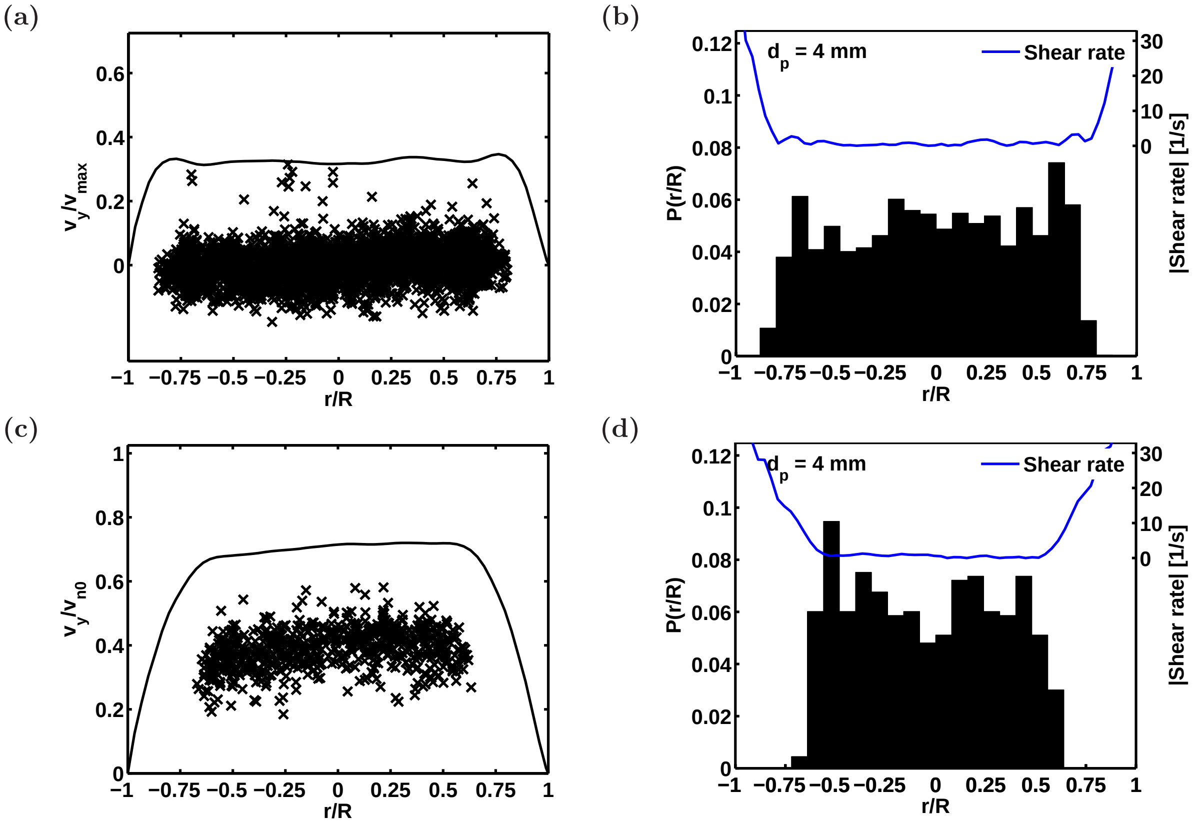

Figure 5.10: Vertical velocities of the 4 mm particles and normalized histograms of the particle positions for constant concentrations and varying flow rate. ×, vertical velocities of the 4 mm particles, —, locally averaged fluid velocity profile: (a and b) exp. 11, $Re = 143$, (c and d) exp. 15, $Re = 270$.

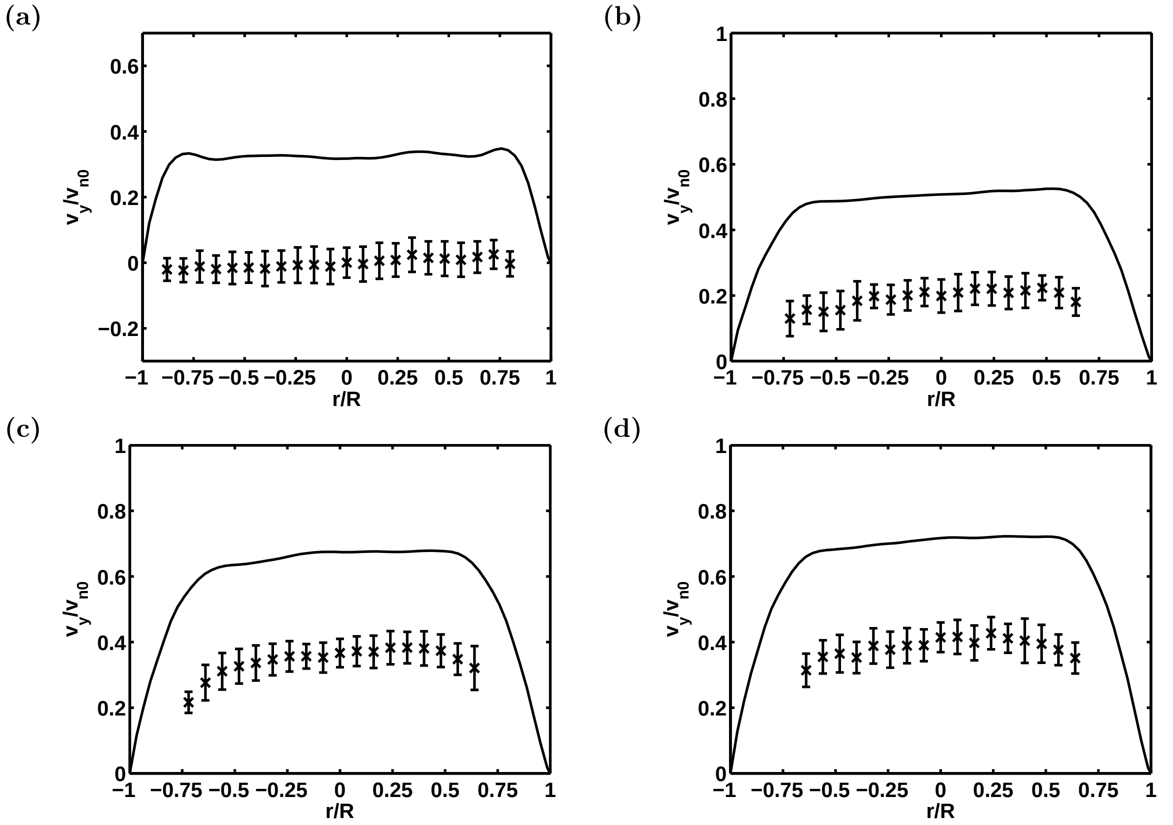

Figure 5.11: Fluid and particle velocity profiles for constant concentrations and varying flow rate. ×, average vertical velocities of the 4 mm particles, I, standard deviation for particles velocity, —, averaged fluid velocity profile: (a) exp. 11, Re = 143, (b) exp. 12, Re = 183, (c) exp. 14, Re = 247, and (d) exp. 15, Re = 270.

5.5 Results of monodisperse flow [2]

5.5.1 Bidisperse suspensions of 2 and 4 mm particles

In this subsection the influence of the addition of smaller particles (d_{p2} = 2 mm) to the reference suspension (d_{p4} = 4 mm) is examined. In figure 5.12 the histograms for 2 different systems (2 and 6) are shown. Figures 5.12(a and c) correspond to 2 mm particles and figures 5.12(b and d) correspond to the 4 mm particles. As in monodisperse suspensions, the increase in concentrations translates in wider histograms. Figure 5.12(a) shows pronounced peaks on the extremes, which may indicate preference of the particles to locate at positions closer to the zone of transition between sloped velocity gradients and the central plateau. It is important to remind that this flat plateau is the result of averaging and the instantaneous velocity gradients in this region are therefore not necessarily zero. A factor that contributes to particle radial velocity fluctuations. Conversely, figure 5.12(b) shows 4 mm particles concentrating around the axis. Higher concentrations translate in more homogeneous distributions in the case of the 2 mm particles, shown in figure 5.12(c), whereas 4 mm particles seem to show a tendency towards the velocity gradient transition as seen in figure 5.12(d). In these systems, the clear liquid surrounding annulus may still be observed, whereas the increase in concentrations reduces its broadness.

Average particle velocities for these systems are shown in figure 5.13. Being the most prominent features the larger velocity fluctuations and average velocities not able to be connected through a smooth profile. Quantification of the fluctuations, shown in table 5.2, indicates moderate increase with larger amount of mixed particles. Furthermore, particle average velocities appear closer to each other for higher concentrations. To quantify this appreciation it is necessary to perform an analysis of the average slip velocities. This is done in a later subsection where it is possible to evaluate the effects of momentum transfer between different species in bidisperse suspensions.

5.5.2 Bidisperse suspensions of 4 and 5 mm particles

This subsection is dedicated to the examination of the inclusion of larger particles (d_{p5} = 5 mm) to the reference suspensions (d_{p4} = 4 mm). Observation of the results for these systems seems to indicate a preferred concentration of the 4 mm particles for the velocity gradient transition. In figure 5.14(a) this tendency may be observed at around $r/R = 0.75$. More homogeneous distributions are observed in experiment 37, where higher concentrations were measured. Furthermore, it can be seen how larger total concentrations result in particles reaching closer positions to the walls. The 5 mm particles shown in figures 5.14(b and d) appear to be more concentrated for lower concentrations to change to more extended distributions as concentration increases.

Again in this case, the average velocities of the particles and its standard deviations are non-dimensionalized with the maximum velocity of the Newtonian velocity profile for the corresponding flow rates (v_{n0}). Increasing concentrations result into flat particle

---

[2] Preliminary results were published in a paper for the International Journal of Multiphase Flow [77].

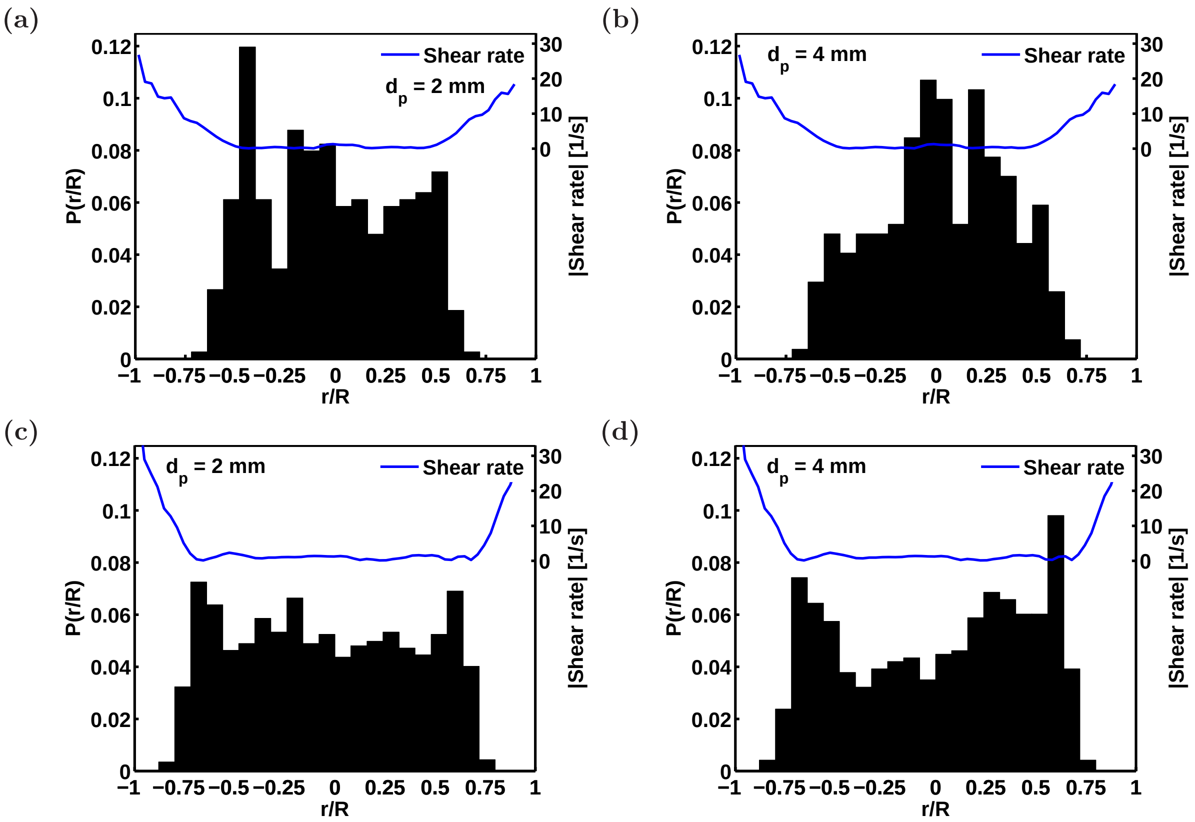

Figure 5.12: Normalized histograms of the particle positions for bidisperse suspensions of 2 and 4 mm particles: (a) exp. 2, $\phi_2 = 0.25\%$, (b) exp. 2, $\phi_4 = 0.25\%$, (c) exp. 6, $\phi_2 = 0.37\%$, and (d) exp. 6, $\phi_4 = 0.62\%$.

velocity profiles parallel to the liquid velocity profiles. Moreover, higher concentrations also translate into more asymmetric fluid velocity profiles. A remarkable feature is the closeness of the average velocities of both species in figure 5.15(c and d). Furthermore, the fluctuations of the longitudinal velocities of both species increase with concentration as shown in table 5.2. With reference to the fluid velocity profiles, peaks at the extremes of the velocity plateau may be observed. The presence of these peaks cause averaged velocity gradients of different sign centered at $r/R = 0.8$, which is an explanation for the preferred concentration at those positions. Also, here an analysis of the slip velocities is necessary to quantify possible momentum transfer between species.

5.5.3 Bidisperse suspensions of 4 and 6 mm particles.

This subsection is again dedicated to the examination of the inclusion of larger particles ($d_{p6} = 6$ mm) to the reference suspensions ($d_{p4} = 4$ mm). In this case, however, the diameter ratio between the included species and the reference object is larger than in the previous subsection and with equal absolute difference with respect to 1 as with the 2 mm mixtures. Figure 5.16(a and b) show a previously seen trend of concentration peaks

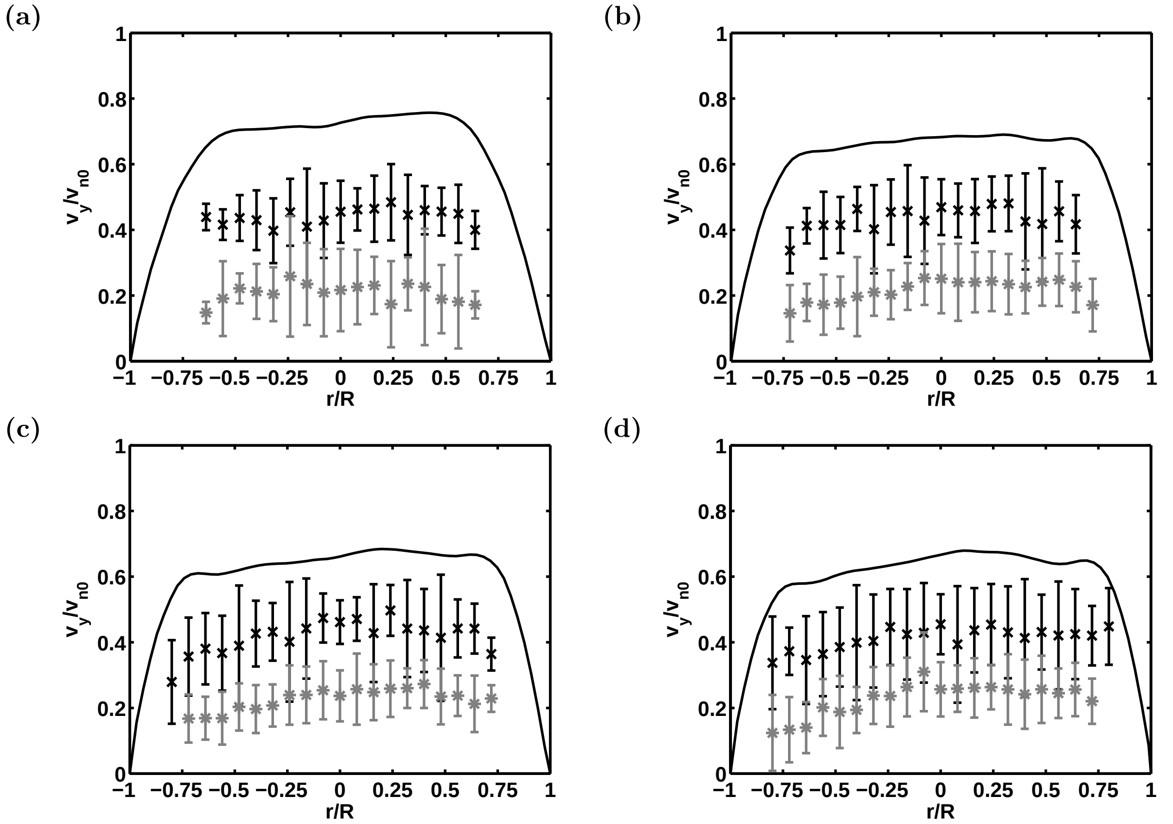

Figure 5.13: Fluid and particle velocity profiles for bidisperse suspensions of 2 and 4 mm particles. ×, average vertical velocities of the 2 mm particles, I, standard deviation for 2 mm particles, *, average vertical velocities of the 4 mm particles, I, standard deviation for 4 mm particles, , fluid velocity profile: (a) exp. 2, $\phi_2 = 0.25\%$, $\phi_4 = 0.25\%$, (b) exp. 4, $\phi_2 = 0.25\%$, $\phi_4 = 0.50\%$ (c) exp. 5, $\phi_2 = 0.25\%$, $\phi_4 = 0.62\%$, and (d) exp. 6, $\phi_2 = 0.37\%$, $\phi_4 = 0.62\%$,.

at $r/R \approx 0.75$ for the 4 mm particles and concentrations maximums centered around the axis for the larger particles. By contrast, figure 5.16(c and d) correspondent to higher total concentrations show more homogeneous distributions.

The average velocities shown in figure 5.17 are in this case significantly different for both species. Similarly to the mixtures with 2 mm particles, the average velocities may not be clearly joined through a smooth profile and the fluctuations of the particle velocities are larger than with monodisperse suspensions or mixtures where the diameter ratio is close to 1. This statement is supported by the values observed in table 5.2. Asymmetric fluid velocity profiles, similar to the ones observed in section 5.5.2, are also observed in these experiments.

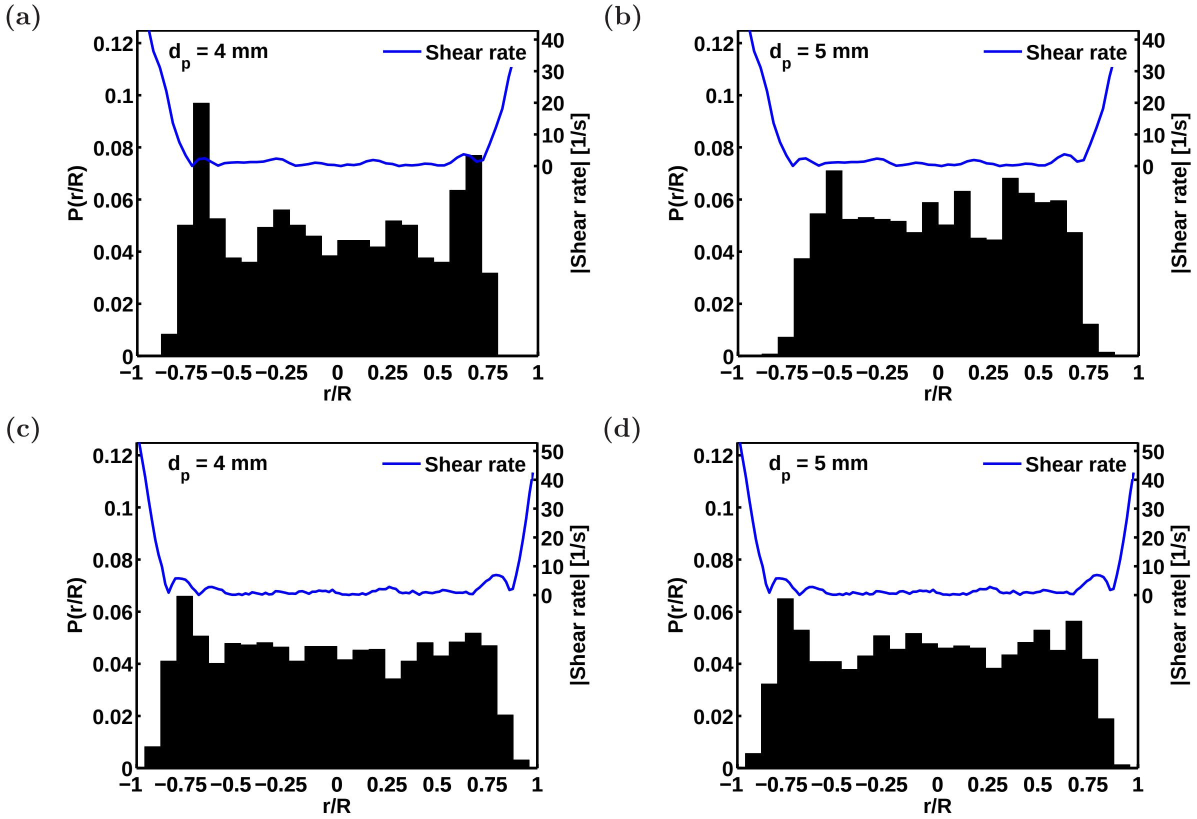

Figure 5.14: Normalized histograms of the particle positions for bidisperse suspensions of 4 and 5 mm particles: (a) exp. 20, $\phi_4 = 0.62\%$, (b) exp. 20, $\phi_5 = 0.50\%$, (c) exp. 37, $\phi_4 = 1.50\%$, and (d) exp. 37, $\phi_5 = 1.50\%$.

5.5.4 Momentum transfer between species

In this subsection the focus is on the momentum transfer between two different particle sizes. Namely, the momentum transferred through the interstitial fluid. For higher concentrations, contact between particles plays a predominant role and it would be difficult to separate one contribution from the other. To examine possible momentum transfer between species in bidisperse suspensions, experimental drag coefficients obtained using equation 5.8 are compared with predicted drag coefficients obtained with well established correlations. Experimental drag coefficients are computed from the average slip velocity between the liquid and dispersed particles via a stationary force balance in the vertical direction:

$$c_d^{exp} = \frac{4}{3} \frac{d_p(\rho_p - \rho_f)|g|}{\rho_f \overline{v_s}^2} \tag{5.8}$$

where ρ_p is the particle density, ρ_f is the fluid density, g is gravity and $\overline{v_s}$ is the average slip velocity given by

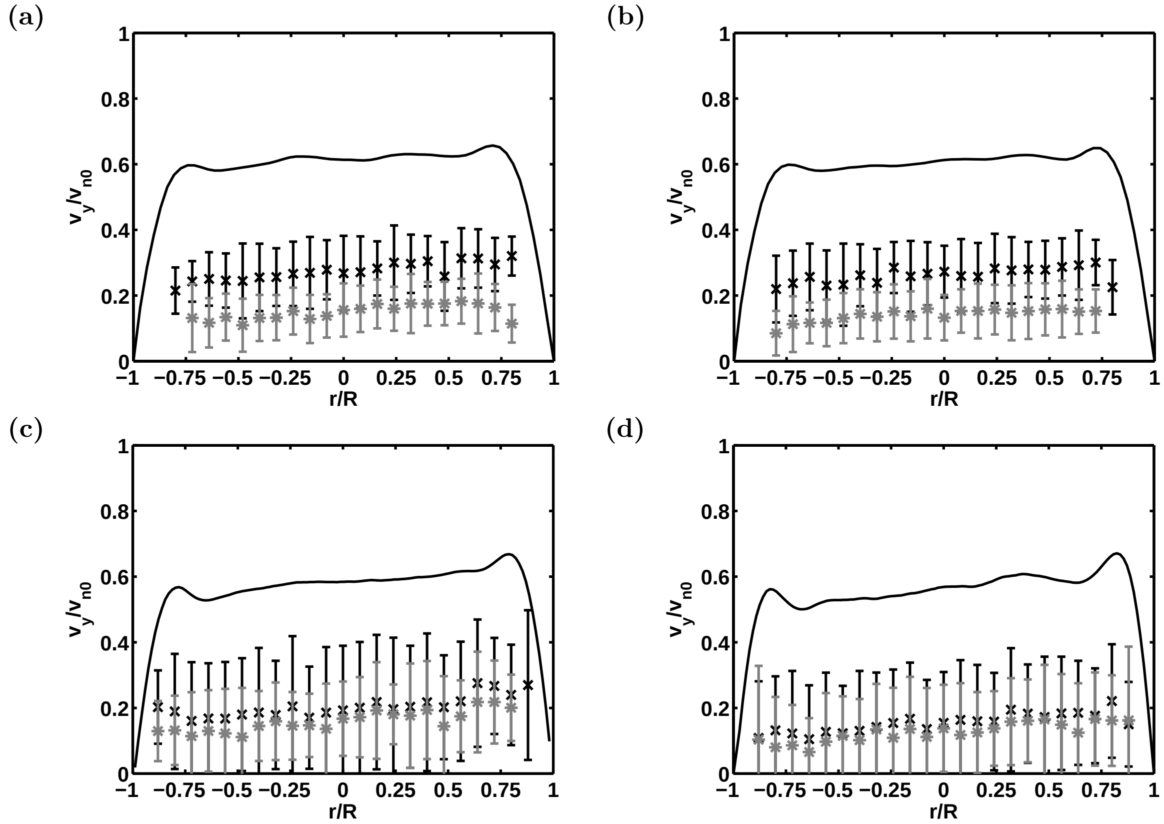

Figure 5.15: Fluid and particle velocity profiles for bidisperse suspensions. ×, average vertical velocities of the 4 mm particles, I, standard deviation for particles velocity, *, average vertical velocities of the 5 mm particles, I, standard deviation for 5 mm particles, —, fluid velocity profile: (a) exp. 20, $\phi_4 = 0.62\%$, $\phi_5 = 0.50\%$, (b) exp. 21, $\phi_4 = 0.62\%$, $\phi_5 = 0.62\%$, (c) exp. 30, $\phi_4 = 1.00\%$, $\phi_5 = 1.00\%$, and (d) exp. 37, $\phi_4 = 1.50\%$, $\phi_5 = 1.50\%$,.

$$\overline{v_s} = \frac{1}{I}\sum_{k=1}^{I}\overline{v_s(r/R)}_k \tag{5.9}$$

where the locally averaged slip velocity $\overline{v_s(r/R)}$ is obtained through the averaged local fluid velocities (eq. 5.1) and the averaged local particle velocities (eq. 5.2)

$$\overline{v_s(r/R)} = \overline{v_f(r/R)} - \overline{v_pi(r/R)} \tag{5.10}$$

Predicted drag coefficients are obtained through the Richardson & Zaki [105] hindered settling function (eq. 5.11). In it, the zero concentration drag c_{d0} is obtained through the Haider & Levenspiel [120] correlation (eq. 5.12), where sphericity Ψ is considered, and the correlation factor K is calculated as described by DiFelice [100](eq. 5.13).

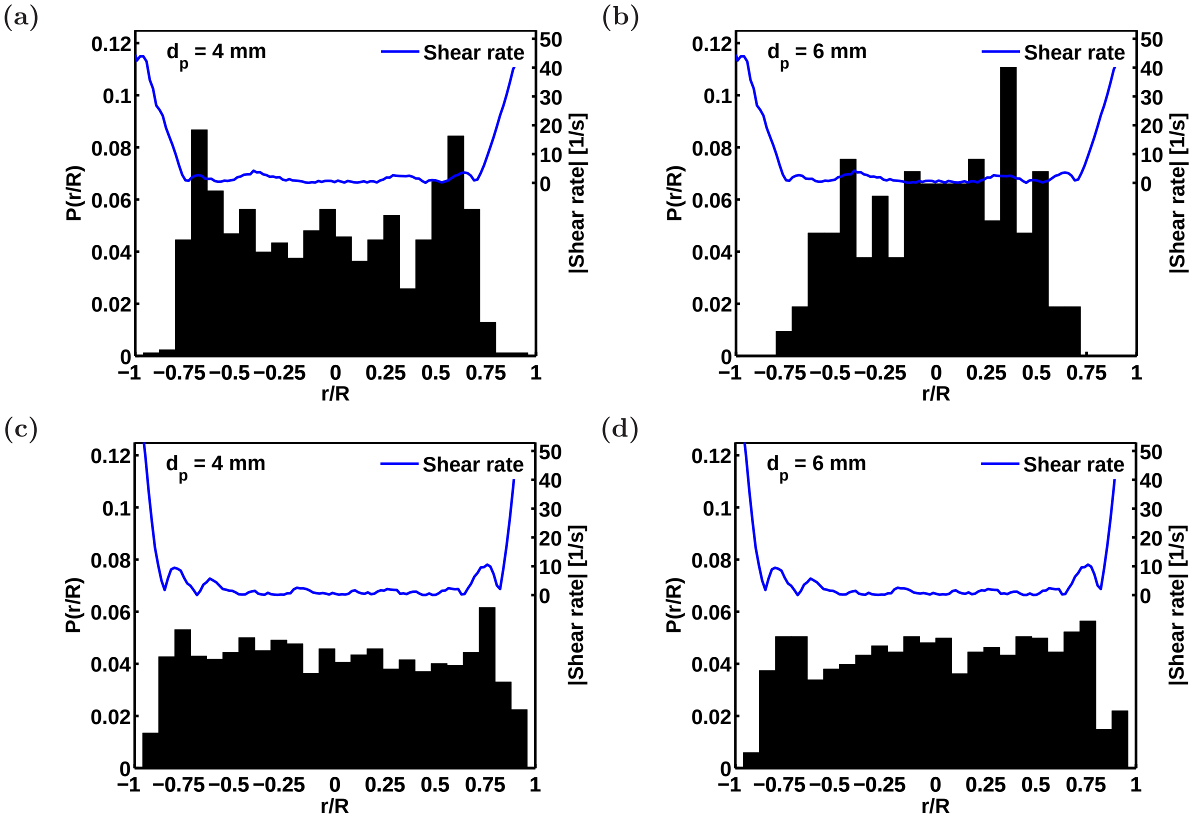

Figure 5.16: Normalized histograms of the particle positions for bidisperse suspensions of 4 and 6 mm particles: (a) exp. 46, $\phi_4 = 1.00\%$, (b) exp. 46, $\phi_6 = 0.25\%$, (c) exp. 62, $\phi_4 = 2.00\%$, and (d) exp. 62, $\phi_6 = 2.00\%$.

$$c_d = c_{d0}(1-\phi)^{-K} \tag{5.11}$$

$$c_{d0} = \frac{24}{Re_p}(1 + ARe_p^B) + \frac{C}{1 + D/Re_p} \tag{5.12}$$

where

A = exp (2.3288 - 6.4581Ψ+2.4486Ψ^2)
B = 0.0964 + 0.5565Ψ
C = exp (4.905 - 13.8944Ψ + 18.4222Ψ^2 - 10.2599Ψ^3)
D = exp (1.4681 – 12.2584Ψ+20.7322Ψ^2 + 15.8855Ψ^3)

$$K = 3.7 - 0.65 \exp\left[-\frac{(1.5 - logRe_p)^2}{2}\right] \tag{5.13}$$

In figure 5.18(a) the comparison for bidisperse suspensions of 2 and 4 mm particles is shown. It must be pointed out that this figure and the ones for the two other mix-

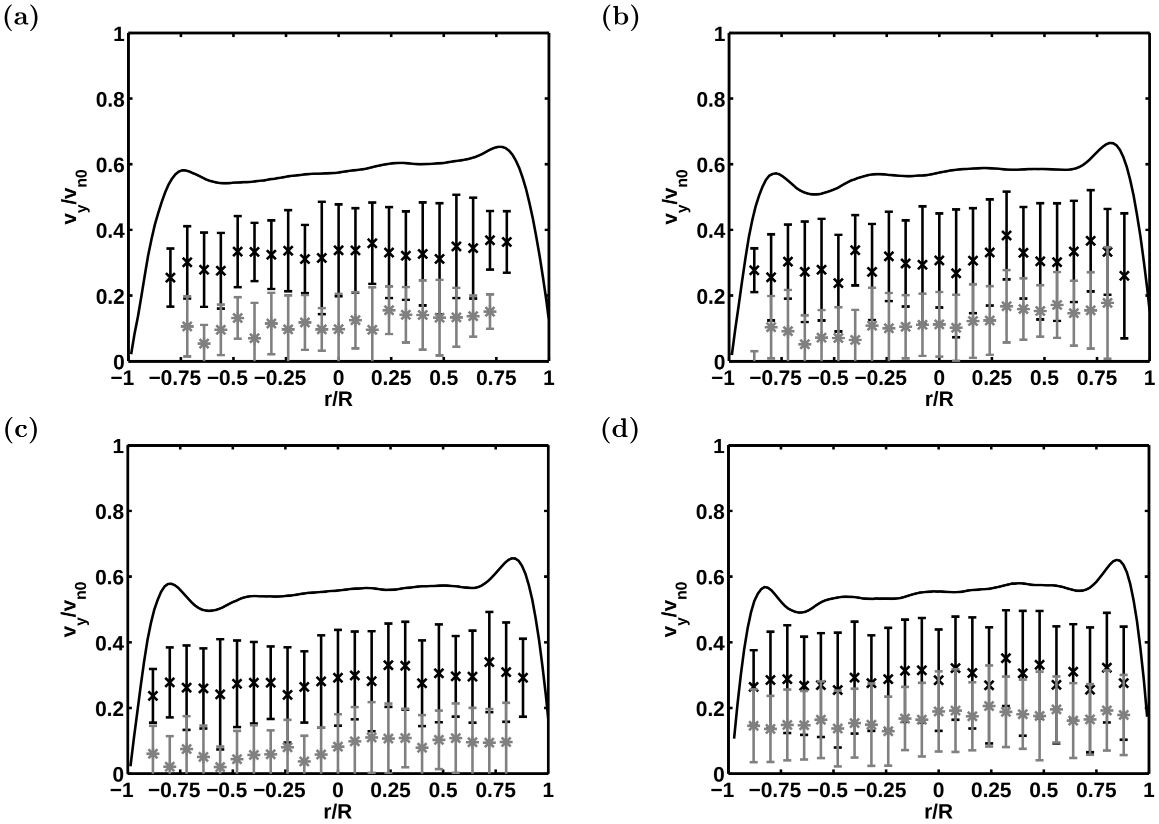

Figure 5.17: Fluid and particle velocity profiles for bidisperse suspensions. ×, average vertical velocities of the 4 mm particles, I, standard deviation for particles velocity, *, average vertical velocities of the 6 mm particles, I, standard deviation for 5 mm particles, , fluid velocity profile: (a) exp. 48, $\phi_4 = 0.62\%$, $\phi_6 = 0.12\%$, (b) exp. 52, $\phi_4 = 0.62\%$, $\phi_6 = 0.25\%$, (c) exp. 55, $\phi_4 = 0.62\%$, $\phi_6 = 0.50\%$, and (d) exp. 62, $\phi_4 = 0.62\%$, $\phi_6 = 0.62\%$,.

tures 5.18(b and c) include all measurements performed in the experimental campaign. Experimental drag coefficients for 2 mm particles seem to be generally lower than the predicted ones. However, as concentration increases tendency to more similar predicted values is observed. Lower experimental drag coefficients than predicted is a sign of hindered transport. On the other hand, 4 mm particles show good agreement for the lower concentrations, whereas increasing concentrations translate into higher drag coefficients than those predicted. This indicates momentum transfer from the 2 mm particles towards the 4 mm particles.

Figure 5.18(b) shows the comparison of the 4 and 5 mm bidisperse suspensions. Good agreement with correlations is observed for total concentrations around 1%. As the total concentration increases, lower experimental drag than predicted was measured for the 4 mm particles. Conversely, 5 mm particles show increasing drag as the total concentration increases. This indicates significant momentum transfer between species. Trend lines estimated with the ordinary least squares technique are added to figures 5.18(b and c) to guide the reader's eye. Nonetheless, these must be regarded with reserve due to the

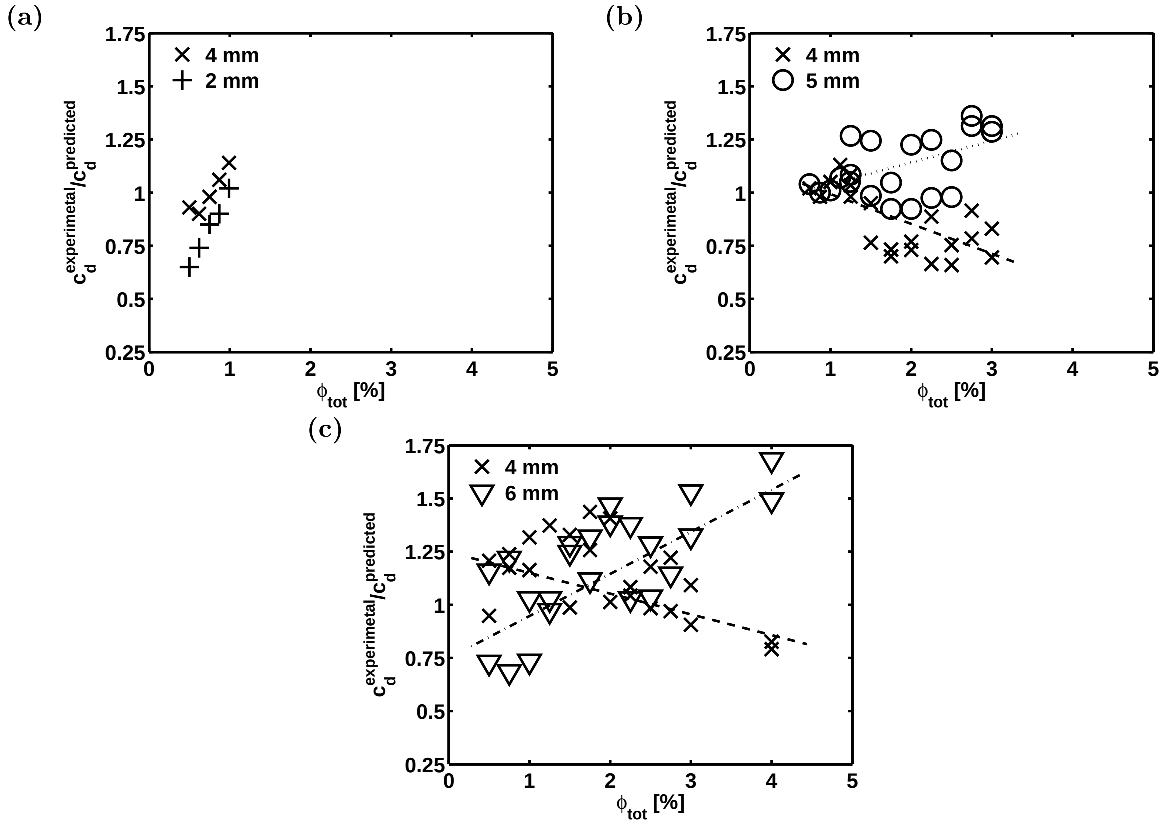

Figure 5.18: Experimental and predicted drag coefficients ratios against concentrations: (a) bidisperse suspension 2 & 4 mm, (b) bidisperse suspension 4 & 5 mm with trend lines and (c) bidisperse suspension 4 & 6 mm with trend lines.

large scattering of the data. In order to investigate possible causes of this scattering, locally averaged slip velocities for all the experiments were obtained. In figure 5.19, three representative experiments (exp. 6, exp. 21 and exp. 52) of each bidisperse suspension system (2 and 4, 4 and 5, and 4 and 6 mm particles) are shown; since similar results were obtained in the other experiments, these are not presented here. Although certain variation is observed, this cannot be conclusively attributed to the preferential spatial distribution of the species.

Finally, figure 5.18(c) shows the comparison of the 4 and 6 mm mixtures. In this case, 4 mm particles show higher drag than predicted in low concentration suspensions. This higher drag is maintained until the total concentration approaches 2% values. There, good agreement with predicted drag is observed. For higher concentrations than 2% lower drag of 4 mm particles is measured, which confirms the trend seen in figure 5.18(b). However, the steeper gradients of the trend lines in comparison to the 4 and 5 mm suspensions indicate higher momentum transfer. For concentrations lower than 2% a larger scatter of the measured drag of the 6 mm particles is observed. This effect could not be explained based on the present data and therefore requires further investigations. For higher concentrations than 2% lower experimental drag, as seen in the 4 and 5 mm

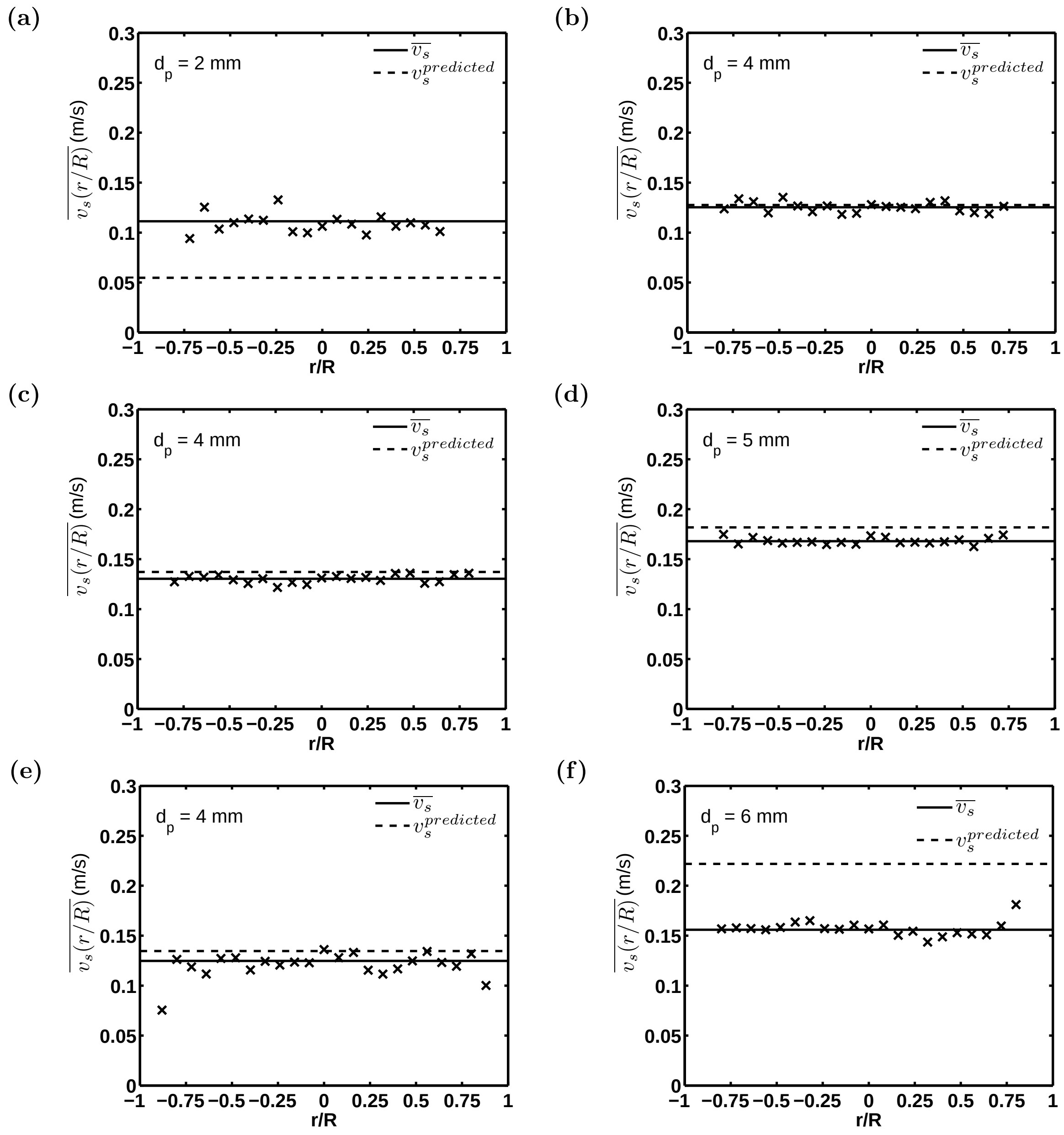

Figure 5.19: Comparison of the locally averaged slip velocities with the total averaged and the predicted slip velocities. ×, locally averaged slip velocities: (a) exp. 2, $\phi_2 = 0.37\%$, (b) exp. 2, $\phi_4 = 0.62\%$, (c) exp. 21, $\phi_4 = 0.62\%$, (d) exp. 21, $\phi_5 = 0.62\%$, (e) exp. 52, $\phi_4 = 1.00\%$ and (f) exp. 52, $\phi_6 = 1.00\%$.

suspensions, is measured. While the behaviour for higher concentrations than 2% was foreseen, the same before 2% concentrations is somehow puzzling. Characteristics similar to the 4 and 5 mm suspensions, where dilute total concentrations show good agreement with predicted values, would be expected. Furthermore, the steeper gradients of the trend lines in comparison to the ones of the 4 and 5 mm suspensions indicate higher momentum transfer intensity.

5.6 Closure

In this chapter, mono- and bidisperse suspensions of rigid spherical particles lagging a laminar vertical axisymmetric sudden expansion flow have been examined by optical methods and analyzed with a two-fluid computational method. The experimental conditions covered situations in which reference particles (d_{p4} = 4 mm) were mixed with smaller (d_{p2} = 2 mm) and bigger (d_{p5} = 5 mm and d_{p6} = 6 mm) particles at several dilute volume concentrations between 0.12 and 4.00%.

The fluid velocities were acquired with a two-dimensional/two-components (2D2C) PIV setup and the particle velocities and positions were acquired with a 2D2C PTV setup. These supplied velocities on an axial slice at the center of the test pipe centered at 1.6 meters downstream of the sudden expansion. Diagrams of the averaged fluid and particle velocities, as well as, particle position histograms demonstrate that the pipe axis constitutes an axis of symmetry for the investigated regimes. This allows the assumption of symmetry in the azimuthal direction and therefore lack of three-dimensional effects. Slight asymmetry is observed in the highest flow rate experiments. This is attributed to curvature of the pipe upstream of the sudden expansion. Therefore, for higher flow rates it is recommended to extend the length of the straight section before the suspension flows through the sudden expansion.

The results for monodisperse suspensions showed good agreement with previous experimental and analytical works. They confirm the existence of a clear surrounding annulus of liquid with the broadness modified by bulk concentration and flow rate. This annulus broadness is quantified through particle distribution histograms. With regard to bidisperse suspensions, complex phenomena such as preferential concentration was observed at low concentrations, while higher particle volume fractions produced more homogeneous particle distributions.

The evaluation of momentum transfer between species through comparison of the measured and predicted drag coefficients revealed higher measured drag coefficients for 4 mm particles and lower ones for the 2 mm particles. This is explained by interaction between both species. In the case of 4 and 5 mm bidisperse suspensions, where more measurements were available, momentum transfer between species was clearly identified. The same was more intense as concentration increased. Moreover, in 4 and 6 mm bidisperse suspensions momentum transfer was also observed. However, somehow unexpected behaviour could be seen for total concentrations below 2%. The same should be further analysed. In any case, the momentum transfer between species was evident and its intensity could be correlated to the particle diameter ratio.

6 Numerical results

> *"Remember that all models are wrong; the practical question is how wrong do they have to be to not be useful."*
>
> \- George E. P. Box

We now explain the simulations performed using the Two-Fluid method and the combined CFD-DEM approach introduced in chapter 4. First of all, simulations output of the Two-Fluid Method is put in comparison to the experimental data for validation. This implementation is then used to explain the concentration peaks observed in the physical experiments. Secondly, the CFD-DEM approach is also compared with experiments for validation. Finally, a sensitivity analysis is performed using the CFD-DEM method to evaluate the effects of eccentricity on the transport of solid particles through annular conducts.

6.1 Results of monodisperse flow [1]

The flow of semi-dilute bidisperse suspensions in axisymmetric sudden expansions present complex interactions of the dispersed species and the continuous medium. Optical measurements are able, to a certain point, to quantify macroscopic parameters. However, these are constrained to the regions where the measurements are done and supply in this way local representations of reality. Although these can be used for comparison, a global representation of the system is necessary to explain non expected behaviors. Transient CFD offers the possibility to represent the complete system along the time. This allows the analysis of the causes behind a particular observation. In other words, the experiments allow us to take an instantaneous picture of the system at a certain position, while transient CFD simulations allow us to reproduce the series of events taking us to that picture. Since CFD is constrained by the physics embedded in the numerical models, the comparison with the experiments allows to confirm if the physics and assumptions done are sufficient to represent reality accurately.

In this section, the simulations performed using the two-fluid model to evaluate particle distributions of monodisperse suspensions in an axisymmetric sudden expansion are explained. The basis implementation used is the one developed by Rusche [87] and also

---

[1] Preliminary results were published in a paper for the International Journal of Multiphase Flow [77].

available in the open-source code OpenFOAM version 2.1.1. Particles are considered to be smooth and perfectly spherical. In addition, no collisions are modeled.

6.1.1 Setup

Simulations were set up in a two-dimensional axi-symmetric mesh because of the axial symmetry of the vertical sudden expansion flow. Discretization of the axisymmetric computational domain resulted in 9,000 cells. The geometry used was identical to the one used in the experimental measurements, with the exception of the exit sudden-contraction found in the experimental setup. In figure 6.1 a diagram of the computational domain and the structure of the computational grid are shown.

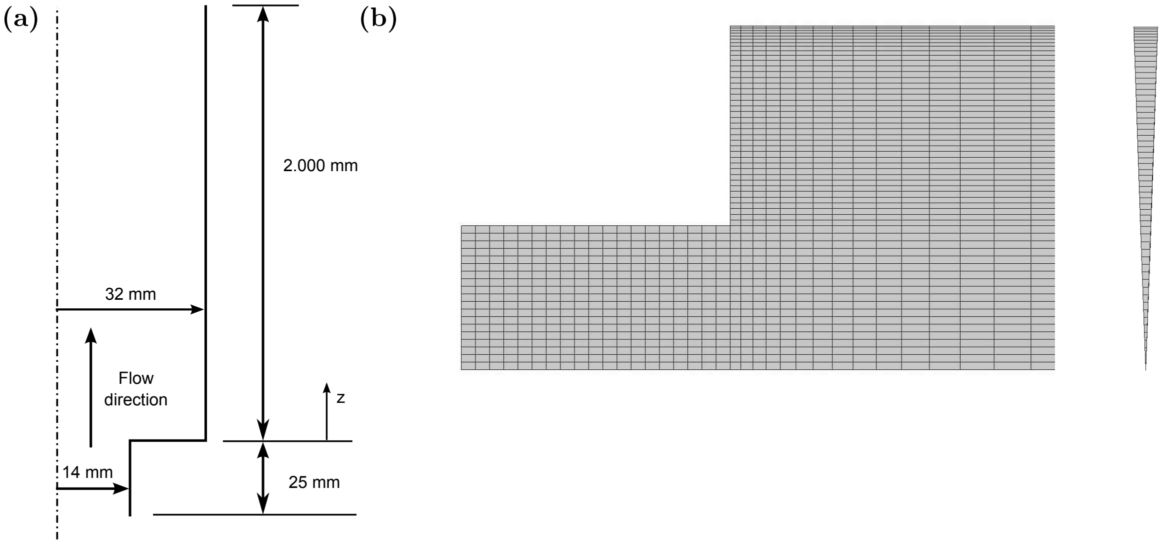

Figure 6.1: Geometry of the two-fluid simulations: (a) Computational domain and (b) grid structure.

At the inlet, velocities and concentrations of both phases are set to a constant and homogeneous value. For pressure, a Neumann boundary condition with zero gradient is used. At the outlet, a static pressure set to null is used as reference. Correspondingly, velocities and phase fraction use a Neumann boundary condition with zero gradient. Finally, the liquid and particle velocities are set to null to impose the no-slip boundary condition at the wall.

The solver used within the OpenFOAM library was the twoPhaseEulerFoam. This one is based on the two-fluid model and it has been extended with the lift model by Saffman-Mei explained in subsection 4.2.1.2. The algorithm used to solve the pressure-velocity coupling in the momentum equations is the PIMPLE algorithm, which is a combination of the PISO and SIMPLE algorithms.

The numerical schemes used to discretize the governing equations are the Euler scheme (first order, bounded, implicit) for the time derivative, the Gauss scheme for both gradients and divergence terms, whereas linear interpolation is chosen for gradients and limited linear differencing for divergence terms involving velocity and volume fraction fields. Furthermore, the Laplacian terms use the Gauss scheme with linear corrected interpolation (unbounded, second order, conservative).

6.1.2 Monodisperse experiments

Comparison with monodisperse suspension experiments is performed to evaluate the reliability of the numerical predictions. In figures 6.2 and 6.3 comparisons of the velocity profiles and the concentration distributions 1.6 meters downstream of the sudden expansion are shown for experiment #7 and #10, respectively. The experimental and numerically obtained velocity profiles are normalized with the maximum velocity of a Hagen-Poiseuille flow with equivalent flow rate. With reference to the particle distributions, these are compared with the predicted local particle concentrations. The results are compared semi-quantitatively in Fig. 6.2 (b). Strictly speaking, only the radial location of the dispersed phase is quantitatively compared. The concentration scaling of the right y-axis is selected to match that one of the particle position probabilities. In this way, a prediction of the local concentration in the experiments is obtained. The results show fairly good agreement between experimental profiles and numerical ones for experiment #7. For experiment #10, while particle distributions are also in good agreement, experimental and numerical results of the liquid velocity show a considerable mismatch. Differences are attributed to the concentration measurement method used in the experiments. Due to its integral character, it was not possible to quantify its value at the entrance of the test pipe, as it would be necessary for a perfect matching of the boundary conditions. The slower velocities of the fluid in the simulation denote larger momentum transfer. Therefore, experiment 10 was probably performed at slightly lower concentration than the used in the simulations ($\phi_4 = 0.50\%$).

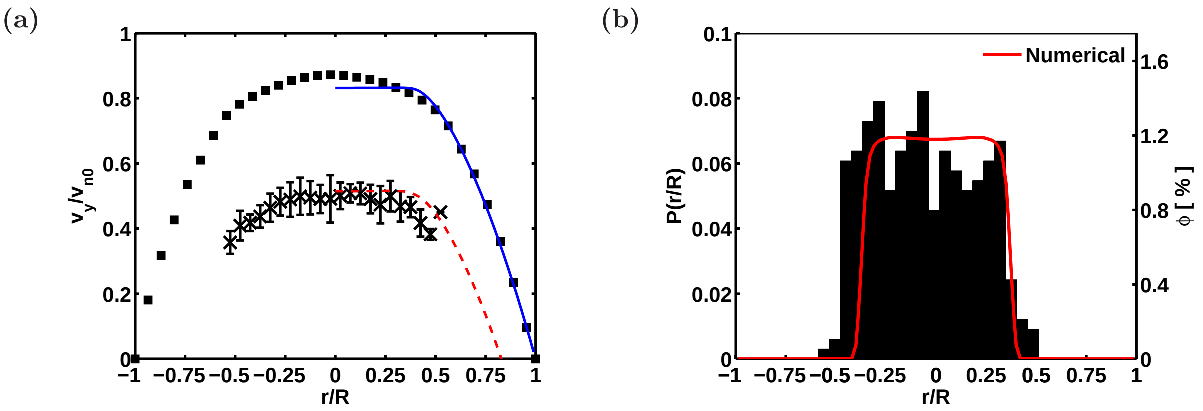

Figure 6.2: Exp. #7, $\phi_4 = 0.12\%$: (a) fluid and particle velocities at 1.6 meters from the entrance and (b) particle distributions and concentrations at the same position.

In figure 6.4 (a and b) velocities and concentrations along the axis are shown for simulations performed with a constant *Re* number equal to 285 and three different concentra-

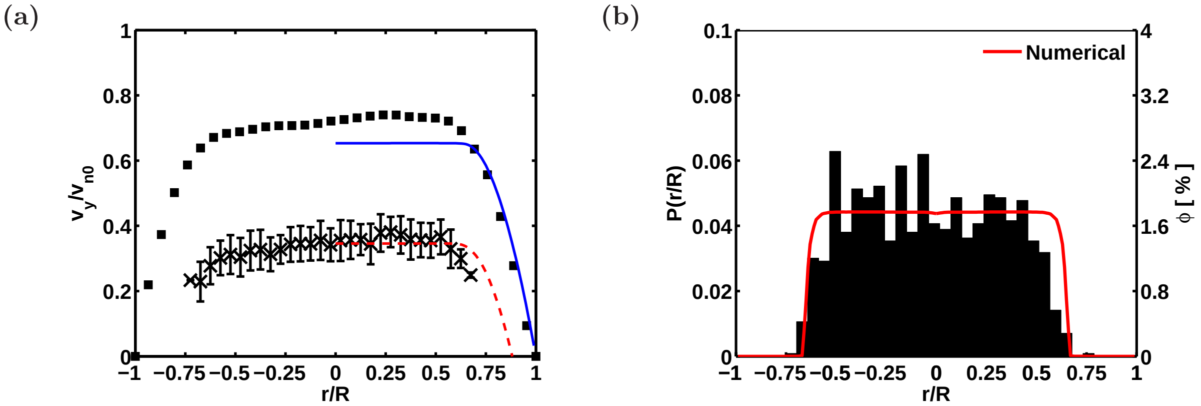

Figure 6.3: Exp. #10, $\phi_4 = 0.50\%$: (a) fluid and particle velocities at 1.6 meters from the entrance and (b) particle distributions and concentrations at the same position.

tions. As can be seen, the computed velocities far downstream of the sudden expansion, namely after the flow has fully developed, are identical. However, the entrance length decreases significantly with increasing particle concentration.

The concentrations along the axis show a sudden increase around 0.5 meters downstream from the sudden expansion. This accumulation of particles in front of the entrance is caused by interplay of lift forces, which bring particles towards the axis, and sudden reduction of velocity. After the accumulation, the concentrations also reach a stationary value. For 0.5% feed concentrations these are reached gradually. In the case of the two higher concentrations (1.10 and 2.50%), these decrease abruptly and oscillate around the stationary concentration until the same is reached. Furthermore, it is interesting to put the concentrations along the axis predicted for feed concentrations equal to 0.5% with the concentration distributions form figure 6.3 (b) in relation. It may be observed how the stationary concentration is constant along the central core positions. These positions correspond to positions where the fluid velocity fluctuates, due to the presence of the particles, resulting in a flattened fluid velocity profile after averaging. At positions closer to the wall the shearing intensity is sufficient to keep those regions clean of particles. This reduction of the diameter, where particles are found, together with the hold-up caused by the slip velocity contributes to higher stationary concentrations than those assigned at the input boundary condition.

The particle accumulation in front of the sudden expansion is thought to be the cause of the concentration peaks observed in the measurements of bidisperse suspensions (see figures 5.12 (d) and 5.14 (a) for clear examples). The observation of these peaks can be explained by the accumulation of the heavier species at the core. The flow of the suspension through the sudden expansion creates a particle accumulation in front of the expansion, which creates an obstacle for the arriving suspension. Within this obstacle, the intense momentum transfer between phases causes velocities to significantly decrease. In addition, the arriving suspension encounters less resistance through the space left between the obstacle and the pipe wall producing velocity profiles resembling the wall channelling phenomena observed in porous media flow (see figure 5.17 for various examples). This

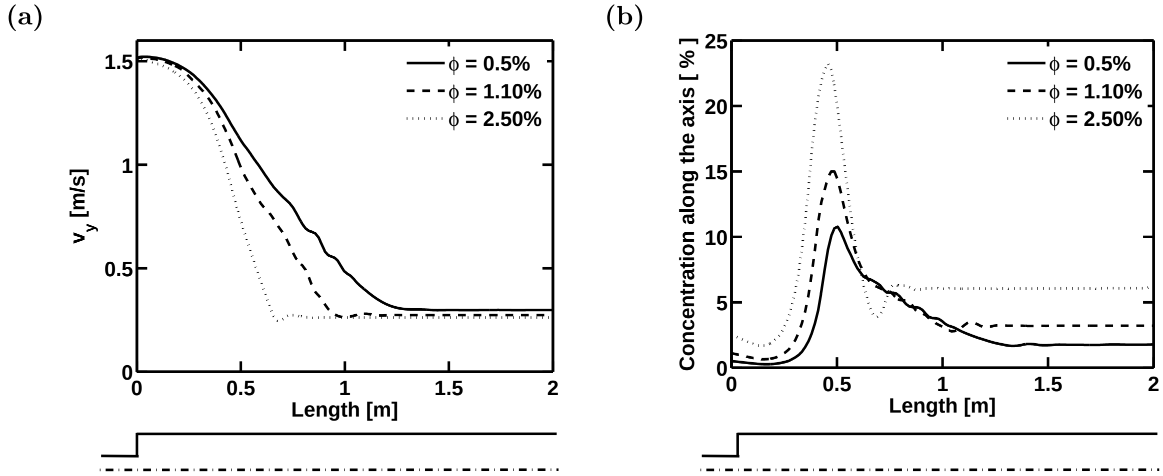

Figure 6.4: Numerical results of the concentration and fluid velocities along the axis for $d_p = 4mm$ particles and $Re_c = 285$: (a) fluid velocities along the axis and (b) particle concentrations along the axis

results in internal velocity gradients of reversed sign within the flow causing lift forces on the particles acting towards the wall instead of acting towards the axis, as it is common for particles lagging an upward vertical flow. The counteraction of forces acting towards the axis at positions close to the wall and forces acting towards the wall at intermediate radial positions produces a circular equilibrium position, where the probability to find particles increases. Similar equilibrium positions between pipe wall and axis were first described by Segré and Silberberg [35] and also investigated by Vasseur and Cox [121], between others. However, these studies considered neutrally buoyant particles. The mechanisms are different in the sense that neutrally buoyant particles present an equilibrium position caused by the varying intensity of the shear rate along the radial positions, which is responsible for the intensity and, more importantly, for the direction of the force. This effect is therefore stationary as long as the flow is fully developed. On the other hand, for particles lagging the flow, as investigated here, the force direction is not dependent on shear rate intensity but only on shear rate direction. For this reason, only shear rates of different directions can be responsible for forces of opposite direction and, eventually, equilibrium positions. Since the accumulation of particles is localized after the sudden expansion, the internal modification of shear rate direction is a local phenomena. The length of this modification is determined by the interchange of momentum between phases and species involved. This is a clear example of a three-way coupling phenomenon, where the particles are affected by the fluid, the fluid is affected by the particles and the disturbances in the fluid affect in turn the motion of the particles

6.2 CFD-DEM comparison with experiments

In this section, the experimental results of chapter 5 are compared with results obtained with the CFD-DEM approach. Firstly, the set-up of the experiment is shortly reminded. Following, the numerical grid is shown and a grid-independence analysis is performed for simulations only with fluid. Then, the boundary conditions used in the simulations and the numerical implementation are explained. Finally, the mono- and polydisperse systems are compared with the experimental results.

6.2.1 Setup

The validation of the numerical models is implemented by comparison with several of the experiments performed in the experimental phase of this work. The variables compared are the velocities of the fluid and the particles at the specified distance as well as the particle distribution. The results offer velocities and particle positions at 1.6 meters from the sudden expansion. The list of presented experiments may be reviewed in table 5.1 in section 5.3. From this list a selection of limiting cases has been extracted. This list is composed by experiments #2, #6, #7, #10, #11, #15, #20,# 37, #46 and #62. The geometry is the one already characterized in section 6.1.1 and conveniently reproduced in figure 6.1(a). The diameters of the two pipe sections are 28 and 64 mm respectively. The complete length of the test section is 2,025 mm.

For the CFD side, the geometry is dicretized with a three-dimensional structured curvilinear grid composed of hexahedrons. The grid is shown in figure 6.5(a). This is formed with one small O-grid covering the diameter of the entrance along the complete length of the test pipe (2,025 mm). This one is filled with a quadrilateral block and wrapped with a larger O-grid covering the diameter of the test pipe and starting 25 mm after the inlet for a total lenght of 2,000 mm as can be appreciated in figure 6.5(b). The number of elements is selected on the basis of a grid analysis performed only with the liquid-phase, where the numerical solutions are compared with the Hagen-Poiseuille solution. This results in O-gids discretized with 40 elements in the circumferential direction and 10 elements in the radial direction. Likewise, the quadrilateral inner block is discretized with 10 elements on each side. This adds to a total of 182,500 elements. Solutions obtained with this grid are compared with the analytic solution in figure 6.6.

For the DEM side, a computational domain formed by a cylinder with 64 mm diameter and 2,025 mm length is used. This domain is delimited with the surfaces of the CFD geometry to maintain the particles only within the intersection of the CFD and DEM domains. Contrary to the CFD case, this computational domain does not need discretization. The Lagrangian framework allows any position within the domain with the precision according to the floating point data type selected.

The physical modelling is based on the numerical model introduced in chapter 4. The physical properties of the liquid and of the particles for each simulated system are the ones listed in table 5.1. From this list, the density and viscosity of the liquid can be correlated as a function of the temperature. The density at the experiment temperature

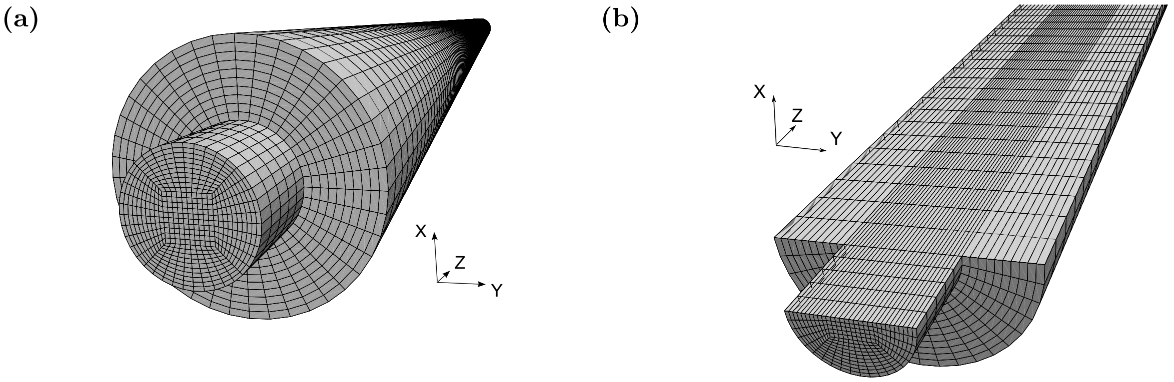

Figure 6.5: Discretized geometry: (a) complete perspective view and (b) halved perspective view.

is obtained as follows:

$$\rho_{exp} = \frac{\rho_0}{(1 + \beta_{exp}(T_{exp} - T_0))} \ \mathrm{kg/m^3}, \tag{6.1}$$

where ρ_0 is the reference density at the reference temperature T_0 and β_{exp} is the volumetric temperature expansion coefficient. For medicinal white oil, ρ_0 can be taken as 865 kg/m^3 at 15 °C and β_{exp} as 7.64×10^{-4} m^3/(m^{3}K). The viscosity is obtained from the following correlation valid between 20 and 40 °C:

$$\eta_{exp} = -2.15 \ T_{exp} + 114.30 \ \mathrm{mPa \cdot s}. \tag{6.2}$$

The particle properties used in the simulation are listed in table 6.1, where also the complete parameters of the simulations may be found. All of them but the Young's Modulus are material properties characteristic of glass. Setting a Young's Moduls similar to the one of glass (E =60 GPa) results in an abrupt increase of the particles kinetic energy causing the disappearance of some of the particles. To avoid such a problem and considering the low probability of contacts between particles and walls at a maximum concentration of 4%, a lower Young's Modulus is set. Interestingly, the most convenient Young's Modulus closely matches that of clayey soil (E= 28 MPa) and is not far from those of gravelly soils (E = 40-70 MPa). Both are materials similar to those produced during drilling operations. The problem can also be solved by decreasing the particle time step. This avoids large overlapping of the particles and reduces the kinetic energy added through the time integration. However, this translates in extremely time intensive computations.

Model *type A* and volume fraction model `divided` are selected for all the experiments. Furthermore, *DiFelice*'s model is selected for the drag force, *Mei*'s model is selected for the lift force and buoyancy is considered by activating `Archimedes` force model.

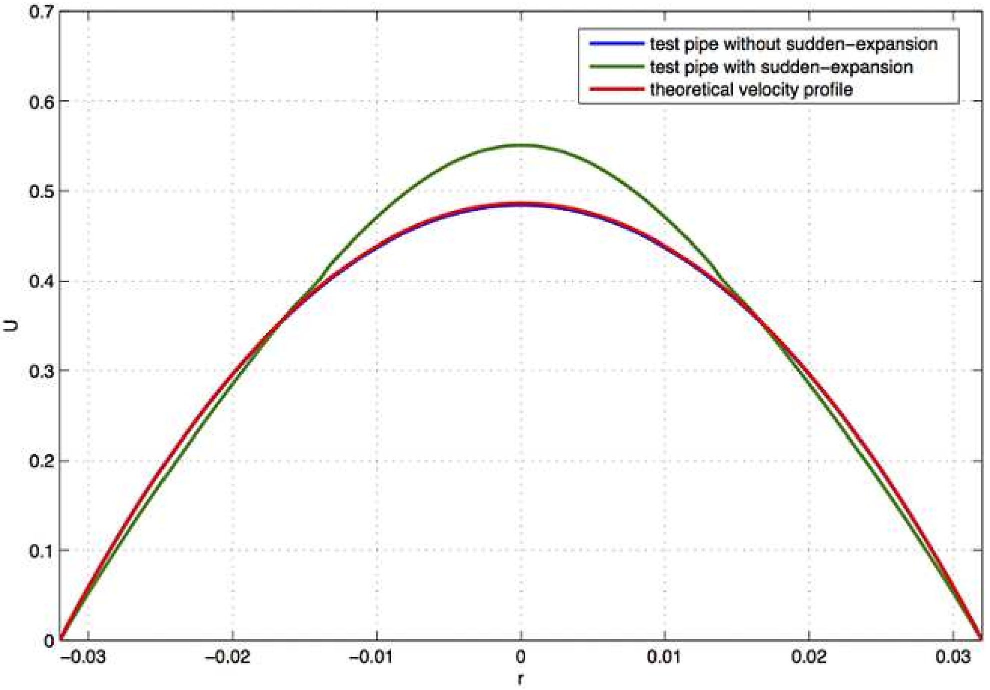

Figure 6.6: Comparison of the Hagen-Poiseuille solution and numerical results obtained with the discretized geometry.

For the fluid, the boundary conditions are set on three areas of the computational domain denominated `inlet`, `outlet` and `fixedwall` as shown in figure 6.7. At `inlet`, velocity of the liquid phase is set to a constant and homogeneous value u_l'. Firstly, the average velocity of the liquid in the larger section of the test pipe is calculated through the Reynolds number Re and the liquid properties of the specific experiment listed in table 5.1

$$u_l = \frac{Re\ \eta}{\rho_l\ D}, \tag{6.3}$$

where D is the diameter of the test pipe equal to 64 mm. Then, the velocity at `inlet` is obtained assuming mass conservation in incompressible flow

$$u_l' = \left(\frac{D}{D'}\right) u_l, \tag{6.4}$$

where D' is the diameter in the entrance section equal to 28 mm. For pressure, a Neumann boundary condition with zero gradient is used. At `outlet`, a static pressure set to null is used as reference. Correspondingly, fluid velocity uses a Neumann boundary condition with zero gradient. Finally, the liquid is set to null to impose the no-slip boundary condition at `fixedwall`. The particles are inserted in the computational domain with a vertical velocity calculated as the inlet velocity of the liquid u_l minus the terminal velocity

Variables	Values
Pipe geometry:	
Inlet diameter (D')	28 mm
Diameter (D)	64 mm
Length (L)	2,000 mm
Number of cells	182,500
Particle properties:	
Particle diameters (d_{pi})	2 - 6 mm
Particle densities (ρ_i)	d_{p2} = 2,500 kg m^{-3}, d_{p4}, d_{p5} and d_{p6} = 2230 kg m^{-3}
Young's Modulus (E)	2.5×10^7 Pa
Poisson ratio (ν)	0.2
Coefficient of restitution (e)	0.77
Friction coefficient (μ)	0.2
Volume fractions (ϕ_i)	0.12 - 4 %
Particles velocity at inlet (u'_p)	u'_l - u_{set}
Fluid properties:	
Density (ρ_l)	$\rho_{exp} = 865/(1 + 7.64 \times 10^{-4}(T_{exp} - 15))$ kg m^{-3}
Viscosity (η_l)	$\eta_{exp} = -2.15\ T_{exp} + 114.30$ mPa·s
Fluid velocity at inlet (u'_l)	Obtained from equation 6.4 and table 5.1)

Table 6.1: Parameters used in the CFD-DEM comparison simulations.

of the particles u_t. The insertion is performed within a 12 mm high and 10 mm radius cylindrical region with the bottom side coplanar to `inlet`. The volume fraction of every simulated experiment is converted in particles per second n_p according to the volume fraction definition

$$\phi = \frac{\frac{\pi}{6}\ d_p^3\ n_p}{\frac{\pi}{4}\ u'_l\ D'^2}. \tag{6.5}$$

Whereas, particles are inserted at 4 Hz frequency to obtain a homogeneous particle introduction. Particles are allowed to exit the computational domain at `outlet` and collision modelling is set at `fixedwall`.

The time-step for the CFD side is set to δt_{flow}=0.001 seconds, which satisfies the Courant-Friedrichs-Lewy (CFL) condition in all simulated cases. On the other side, the DEM time-step is selected on the basis of the Rayleigh time introduced in section 4.2.2. Considering the particle properties listed in table 3.1, the time-step for the DEM side is set to δt_{soft} =1×10^{-5} seconds. The coupling of both solvers defined by $\delta t_{coupling}$ is set to the same time as the CFD time-step. The initial condition of the simulation for the liquid-phase is no velocity in any direction over the complete domain. After 2 seconds of simulated time, the liquid flow acquires the so called single-phase steady-state. Then, the particle insertion begins and the simulations are left running for as long as particles start to be continuously transported out of the computational domain. From this moment, at least 20 seconds of simulation are saved for analysis.

The solver used within the CFDEM library is the cfdemSolverPiso. The same is based on the pisoFoam solver by openFOAM coupled with the LIGGGHTS simulation code.

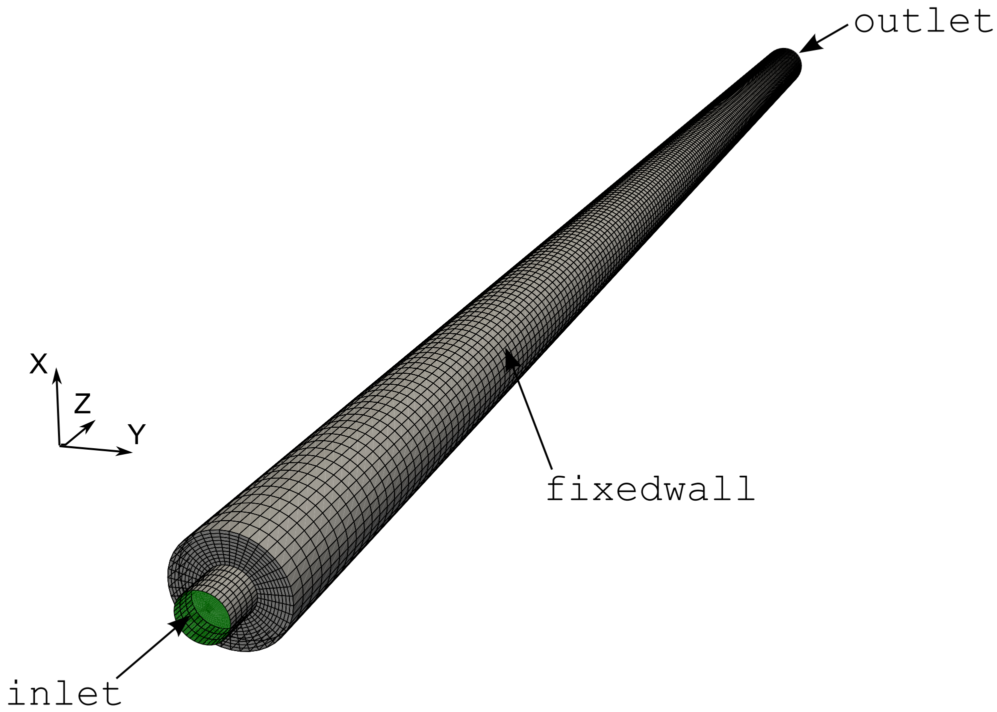

Figure 6.7: Definition of the boundaries in the computational domain.

The algorithm used to solve the pressure-velocity coupling in the momentum equations is the PISO algorithm. The numerical schemes used to discretize the governing equations are the Euler scheme (first order, bounded, implicit) for the time derivative, the Gauss scheme for both gradients and divergence terms, whereas linear interpolation is chosen for gradients and limited linear differencing for divergence terms involving velocity and volume fraction fields. Furthermore, the Laplacian terms use the Gauss scheme with linear corrected interpolation (unbounded, second order, conservative).

6.2.2 Data processing

The results obtained from the experimental set-up are derived from measurements performed on a plane coplanar with the pipe axis. On the other hand, the numerical results are obtained from the complete cross section at 1.6 meters of the sudden expansion. This difference in the type of data acquired needs to be conveniently treated in order to obtain histograms of the particle positions, which can be directly compared. The experimental results are presented in diagrams, where the x-axis depicts the non-dimensionalized radial position and the zero position is the axis of the pipe. In this way, the positive radial positions are on the right of the pipe axis and the negative ones on the left. In the case of the simulations, a circular cross sectional slice is used to acquire position and velocity of the particles. The particles distribute, then, on two-dimensions instead of on one-dimension as was the case for the experiments. The first action is to separate the particles data in two semi-circles. In figure 6.8, the semi-circle on the left corresponds to negative radial positions and the one on the right corresponds to the positive radial positions.

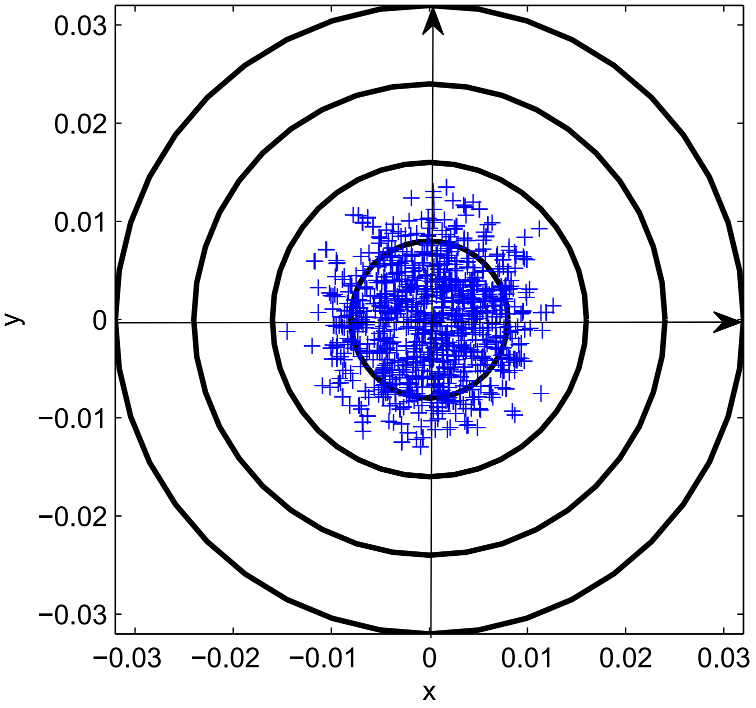

Figure 6.8: Cross section at 1.625 m with particle positions. +, particle positions. —-, circles with varying radius.

The second action corrects the effect of circumferences capturing a higher amount of particles at larger radii. This follows the reasoning of Matas et al. [122] to obtain a radial probability function $P(r)$. It starts by building a histogram from all the measured radial positions on the cross-section. The histogram, "when normalized, yields the probability density function (p.d.f.) $P_r(r)$ associated with the probability of a particle being at radius r." However, the radial probability function $P(r, \Theta)$ is associated with the probability of being at a radius r and a given angular position Θ. The numerically obtained P_r is related to P by

$$P_r(r) = \frac{1}{\pi} \int_0^{2\pi} P(r, \Theta) r d\Theta. \tag{6.6}$$

Assuming that P depends only upon r, this yields

$$P(r) = \frac{P_r(r)}{2r}. \tag{6.7}$$

Finally, considering the previous division of the cross-section in two semi-circles, $P(r)$ is obtained by

$$P(r) = \frac{P_r(r)}{r}. \tag{6.8}$$

The first example of such data processing is shown in figure 6.9 (d).

6.2.3 Monodisperse experiments

The simulations in this section are performed with monodisperse suspensions. In the experiments, the particle size selected was 4 mm. Moreover, two types of analyses were conducted. One focused on volume fraction variation with constant flow-rate and the other one focused on flow-rate variation with constant volume fraction. From these experiments, which go from #7 to #15 in table 5.1, experiment #7 and #10 are simulated and compared with the experimental results to examine the response of the numerical model at increasing volume fractions. On the other hand, experiments #11 and #15 serve to explore the implications of varying shear-rates and implicitly lift forces.

6.2.3.1 Concentration variation

Figure 6.9 shows the comparison for experiment #7. The diagrams follow the representation of the data used for the experiments and already explained in section 5.4.1. Figures 6.9 (a) and (b) correspond to the experimental results, while figures 6.9 (c) and (d) are the numerical results. Comparison of the liquid velocity profiles reveals very similar maximum velocities, whereas the shape of the numerical results is more flattened at centred positions. The similarity in the maximum velocities indicates proper replication of the momentum transfer between phases. The particle velocities also display similar behaviour, although a more flattened velocity profile is observed in the physical experiments. Velocity fluctuation are lower in the simulations. In table 6.2 a comparison of the fluctuations in the experiments and the simulations quantified through the standard deviation of the particle velocities is shown. Looking at the particle distributions, positions closer to the axis are regarded for the numerical simulations. These result in higher probabilities than the ones measured in the experiments. This more concentrated positions are an explanation for the flatter liquid velocity profile. The shear rates are in the same range, but seem to apply a stronger lift force in the case of the simulations.

The comparison of experiment #10 with a light increase in concentration up to ϕ_4=0.50% is shown in figure 6.10. The effect of the volume fraction increase is clearly appreciated in the flattening of the liquid velocity profiles. The numerical simulation is able to replicate the liquid and particle velocity profiles of the experiments accurately. By contrast, the particle velocity fluctuations are quite lower in the simulations. This is again quantified in table 6.2. Figures 6.10 (b) and (d) show the particle distributions. In this case, the matching of experiments and simulations is almost perfect. A sign for the appropriateness of the lift force model in terms of the particles locations.

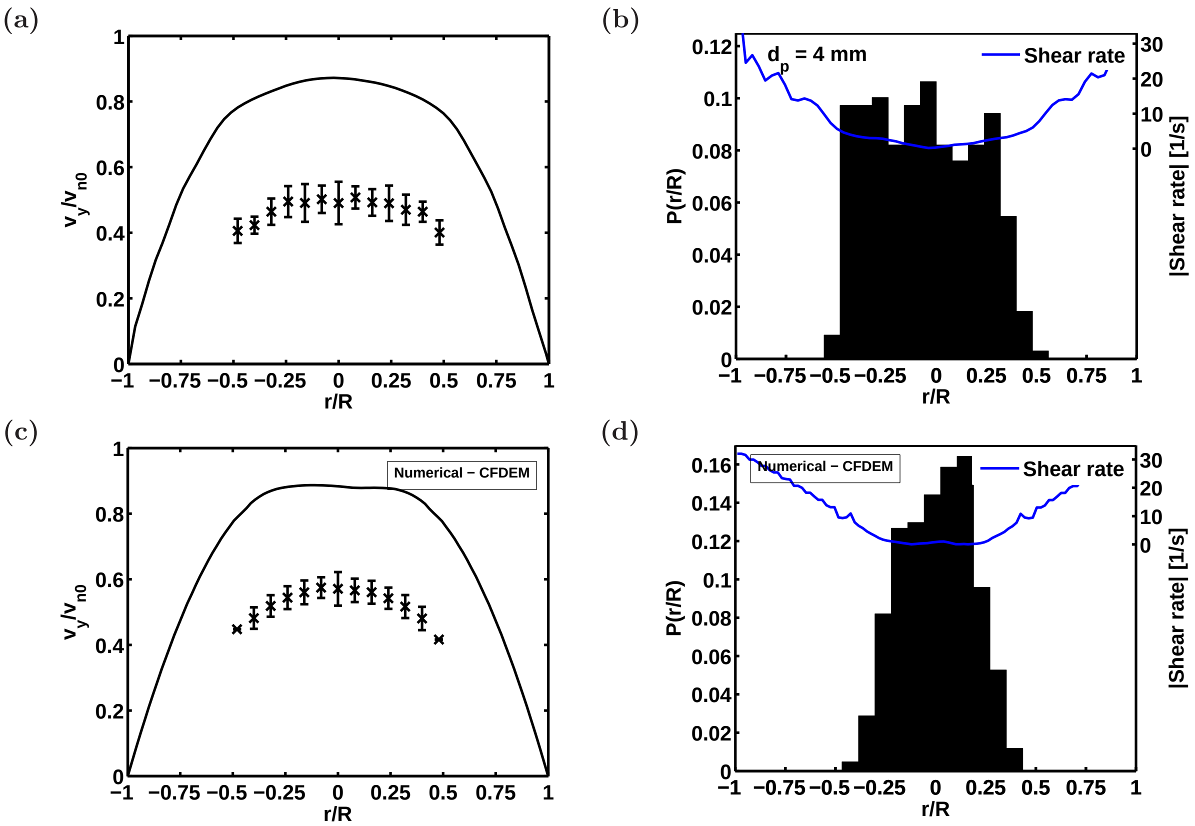

Figure 6.9: Comparison of the vertical velocities of the 4 mm particles and normalized histograms of the particle positions for experiment #7, $\phi_4 = 0.12\%$. ×, vertical velocities of the 4 mm particles, —, locally averaged fluid velocity profile: (a and b) experimental results and (c and d) numerical results.

6.2.3.2 Constant concentration and varying flow rate

In figure 6.11 the comparison for experiment #11 is shown. In this experiment, it is possible to observe a system corresponding to a fluidized state. In this case, the numerical results do not accurately match the experimental results. In figure 6.11 (c) the liquid velocity is over-predicted. In addition, the particle velocities are not stationary as in the case of the experiments and are entrained with low velocities. Moreover, the particle fluctuations are much higher in the simulations than in the experimental case. With respect to the particle distributions positions are matched. This is due to the strong shear rates close to the walls pushing the particles inwards. However, the shape of the particle histograms are significantly different. This is clearly observed at the extremes, where the peaks measured in the experiments cannot be detected in the simulations.

By increasing the flow rate and keeping the concentration fixed at $\phi_4 = 0.62\%$, experiment #15 is obtained. In this case, the comparison, shown in figure 6.12, offers again good matching. Velocity profiles of the liquid and the particles are properly replicated. The slight asymmetry of the liquid profiles, already commented in section 5.6, is not observed in the simulations, because of the homogeneous inlet liquid velocity set in the simulations.

Exp.	ϕ_2[%]	ϕ_4[%]	ϕ_5[%]	ϕ_6[%]	$\overline{\sigma_{p2}}$ [mm/s] (exp./sim.)	$\overline{\sigma_{p4}}$[mm/s] (exp./sim.)	$\overline{\sigma_{p5}}$[mm/s] (exp./sim.)	$\overline{\sigma_{p6}}$[mm/s] (exp./sim.)
7	-	0.12	-	-	-	15 / 14	-	-
10	-	0.50	-	-	-	19 / 12	-	-
11	-	0.62	-	-	-	21 / 42	-	-
15	-	0.62	-	-	-	22 / 15	-	-
2	0.25	0.25	-	-	21 / 8	25 / 7	-	-
6	0.37	0.62	-	-	40 / 17	26 / 17	-	-
20	-	0.62	0.50	-	-	35 / 41	28 / 32	-
37	-	1.50	1.50	-	-	43 / 43	45 / 35	-
46	-	1.00	-	0.25	-	42 / 57	-	29 / 44
62	-	2.00	-	2.00	-	77 / 62	-	49 / 50

Table 6.2: Comparison of the standard deviation of the particle velocities between experiments and simulations

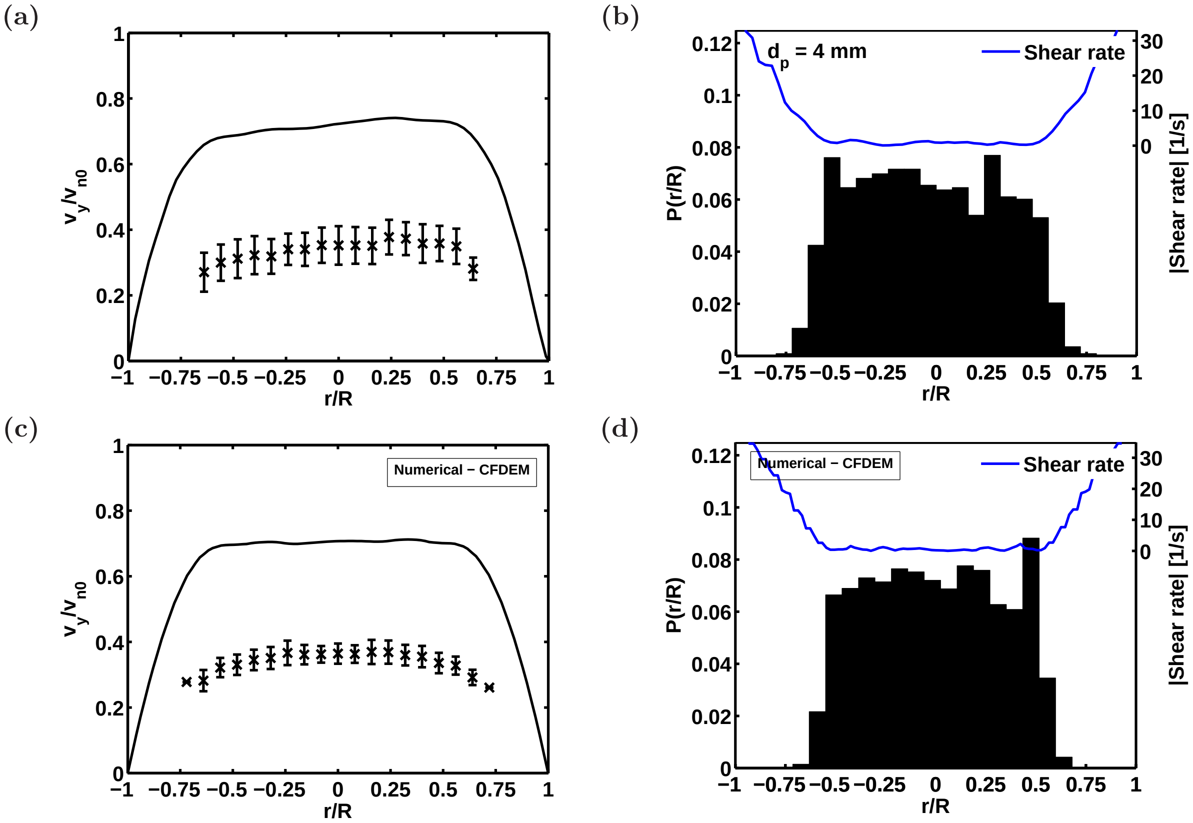

Figure 6.10: Comparison of the vertical velocities of the 4 mm particles and normalized histograms of the particle positions for experiment #10, $\phi_4 = 0.50\%$. ×, vertical velocities of the 4 mm particles, —, locally averaged fluid velocity profile: (a and b) experimental results and (c and d) numerical results.

Again here, lower velocity fluctuations are observed in the predictions. This could be a sign of lower particle interactions than the occurring in the experimental systems. Particle distributions are also here satisfactory with the surrounding annulus clear of particles

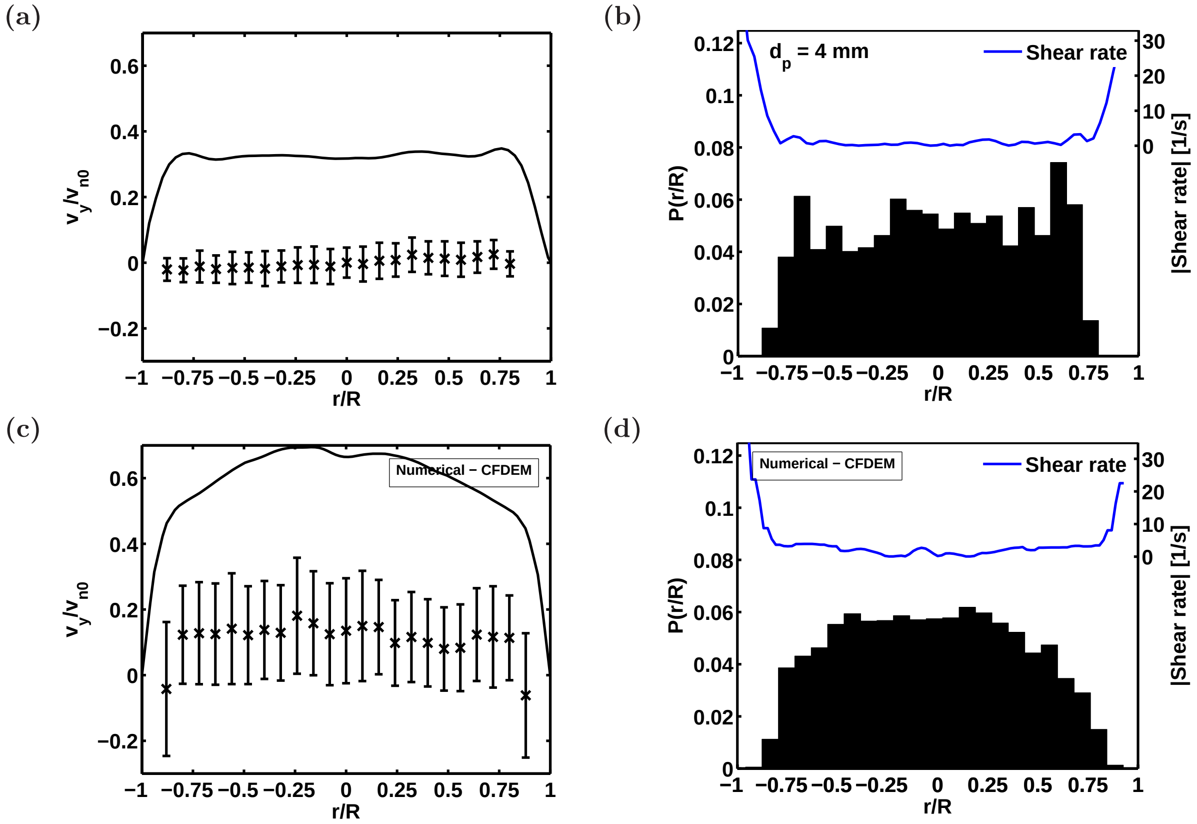

Figure 6.11: Comparison of the vertical velocities of the 4 mm particles and normalized histograms of the particle positions for experiment #11, $\phi_4 = 0.62\%$. ×, vertical velocities of the 4 mm particles, —, locally averaged fluid velocity profile: (a and b) experimental results and (c and d) numerical results.

sharply predicted. Being the only appreciable difference, the tendency of the particles to concentrate at the extreme of the histograms in the experiments.

6.2.4 Polydisperse experiments

The simulations in this section are performed with bidisperse suspensions. In the experiments, the reference particle size selected is again 4 mm, while the sizes added to obtain the bidisperse systems are 2 , 5 and 6 mm. A selection of the cases representing experiments with lowest and highest volume fractions in each series are selected from the list of experiments presented in table 5.1 for comparison. For the bidisperse suspensions of 2 and 4 mm particles, experiments #2 and #6 are chosen. Secondly, experiments #20 and #37 are selected to perform the comparison for bidisperse suspensions of 4 and 5 mm particles. Finally, the 4 and 6 mm particles systems are compared through experiments #46 and #62.

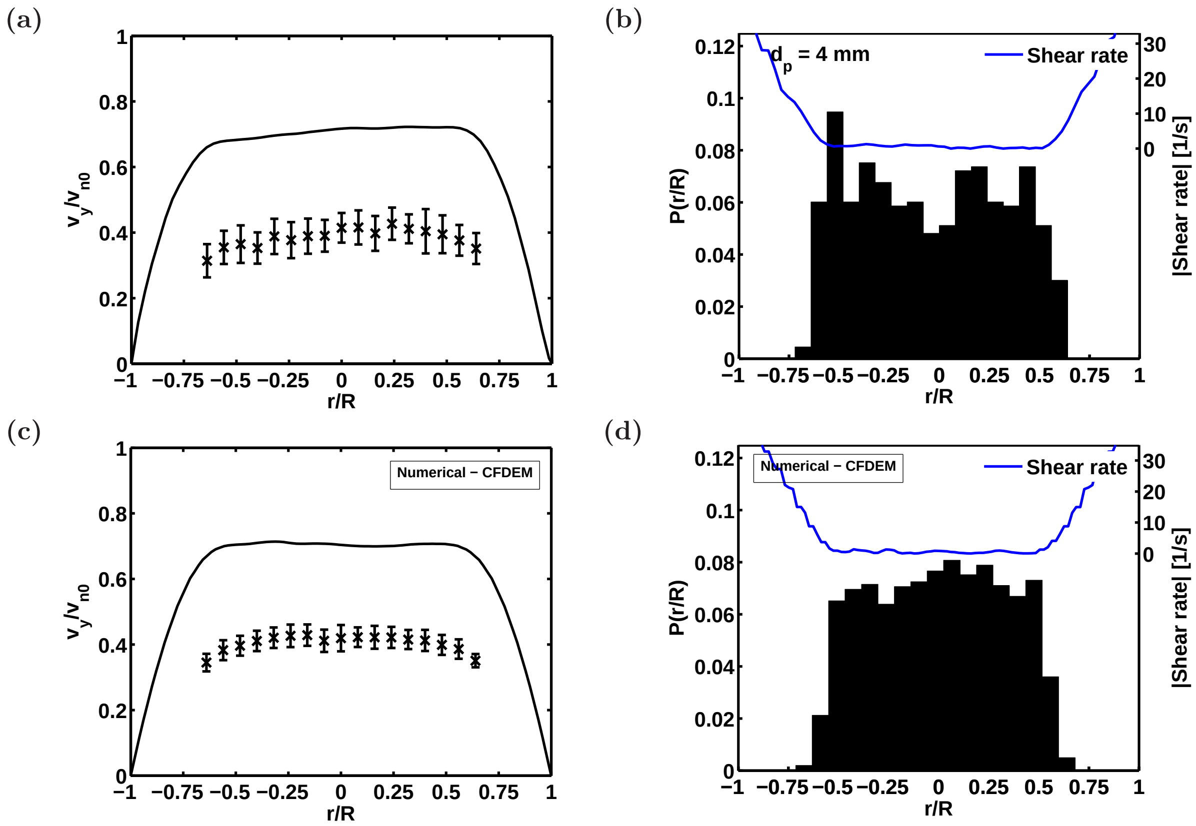

Figure 6.12: Comparison of the vertical velocities of the 4 mm particles and normalized histograms of the particle positions for experiment #15, $\phi_4 = 0.62\%$. ×, vertical velocities of the 4 mm particles, —, locally averaged fluid velocity profile: (a and b) experimental results and (c and d) numerical results.

6.2.4.1 Bidisperse suspensions of 2 and 4 mm particles

Figure 6.13 displays the first comparison of bidisperse systems results. Figures 6.13 (a), (c) and (e) offer the diagrams of the experimental results and (b), (d) and (f) the diagrams of the simulation results. The liquid velocity profiles show good matching as in the monodisperse transporting systems. Conversely, particle velocity profiles display several distinct features. First of all, the 2 mm particles, distinguished through the × symbol, exhibit lower slip velocities in the simulations. Considering the momentum transfer study between species introduced in section 5.5.4, this could indicate imprecise modelling of the drag forces acting on the 2 mm particles. On the other hand, 4 mm particles, represented by the $*$ symbol, show similar values in both experiment and simulation. Secondly, particle velocity fluctuations, also shown in table 6.2, are much lower in the simulations. This is a symptom of lower particle interaction. Finally, the particle average velocities show lower variation in the simulation. This is thought to be caused by the much larger amount of particles evaluated in the simulations than in the physical experiments.

With reference to the particle histograms, similar positions are covered for both 2 and 4 mm particles. With reference to the shapes of the particle histograms, 2 mm particles display more centred positions than in the experiments with a peak at positions around the axis. The higher concentration around the axis is also predicted for 4 mm particles, whereas this agrees with experimental results.

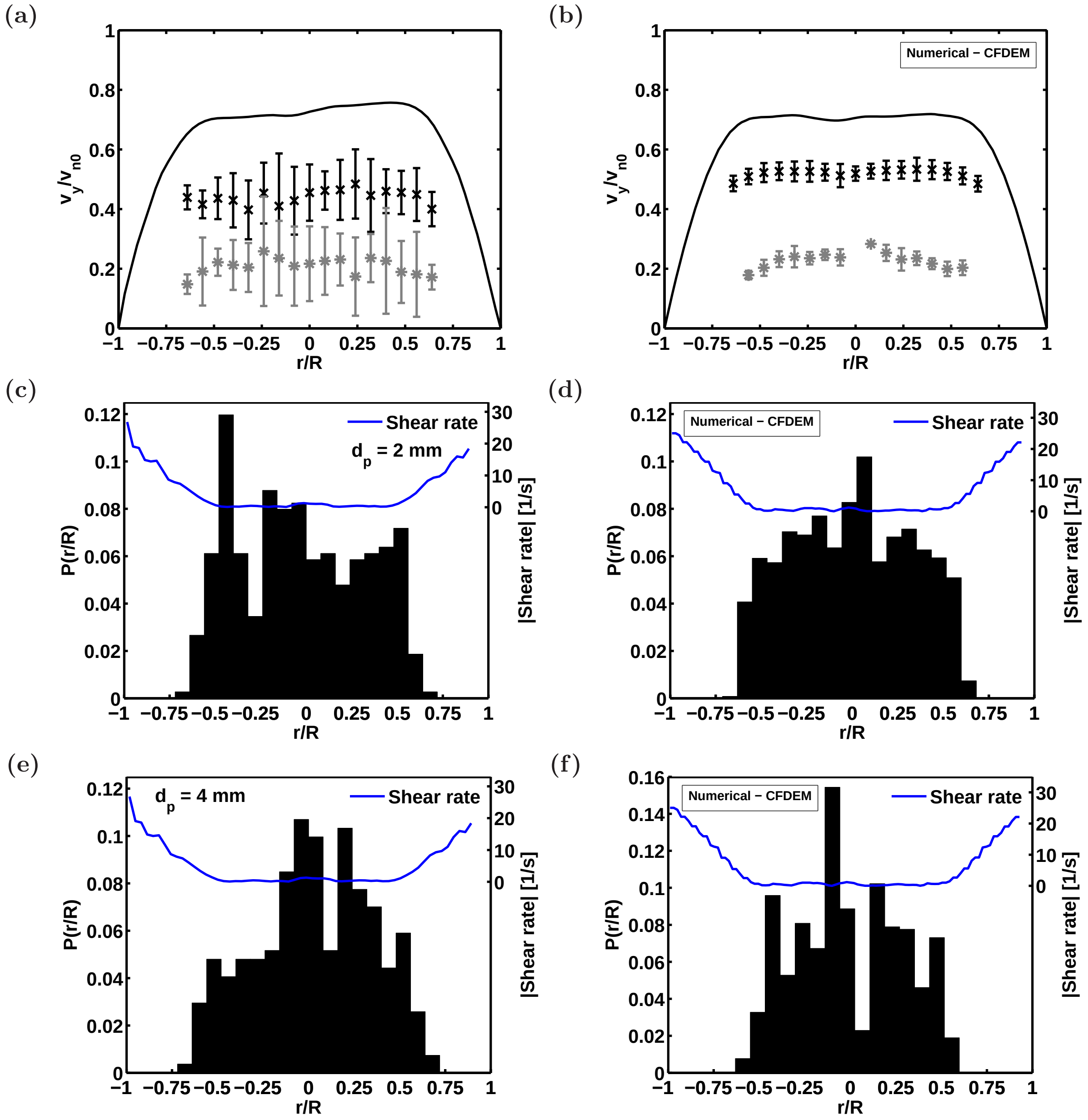

Figure 6.13: Comparison of the vertical velocities of 2 and 4 mm particles and normalized histograms of the particle positions for experiment #2, $\phi_2 = 0.25\%$ and $\phi_4 = 0.25\%$. ×, average vertical velocities of the 2 mm particles, I, standard deviation for 2 mm particles, *, average vertical velocities of the 4 mm particles, I, standard deviation for 4 mm particles, —, fluid velocity profile: (a, c and e) experimental results, (b, d and f) numerical results with CFDEM.

Increasing the concentration of both species up to $\phi_2 = 0.37\%$ and $\phi_4 = 0.62\%$ experiment

#6 is obtained. The comparison between experiments and simulation is shown in figure 6.14. Velocity profiles are in good agreement. Owing to the the purity of the boundary conditions in the simulations, the predicted values display more uniformity. Likewise, the particle velocity fluctuations are also lower than in the experiments. With regard to the particle histograms, the main difference is the inability of the simulation to obtain the concentration peaks observed in the experiments. The cause for this difference is deemed on the discretization of the CFD grid. The necessity to use cells larger than the particles for the void fraction model selected, translates in velocity field resolution lower than the necessary one to capture relevant velocity gradients. This is observed in figures 6.14 (d) and (f), where the shear rates do not show the change of sign observed in the experiments shown in figures 6.14 (a) and (b). This finally translates in the inability to capture the three-way coupling effect observed in the experiment and detailed in section 6.1.2.

6.2.4.2 Bidisperse suspensions of 4 and 5 mm particles

Figure 6.15 shows the first comparison between experiments and simulations performed for 4 and 5 mm particles. The first important difference is the liquid velocity. In the simulation, shown in figure 6.15 (b) the fluid velocity is clearly over predicted. As a result, the particle velocity profiles are also larger than in the experiment. With reference to the particle positions, no concentration peaks are observed for 4 mm particles as in the experiments. On the other hand, 5 mm particles show much better agreement.

The comparison of experiment #37, where particle concentrations are increased up to ϕ_4 = 1.50% and ϕ_5 = 1.50%, is displayed in figure 6.16. In figure 6.16(a) the wall channelling effect, already commented in section 6.1.2, may be clearly appreciated. By contrast, figure 6.16(b) shows no trace of this phenomenon. In other words, the simulation is not able to capture it. Again here, liquid velocity profiles are over predicted. This indicates deficiency of the models in replicating momentum transfer between liquid and particles as well as between particles and particles. The increase in concentration is certainly a circumstance to consider, because at higher concentrations, the particle interactions increase. Bearing in mind the inclusion of models considering particle collisions, this suggests that hydrodynamic effects play here a relevant role. Therefore, it is recommended to introduce more detailed models as the one by Kempe anf Fröhlich [45] for particles in viscous fluids. These are able to consider the forces appearing when particles approach walls or other particles known as lubrication forces. Moreover, particle velocities are influenced by the higher fluid velocities causing the over prediction of the former. A further disagreement is observed in the difference between species velocities. While the experiment shows very close velocities, the simulation still predicts a noticeable difference. On the other hand, particle velocity fluctuations are in this case very similar to the experimental ones. This is is quantified in table 6.2.

With regard to the particle positions, the same observations as for experiments #6 (figure 6.14) and #20 (figure 6.15) about the lack of concentration peaks can be done here. This results in histograms with particles concentrated around the pipe axis, while the experiment shows more homogeneous distributions for both, 4 and 5 mm particles.

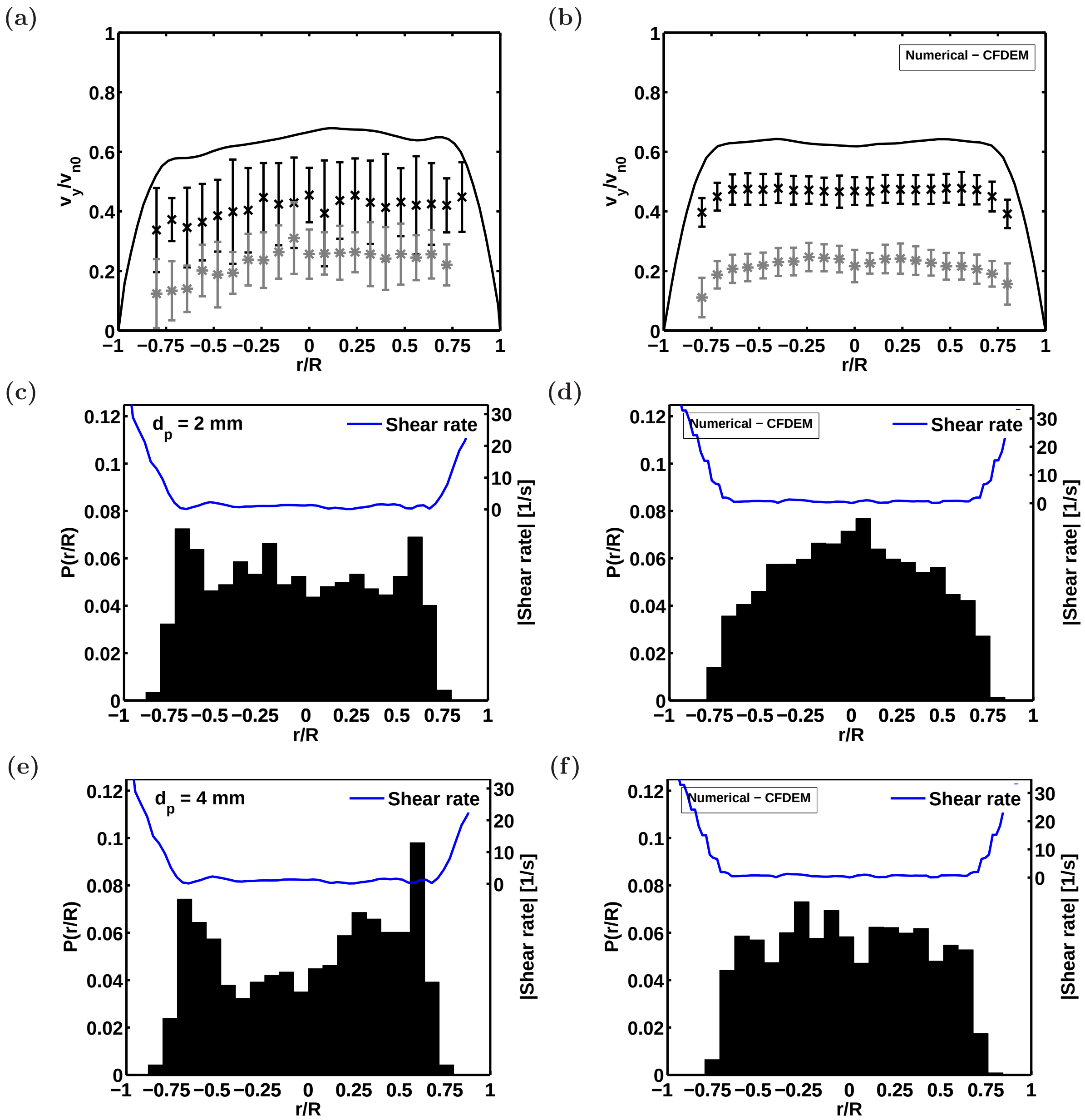

Figure 6.14: Comparison of the vertical velocities of 2 and 4 mm particles and normalized histograms of the particle positions for experiment #6, $\phi_2 = 0.37\%$ and $\phi_4 = 0.62\%$. ×, average vertical velocities of the 2 mm particles, I, standard deviation for 2 mm particles, *, average vertical velocities of the 4 mm particles, I, standard deviation for 4 mm particles, —, fluid velocity profile: (a, c and e) experimental results, (b, d and f) numerical results with CFDEM.

6.2.4.3 Bidisperse suspensions of 4 and 6 mm particles

Finally, 4 and 6 mm particle systems are compared. Experiment #46, displayed in figure 6.17, suffers of similar problems as for systems with 4 and 5 mm particles. Fluid velocity

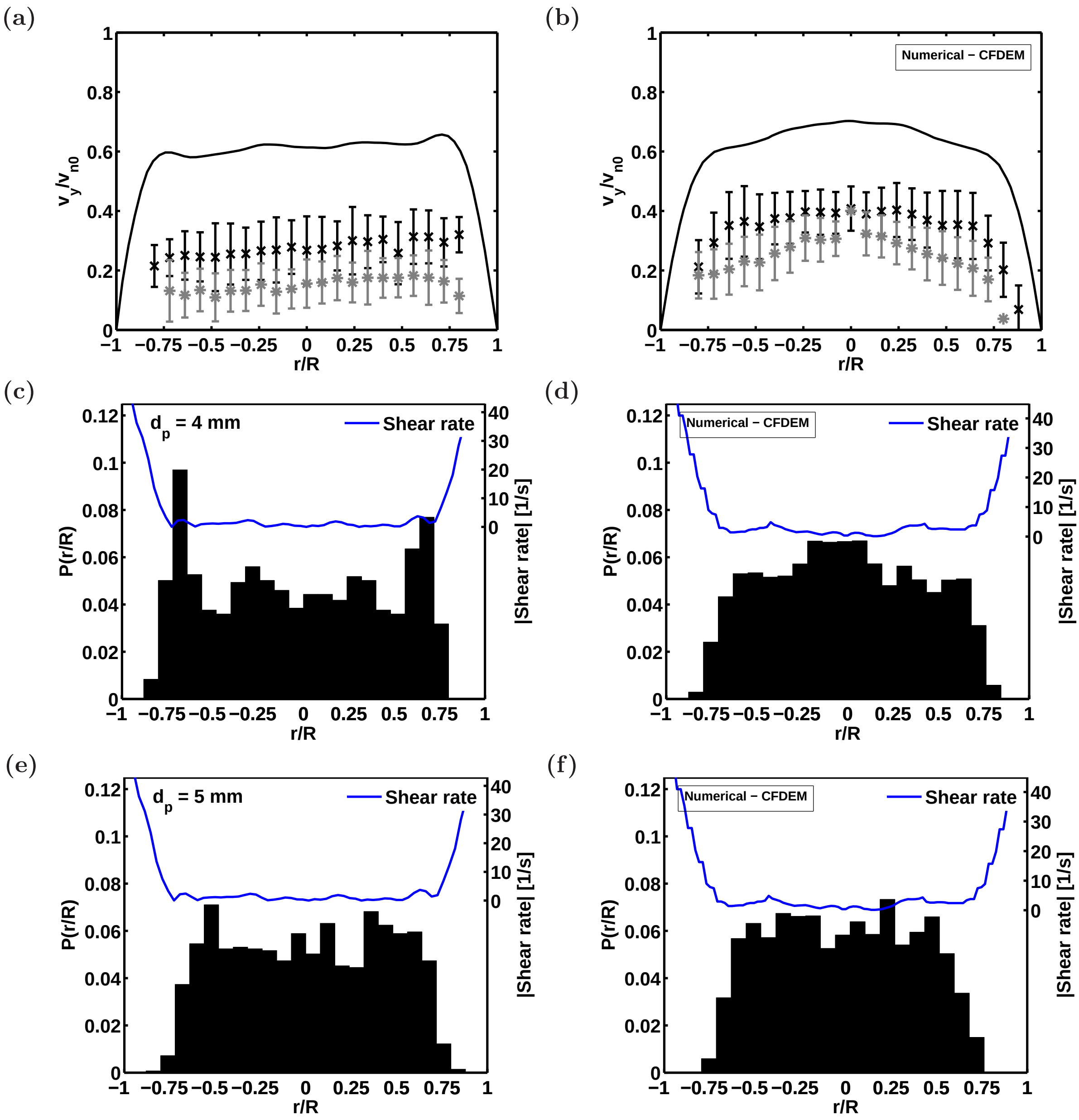

Figure 6.15: Comparison of the vertical velocities of 4 and 5 mm particles and normalized histograms of the particle positions for experiment #20, $\phi_4 = 0.62\%$ and $\phi_5 = 0.50\%$. $\times$, average vertical velocities of the 4 mm particles, I, standard deviation for 4 mm particles velocity, $*$, average vertical velocities of the 5 mm particles, I, standard deviation for 5 mm particles, —, fluid velocity profile: (a, c and e) experimental results, (b, d and f) numerical results with CFDEM.

is over predicted and the low resolution of the grid does not capture the change in sign of the shear rate. Fluctuations are in this case larger than in the experiment, whereas the difference between velocities species is in agreement. Looking at the particle histograms, concentration peaks are not observed in figure 6.17 (d). In addition, 6 mm particles

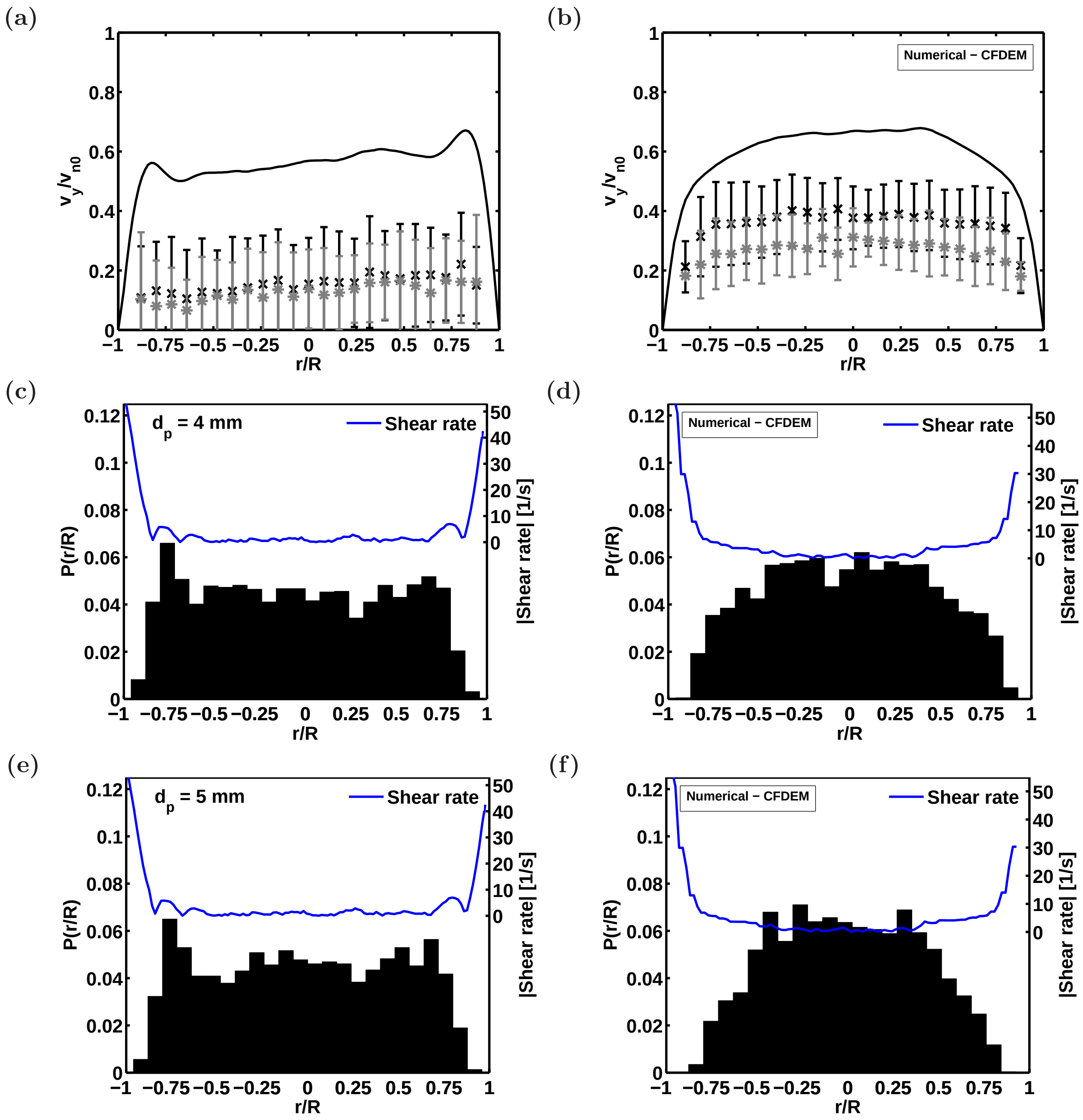

Figure 6.16: Comparison of the vertical velocities of 4 and 5 mm particles and normalized histograms of the particle positions for experiment #37, $\phi_4 = 1.50\%$ and $\phi_5 = 1.50\%$. ×, average vertical velocities of the 4 mm particles, I, standard deviation for 4 mm particles velocity, *, average vertical velocities of the 5 mm particles, I, standard deviation for 5 mm particles, —, fluid velocity profile: (a, c and e) experimental results, (b, d and f) numerical results with CFDEM.

are strongly concentrated on the pipe axis. A feature not so clearly observed in the experiment.

The last comparison corresponds to experiment #62, where concentrations are increased up to $\phi_4 = 2.00\%$ and $\phi_6 = 2.00\%$. Again here the liquid disturbances are not observed

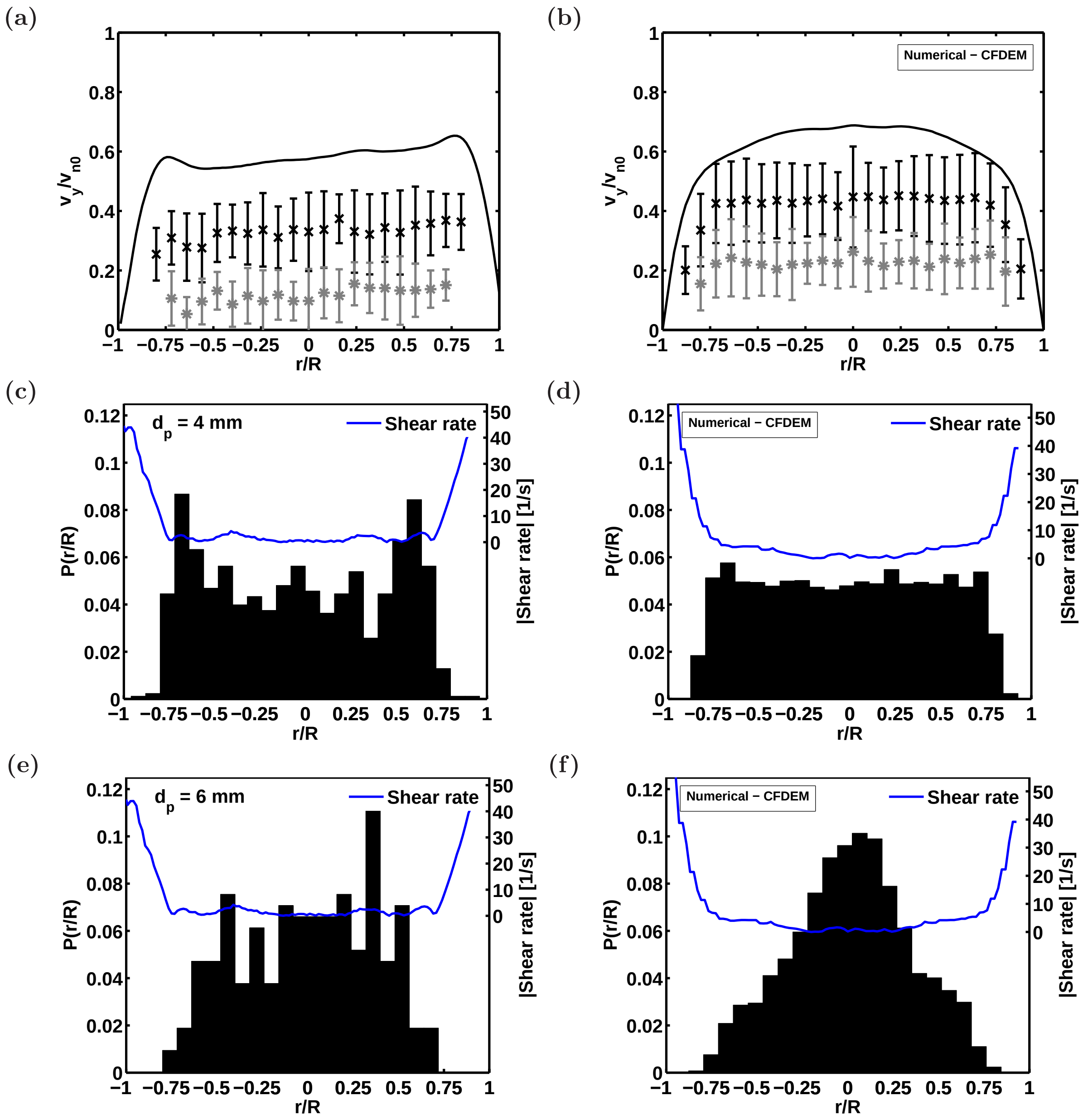

Figure 6.17: Comparison of the vertical velocities of 4 and 6 mm particles and normalized histograms of the particle positions for experiment #46, $\phi_4 = 1.00\%$ and $\phi_6 = 0.25\%$. ×, average vertical velocities of the 4 mm particles, I, standard deviation for 4 mm particles velocity, *, average vertical velocities of the 6 mm particles, I, standard deviation for 6 mm particles, —, fluid velocity profile: (a, c and e) experimental results, (b, d and f) numerical results with CFDEM.

and velocities are over predicted. Particle velocity fluctuations are in the same range, but the difference between species velocities is in disagreement with the experiment. The distribution of 4 mm particles covers almost the complete cross-section, an aspect also observed in the experiment. Although the peak concentrations of the experiments are not so pronounced in this case, the simulation is still unable to replicate them. For 6 mm particles, shown in figure 6.18, histograms repeat the trend observed for experiment #46 of particles concentrated around the axis, whereas experimental results show a more homogeneous distribution.

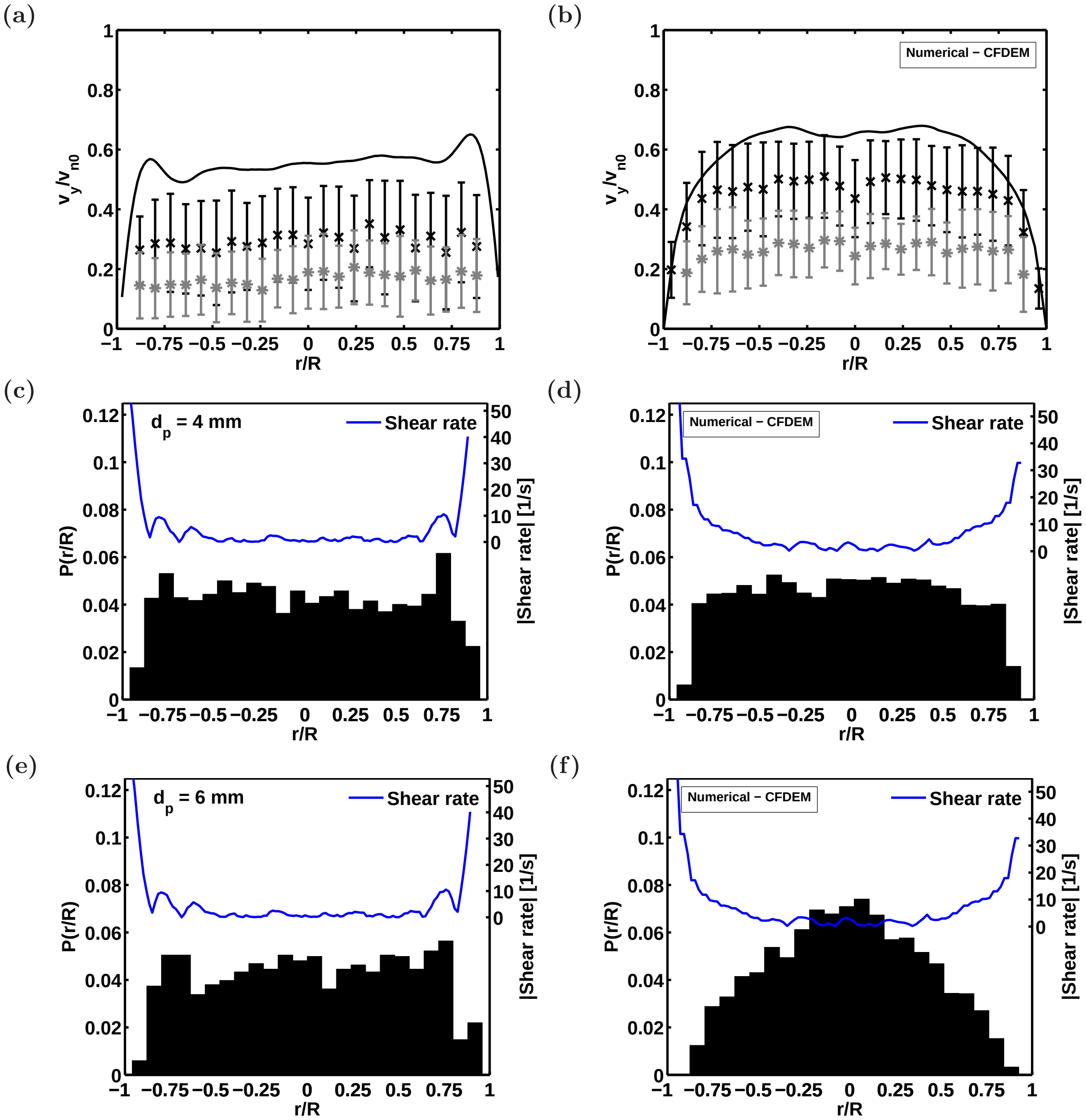

Figure 6.18: Comparison of the vertical velocities of 4 and 6 mm particles and normalized histograms of the particle positions for experiment #62, $\phi_4 = 2.00\%$ and $\phi_6 = 2.00\%$. ×, average vertical velocities of the 4 mm particles, I, standard deviation for 4 mm particles velocity, $*$, average vertical velocities of the 6 mm particles, I, standard deviation for 6 mm particles, —, fluid velocity profile: (a, c and e) experimental results, (b, d and f) numerical results with CFDEM.

6.3 CFD-DEM transport parameters in annular flows

The simulations performed in this section have the intention to supply information about the transport processes taking place within the wellbore. Such experiments are very demanding or impossible to perform in physical setups because of the characteristics of the medium and the operational conditions. Likewise, the broadness of the parameter space makes the experimental campaigns specially laborious. Moreover, simulations are able to quantify the process in a much more detailed form and with less effort than would be possible in a physical model. Due to the resolution of the models, these focus on small sections of the wellbore in the order of 1 meter. Firstly, the setup of the simulations is explained. After that, the processing of the data to obtain distribution coefficients C_0, drift-flux velocities V_{pj} and superficial velocities of the particles V_{Sp} as well as other relevant integral parameters is described. Finally, an analysis of the effect of eccentricity on cuttings transport is presented.

6.3.1 Setup

The main idea is to conduct a sensitivity analysis centred on the eccentricity parameter, but also considering variation of complementary parameters present in the wellbore as particle diameter, flow rate, dynamic viscosity and particle volume fraction. To quantify such effects, distribution coefficients C_0, drift-flux velocities V_{pj} and superficial velocities of the particles V_{Sp} are generated through numerical simulations. The numerical experiments are performed in 1 meter long annular conducts with three different eccentricities, that is concentric, 25% and 50% eccentricity. In order to obtain developed results, it is necessary to use periodic boundary conditions and a momentum source continuously calculated to sustain a specified velocity. The outer and inner diameters of the annular section are 250 mm and 125 mm respectively.

For the CFD side, the geometry is discretized with a three-dimensional structured curvilinear grid composed of hexahedrons. The grid is shown in figures 6.19. This is formed with one O-grid covering the full length of 1,000 mm. The number of elements is selected on the basis of a grid analysis performed with the liquid phase first and with both phases afterwards. This results in O-grids dicretized with 40 elements in the azimuthal direction, 10 in the radial direction and 50 in the axial direction. This adds to a total of 20,000 elements.

For the DEM side, a computational domain formed by a cylinder of 250 mm diameter and 1,000 mm length is used. This domain is delimited with the surfaces of the CFD geometry to maintain the particles within the annular gap.

The physical modelling is based on the numerical model introduced in chapter 4 and the settings investigated in section 6.2. The complete settings of the simulation are shown in table 6.4. To reduce the amount of simulations performed, a simulation matrix obtained through an Optimal Space-Filling (OSF) design of experiments was performed. This one generated 4 basic experiments with variation of the complementary parameters as shown in table 6.3. The densities of the liquid and the particles were kept constant at 1,000 and

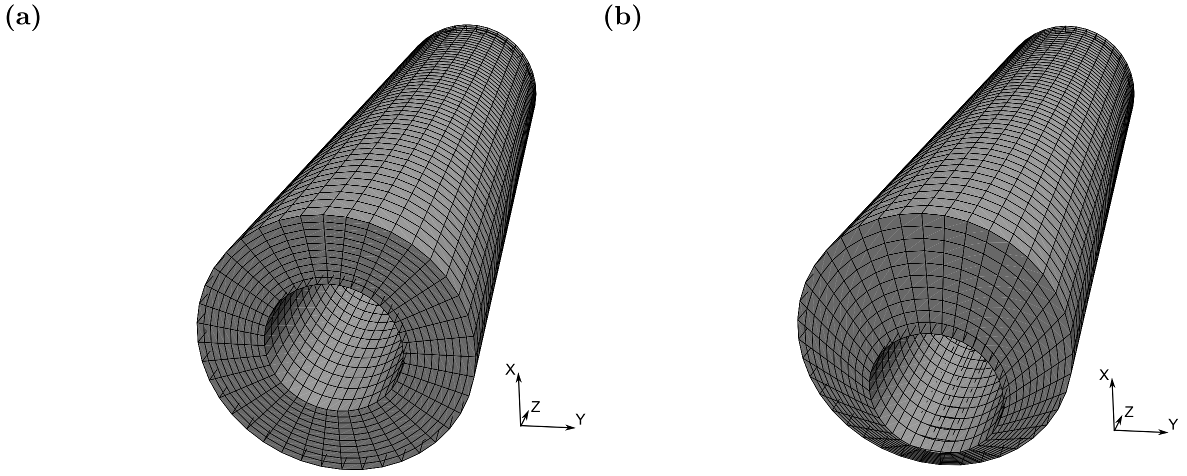

Figure 6.19: Discretized geometry: (a) Concentric geometry (b) 80% eccentric geometry.

2,500 kg/m^3 respectively.

Basic Experiment	Particle Diameter d_p (mm)	Fluid average velocity u_l (m/s)	Dynamic Viscosity η (mPa·s)	Particle Volume Fraction ϕ (%)
S1	4	0.7	50	5
S2	4	0.6	75	2.5
S3	6	0.7	50	1
S4	5	0.5	30	1

Table 6.3: Complementary parameters for the basic experiments.

The particle properties used in the sensitivity analysis are the ones obtained from the comparison with experiments in section 6.2 and listed in table 6.1. As previously commented, the reduction of the Youngs's Modulus to $E = 27$ MPa results in particle properties with greater similarity to those found in the cuttings transport problem.

Again here, model *type A*, volume fraction `divided`, *DiFelice's* drag model, *Mei's* lift model and buoyancy through `Archimedes` force model are selected for all the simulations.

Periodic boundary conditions are implemented in this case. The information of the fields solved at the `top_wall` boundary, shown in figure 6.20, is the same for the `bottom_wall`. In order to maintain an average constant velocity, it was necessary to modify one of the three available solvers in the CFDEM library (`cfdemSolverPiso`) and introduce a source of momentum. The solver gets the average fluid velocity in every cell of the computational domain and calculates the necessary momentum source, which is later applied in the momentum conservation equation. At `inner_wall` and `outer_wall` the liquid velocity is set to null to impose the no-slip boundary condition. The particles are stochastically distributed across the computational domain of the outer conduct. The number of particles is automatically calculated by LIGGGHTS according to the volume fraction of each basic experiment, as listed in table 6.3. Before the CFD part of the simulation starts, the particles located within the inner annular conduct are deleted. Such procedure facilitates the automatic creation of simulation cases. Furthermore, the initial velocities of the particles are set to null and acquire the settling velocity with the simulation progress in time. The `top_wall` and `bottom_wall` boundaries are also set as periodic boundary conditions for the particles. This setting artificially forces the volume fraction in the computational domain to remain constant. Finally, Hookean collision modelling is set for the particle-particle and particle-wall contacts.

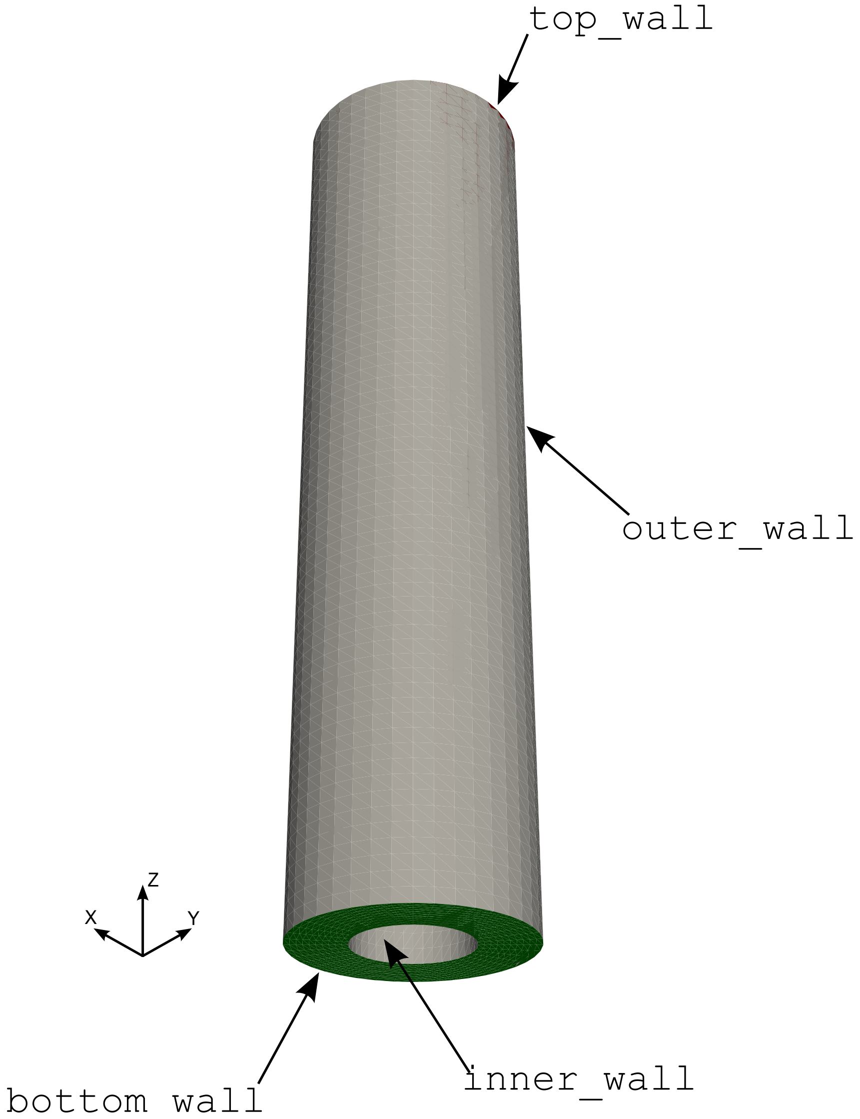

Figure 6.20: Definition of the boundaries in the eccentric computational domain.

6.3.2 Data processing

The results obtained from the CFDEM simulations are divided between the fields solved by the CFD side, that is liquid velocity v_l, particle velocity v_p, particle volume fraction ϕ_p,

Variables	Values
Pipe geometry:	
Inner diameter	125 mm
Outer diameter	250 mm
Eccentricity	concentric to 80 % eccentricity
Length	1,000 mm
Number of cells	20,000
Particle properties:	
Particle diameters (d_{pi})	4 - 6 mm
Particle densities	2,500 kg m^{-3}
Young's Modulus (E)	2.5×10^7 Pa
Poisson ratio (ν)	0.2
Coefficient of restitution (e)	0.77
Friction coefficient (μ)	0.2
Volume fractions	1 - 5 %
Fluid properties:	
Density	1,000 kg m^{-3}
Viscosity	η = 30 - 75 mPa·s
Fluid velocity	0.5 - 0.7 m/s

Table 6.4: Parameters used in the sensitivity analysis for eccentricity simulations.

pressure p, and the particle information solved by the DEM side, that is position, velocity, rotational velocity and force for each particle. In figure 6.21 an exemplary visualization of the solved flow fields and particle positions and velocities is shown. From these results, the ones processed to obtain the parameters used to quantify the efficiency of the cuttings transport, that is distribution coefficient C_0, drift-flux velocity of the particles V_{pj} and superficial velocity of the particles V_{Sp}, are those of the CFD part. Indeed, information from both sides is contained in the CFD outcome, because the CFD and DEM results are connected through the particle volume fraction ϕ_p, calculated according to the particle positions and properties solved and defined in the DEM solver, and through the particle velocity v_p, averaged at every CFD cell from the results obtained in the DEM side. In other words, due to the integral nature of the transport parameters, no further processing of the DEM results is required. The transport parameters are obtained from equations already presented in section 2.1.4. C_0 supplies information about the distribution of the particles across the cross-sectional area. In this respect, values of C_0 equal to 1, indicate a homogeneous distribution as normally assumed in cuttings transport, values larger than 1 indicate distribution of the particles at positions where liquid velocity is high and values lower than one at positions where the liquid velocity is low, e.g. close to the walls,

$$C_0 = \frac{\overline{\varepsilon_p j_M}}{E_p V_M}, \tag{6.9}$$

where ε_p is the local particle volume fraction, j_M the local mixture volumetric flux, E_p the particle cross-sectional average *in situ* fraction and V_M the mixture average velocity. On the other hand, the drift flux velocities of the solid particles V_{pj} may be seen as a more complex version of the settling velocity, since this is able to include the effects of local concentrations and local liquid velocities. Furthermore, it must be pointed out that the drift-flux velocity gives the velocity difference between the mixture and dispersed phase and not the liquid and the dispersed phase as given by the settling velocity.

$$V_{pj} = \frac{\overline{\varepsilon_p v_{pj}}}{E_p}, \tag{6.10}$$

where v_{pj} is the local particle drift velocity. The previous values are obtained from the field variables solved in the simulations at the cells intersected by the 20 layers shown in figure 6.22. Further treatment of the local field variables as shown in equations 6.11 to 6.14 is required.

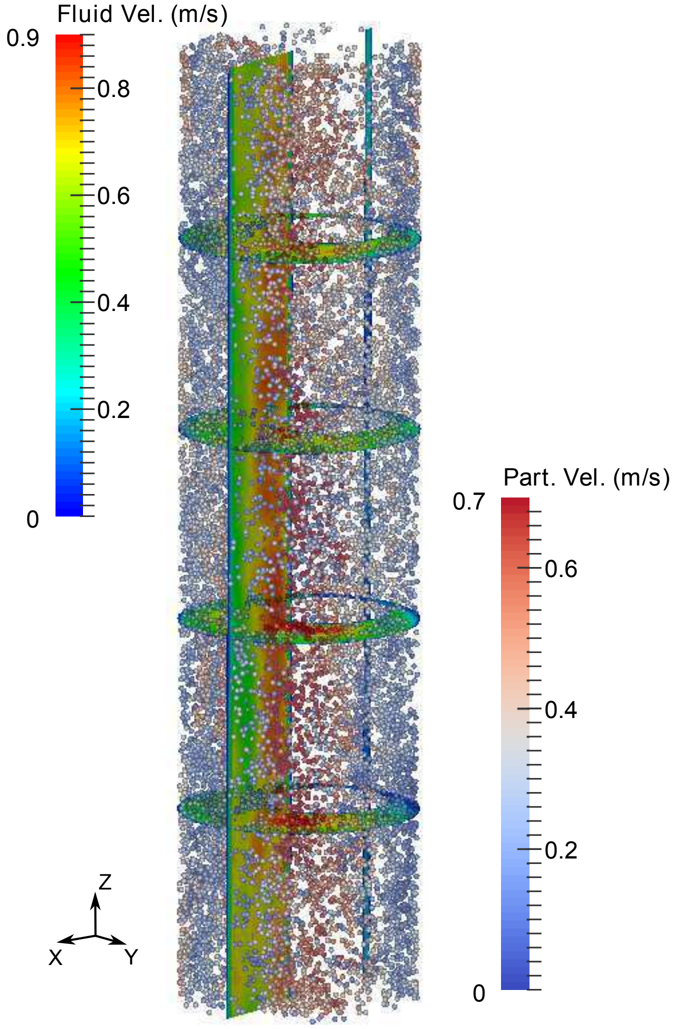

Figure 6.21: Visualization of the flow field and particle positions and velocities.

$$\overline{\varepsilon_p J_M} = \frac{1}{A} \sum_{i=1}^{n} \varepsilon_{pi} (\varepsilon_{pi} v_{pi} + (1 - \varepsilon_{pi}) v_{li}) A_i, \tag{6.11}$$

$$\overline{\varepsilon_p v_{pj}} = \frac{1}{A}\sum_{i=1}^{n} \varepsilon_{pi}(v_{pi} - (\varepsilon_{pi} v_{pi} + (1-\varepsilon_{pi}) v_{li})) A_i, \tag{6.12}$$

$$E_p = \frac{1}{A}\sum_{i=1}^{n} \varepsilon_{pi} A_i, \tag{6.13}$$

$$V_M = V_{Sl} + V_{Sp} = \frac{1}{A}\sum_{i=1}^{n} \varepsilon_{li} v_{li} A_i + \frac{1}{A}\sum_{i=1}^{n} \varepsilon_{pi} v_{pi} A_i, \tag{6.14}$$

where A_i is the cross-sectional area of the corresponding cell.

Before the results are processed, the simulations are run until the flow has reached a stable condition. This is quantified through the distribution coefficient C_0 at 20 annular cross-sections along the axial direction as shown in figure 6.22. After around 60 seconds the value of C_0 reaches an asymptotic value. From this point, the next 20 seconds are evaluated to obtain the average value of the distribution coefficient C_0, the drift-flux velocity V_{pj} and the superficial velocity V_{Sp} of the particles.

6.3.3 Eccentricity variation

The results of the eccentricity variation analysis are presented by commenting the outcomes of every single experiment with its corresponding eccentricities in ascending order. The observations of the presented figures are put in relation with quantifiable data as the drift-flux parameters. Finally, a comparison between these data is depicted through bar diagrams to identify characteristics and trends.

Figure 6.23 shows the results for the three different configurations of experiment #S1. In the concentric configuration, an axisymmetric distribution of particles is observed. Likewise, the distribution of particles appears homogeneous. Two regions clear of particles around the inner and outer walls are also observed. These are caused by the lift force as already observed in the physical experiments and simulations of the vertical flow-loop. Figure 6.24 shows the distribution of particles seen from the side for all experiments. Experiment #S1 with the largest volume fractions shows the most dense condition. In figure 6.23(b), the 25% eccentric configuration is shown. Contrary to the concentric case, there is no axisymmetric distribution of particles. However, plane XZ constitutes a plane of symmetry. In the narrower gap of the annulus wider clean particle regions are also observed. Figure 6.23(c) shows the result of increasing the eccentricity up to 50%. Also in this case plane XZ constitutes a plane of symmetry. Furthermore, much fewer particles are located in the narrow gap, which creates regions of different volume fraction within the annular conduct. Quantification of the drift-flux and integral parameters of the particle transport for all experiments and configurations is found in table 6.5. In this table, it can be observed how C_0 values are mostly larger than one. Only for experiment #S4 and concentric or 25% eccentricity the C_0 values are close to one. Moreover, eccentricity does not seem to have a consistent effect. The V_{pj} values remain relatively constant

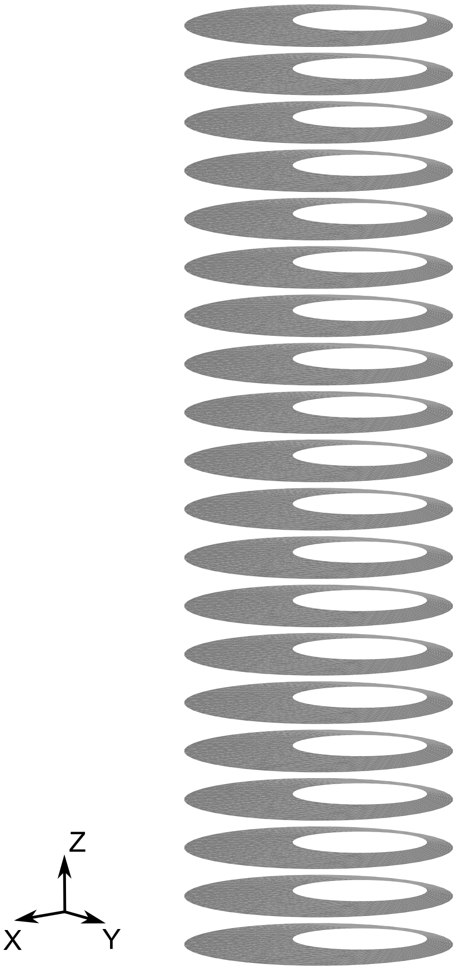

Figure 6.22: Annular cross sections along the annular geometry.

independent of eccentricity. On table 6.6, the settling velocities of the four basic experiments calculated using the Schiller & Naumann [90] and the Di Felice [100] correlations are given for comparison. While the Schiller & Naumann [90] correlation considers the effects of the liquid and particle physical properties on the settling velocity, the Di Felice [100] correlation is also able to consider the effects of volume fraction.

Figure 6.25 shows the results for experiment #S2, where lower volume fraction, higher viscosities and lower velocities than in experiment #S1 were set. The effect of lower concentrations and higher viscosities can be appreciated in the formation of more compact particle annulus at a further distance from the annular conduct walls. The larger values of parameter C_0 for experiment #S2 in comparison to experiment #S1, shown in table 6.5, quantify this observation. Likewise, eccentricity has an ambiguous effect on C_0 as depicted in figure 6.28(b). The lower V_{pj} values are due to the higher viscosity used in this experiment as also observed in the settling velocities of table 6.6.

Figure 6.26 shows the results for experiment #S3, where larger particle diameter and lower volume fraction than in experiment #S1 were set. In this case, less homogeneity is observed. Some particles reach positions close to the wall. However, the regions clear of

Experiment	Eccentricity	Volume fraction	V_M (m/s)	C_0 (-)	V_{pj} (m/s)	V_p (m/s)	V_{Sp} (m/s)	V_l (m/s)	V_{Sl} (m/s)	$V_p - V_l$ (m/s)
S1	0%	5%	0.646	1.421	-0.062	0.857	0.058	0.631	0.588	0.226
S2	0%	2.5%	0.557	1.534	-0.054	0.800	0.027	0.548	0.530	0.252
S3	0%	1%	0.653	1.484	-0.093	0.881	0.012	0.650	0.641	0.227
S4	0%	1%	0.465	1.040	-0.153	0.383	0.005	0.467	0.460	-0.135
S1	25%	5%	0.771	1.233	-0.061	0.857	0.077	0.760	0.694	0.132
S2	25%	2.5%	0.675	1.337	-0.054	0.794	0.035	0.668	0.640	0.182
S3	25%	1%	0.775	1.303	-0.096	0.841	0.015	0.772	0.759	0.142
S4	25%	1%	0.554	1.056	-0.151	0.374	0.007	0.556	0.547	-0.122
S1	50%	5%	0.713	1.313	-0.057	0.883	0.065	0.699	0.648	0.179
S2	50%	2.5%	0.617	1.504	-0.053	0.751	0.025	0.610	0.592	0.266
S3	50%	1%	0.699	1.366	-0.100	0.731	0.012	0.697	0.687	0.153
S4	50%	1%	0.505	1.300	-0.155	0.425	0.006	0.505	0.499	-0.005

Table 6.5: Integral parameters of the eccentricity analysis.

Experiment	Schiller & Naumann (m/s)	Di Felice (m/s)
S1	-0.14	-0.12
S2	-0.11	-0.1
S3	-0.23	-0.22
S4	-0.23	-0.22

Table 6.6: Settling velocities calculated with the Schiller & Naumann [90] and the Di Felice [100] correlations.

particles can still be identified. In this experiment, most of the particles are still located at high velocity locations. This can be confirmed by the results of C_0 shown in table 6.5, which remain high. The bigger size of the particles causes higher V_{pj} values. Moreover, this value slightly increases with more eccentric configurations. Such trend is contrary to the two previous experiments.

Finally, figure 6.27 shows the results for experiment #S4, where larger particle diameter, lower concentration and lower viscosity than experiment #S1 were set. For the concentric and 25% eccentricity configurations, a homogeneous particle distribution is observed. This can be confirmed in table 6.5, where the C_0 values are almost one. For 50% eccentricity, particles are concentrated in faster regions, that is the wider gap of the annular conduct, and the C_0 value increases. In this experiment, the combination of the particle size and the lower liquid viscosity results in the largest V_{pj} values.

To provide a visual comparison, the results of V_M, C_0 and V_{pj} are depicted through bar diagrams included in figure 6.28. The diagram corresponding to V_M shows very close values to the ones defined for the liquid velocity in the basic experiments only for the eccentricity 50% configurations. For the rest of the configurations a slight disagreement is observed. Values of C_0 only show correlation with eccentricity in experiment #S4. Such trend indicates a migration of the particles to faster locations as eccentricity increases. In figure 6.28(c) the V_{pj} values do not seem to be affected significantly by varying eccentricities.

The average velocities V_p and superficial velocities V_{Sp} of the particles are compared in figure 6.29. The average velocities are similar for different eccentricities for almost all the experiments. Only, experiment #S4 seems to be affected by eccentricity. Furthermore, the average particle velocities are always significantly higher than the ones predicted with the Di Felice [100] correlation assuming homogeneous distribution of the particles. V_{Sp} synthesizes information about particle velocities and volume fraction. In all the experiments, the V_{Sp} values are higher than the ones predicted assuming homogeneous distribution. This indicates the relevancy of the migration of particles to faster regions of the annular cross section. This can also be observed in figure 6.30, where for experiments #S1, #S2 and #S3 the average velocities of the particles are higher than the ones of the liquid for every eccentricity.

Figure 6.31 confirms the appreciation drawn from the values of V_M in figure 6.28. The differing liquid velocities to the ones specified require further investigations focused on the mechanism used to calculate the required momentum source.

6.4 Closure

6.4.1 Two-Fluid simulations

To explain the origin of the concentration peaks observed in some of the measured systems, simulations using the two-fluid method have been performed. An axisymmetric configuration is selected due to symmetry in the azimuthal direction inferred from the experiments. As a result, simulations of the flow in 2 meter pipe with homogeneous velocity and concentrations at the inlet compare well with monodisperse experimental measurements. The numerical simulations are then used to predict particle distributions at higher feeding concentrations. The same show the effect of the lift force and the reduction of velocity on the suspensions, which generates accumulations of particles in front of the sudden expansion creating an obstacle. The suspension arriving from upstream encounters less resistance through the space left between the obstacle and the pipe wall producing velocity profiles resembling the wall channelling phenomenon observed in porous media flow. Therefore, the presence of this obstacle formed by slower particles causes an internal modification of the velocity profile and originates shear rates of opposite direction at locations between the pipe axis and wall. Such shear rates are responsible for counteracting forces originating equilibrium positions at these same locations, where the probability to find particles increases. As previously commented, the main difference with the tubular pinch effect is related to the nature of the counteracting forces. While in tubular pinch these are caused by shear rates of different intensity, but same direction, the ones investigated here are caused by shear rates of different direction produced by the internal modification of the flow fields.

6.4.2 CFD-DEM comparison

Simulations comparing the experimental results have been performed with the CFD-DEM approach. This one allows predictions of polydisperse suspensions without the necessity to model the rheology of the suspension with closure relations. A full three-dimensional representation is selected to validate the model for cases where this is strictly necessary (e.g. annular pipes considering eccentricity, rotation or inclination). Simulations of monodisperse suspensions with low concentrations show good agreement with the experiments as long as particles are entrained. Only in the case of a fluidized bed simulations supply inaccurate predictions. The accurate prediction of the annuls free of particles reveals good modeling of the lift forces. If steady state results are required, the lift model construction is relatively unimportant as long as there is one. If fine time resolution is necessary, for example to predict the radial velocity fluctuations of the particles, accurate modelling and fine resolution of the velocity fields will be necessary.

For bidisperse systems, simulations are also accurate as long as concentrations are kept low. Once concentration is increased, better resolution of the flow fields is required to capture three-way coupling phenomenon. The relevancy of this phenomenon should be further investigated. A general trend observed in low concentration simulations, either mono- or bidisperse is lower velocity fluctuations than observed in the experiments. On the other hand, higher concentrations show good agreement. A further effect of concentration increase is the over prediction of fluid velocities. This is thought to be caused by inaccurate modelling of momentum transfer between fluid and particles. The Adaptative Collision Model (ACM) of Kempe and Fröhlich [45] is proposed as a further development. In relation to slip velocities between particles and liquid, monodisperse suspensions show very good agreement. In the case of the bidisperse suspensions, the momentum transfer observed in the experiments is not accurately reproduced and results in slight over prediction of the slip velocities for the large specie and under prediction for the smaller specie.

Considering the previous results, it is decided to continue the numerical experiments with CFD-DEM coupling regarding only monodisperse systems, while the modeling of bidisperse systems should be further investigated. These experiments have the objective to understand the effect of eccentricity on cuttings transport.

6.4.3 Superficial velocities in annular conducts

Analysis of eccentricity effects on particle transport in annular conducts has been performed through CFD-DEM. After processing of the results, one weakness of the models was identified: the lack of accuracy in the setting of average velocities. This being said, the shortcoming does not harm the general outcome of the comparison and allows acquiring insight into the cuttings transport problem.

A first conclusion of the analysis is the over prediction of particle settling velocities through the homogeneous particle distribution assumption and state-of-the-art particle settling correlations. Such over prediction results in the consequent under prediction of particle transport. The cause of this under prediction resides in the non-consideration of lift forces pushing particles to specific regions, where local average velocities are higher than the average velocity in the complete cross-section. This can be unequivocally quantified through the use of integral parameters used in the formulation of the drift-flux model. Evaluation of these parameters indicates ambiguous effect of eccentricity on the distribution coefficient C_0. However, eccentricity does not result in detrimental effects on particle vertical transport. With relation to the drift-flux velocities of the particles V_{pj}, the effect of eccentricity is not prominent.

From the results extracted, the outstanding importance of the *in situ* volume fraction can also be drawn. In this way, effective particle transport cannot only be assessed on the basis of the average velocity of the particles V_p. This needs to be done trough evaluation of the superficial velocity of the particles V_{Sp}. This parameter is able to synthesize three main aspects influencing vertical particle transport: (1) liquid and particle physical properties, (2) particle distribution and (3) volume fraction. By using this parameter, the effectiveness of good transport conditions at very low volume fractions can be compared with situations where the conditions are not as good but the volume fraction is higher. This supplies an increased understanding of the transport systems.

For the sake of exactitude in possible further model developments it is deemed convenient to find an improved manipulation of the momentum sources used in the periodic boundary conditions to adjust fluid average velocities.

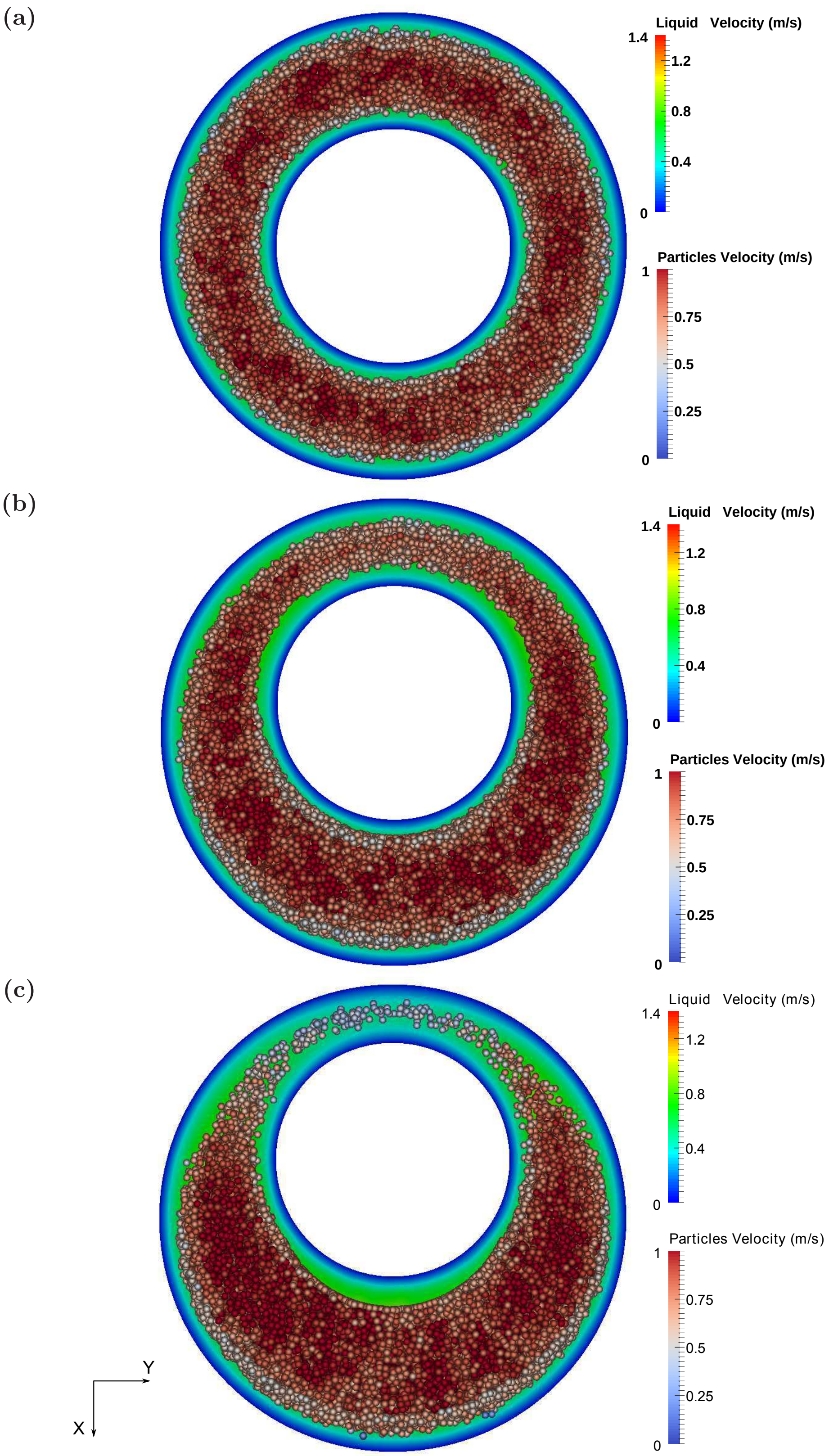

Figure 6.23: Cross sectional top views of experiment #S1: (a) concentric, (b) 25% eccentricity and (c) 50% eccentricity.

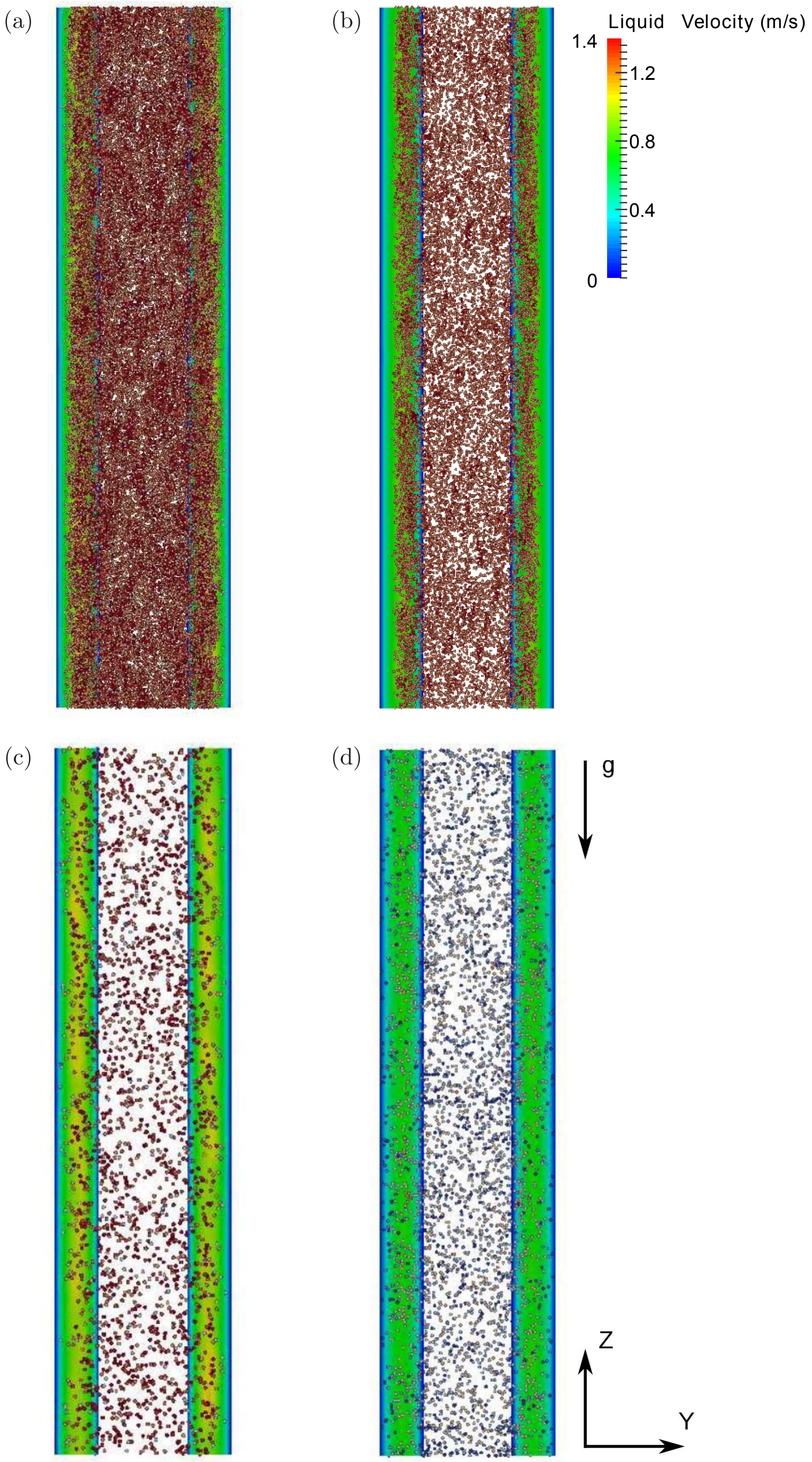

Figure 6.24: Vertical views of the concetric settings: (a) experiment #S1, (b) experiment #S2, (c) experiment #S3 and (d) experiment #S4

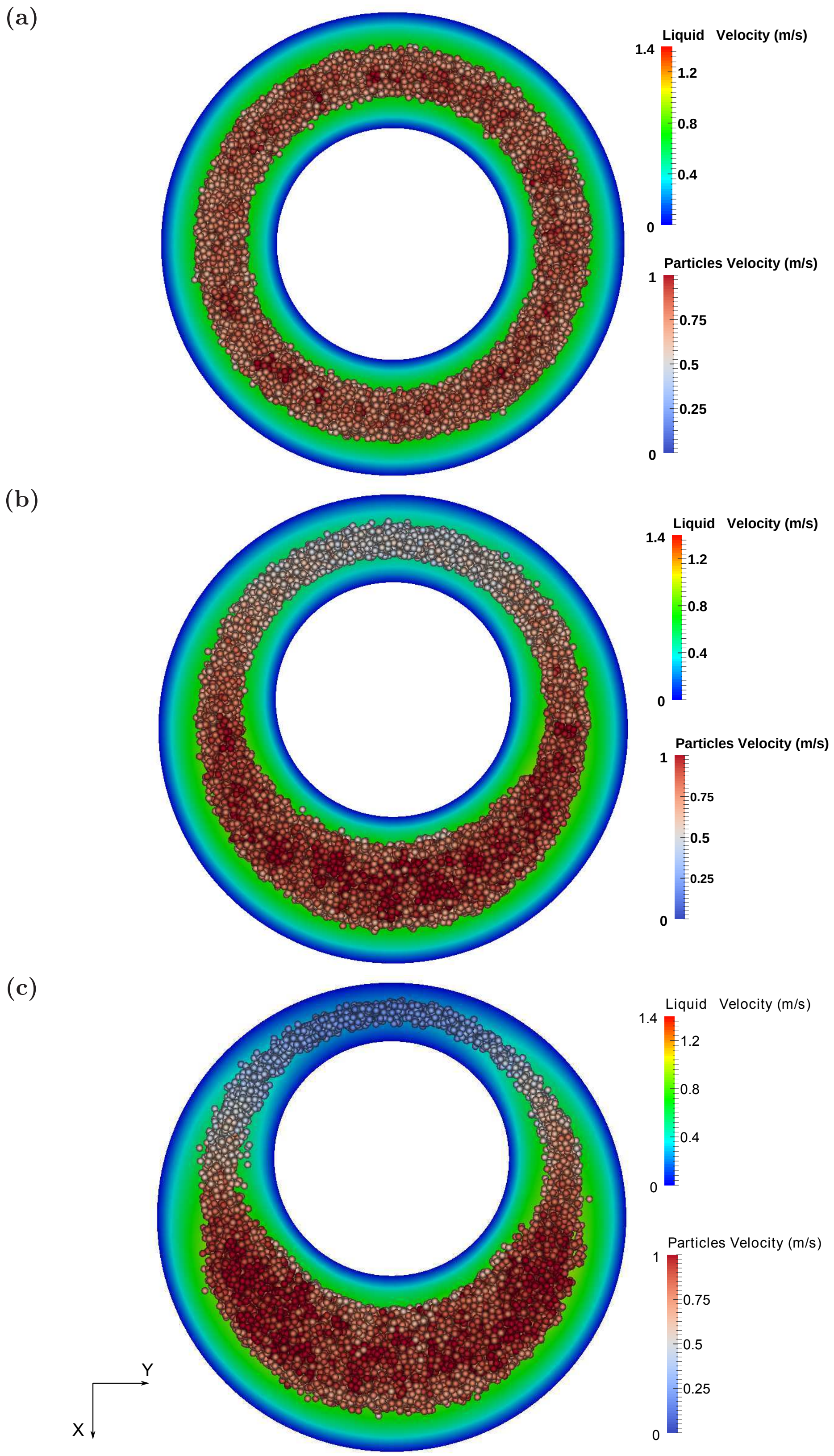

Figure 6.25: Cross sectional top views of experiment #S2: (a) concentric, (b) 25% eccentricity and (c) 50% eccentricity.

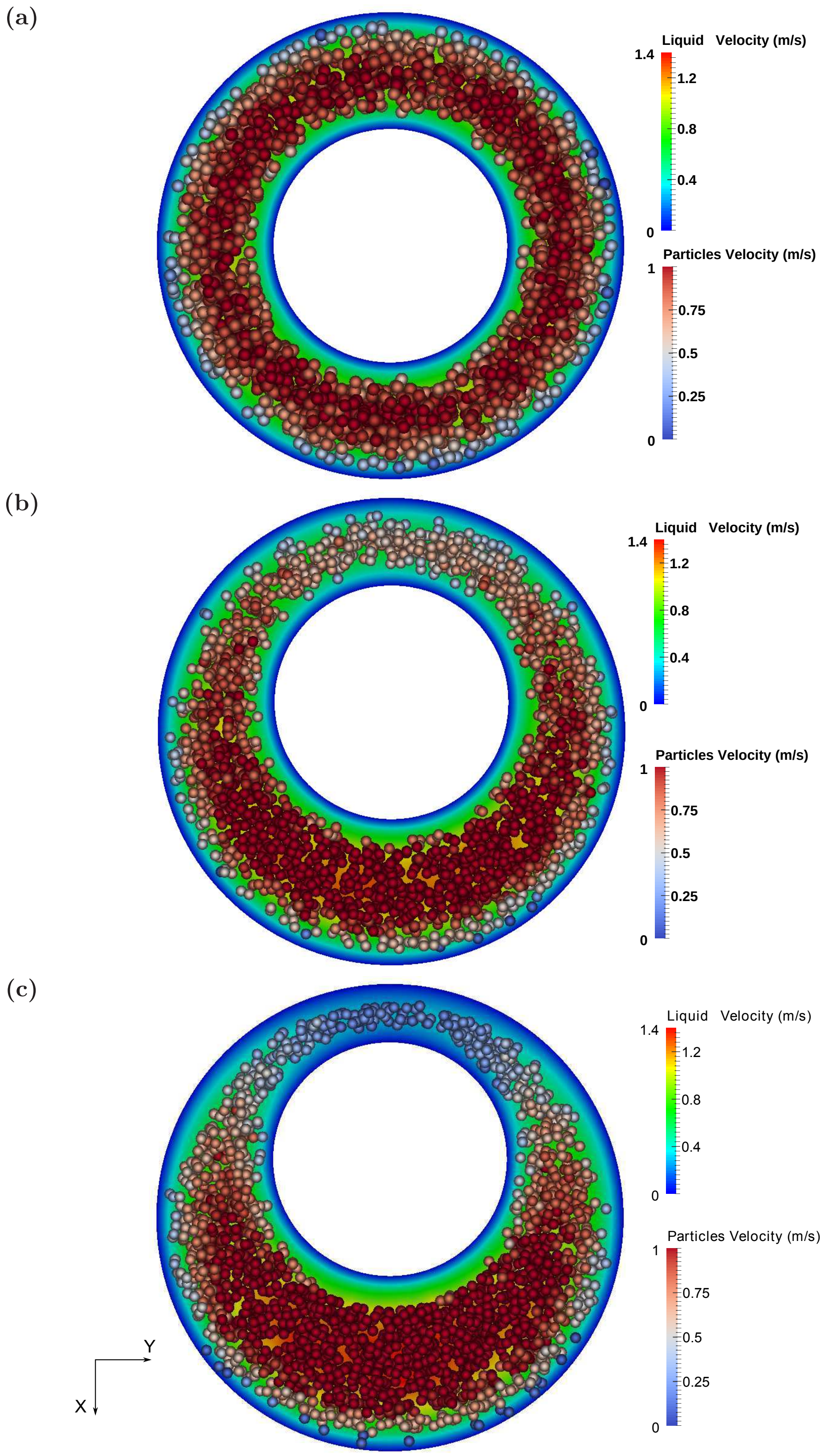

Figure 6.26: Cross sectional top views of experiment #S3: (a) concentric, (b) 25% eccentricity and (c) 50% eccentricity.

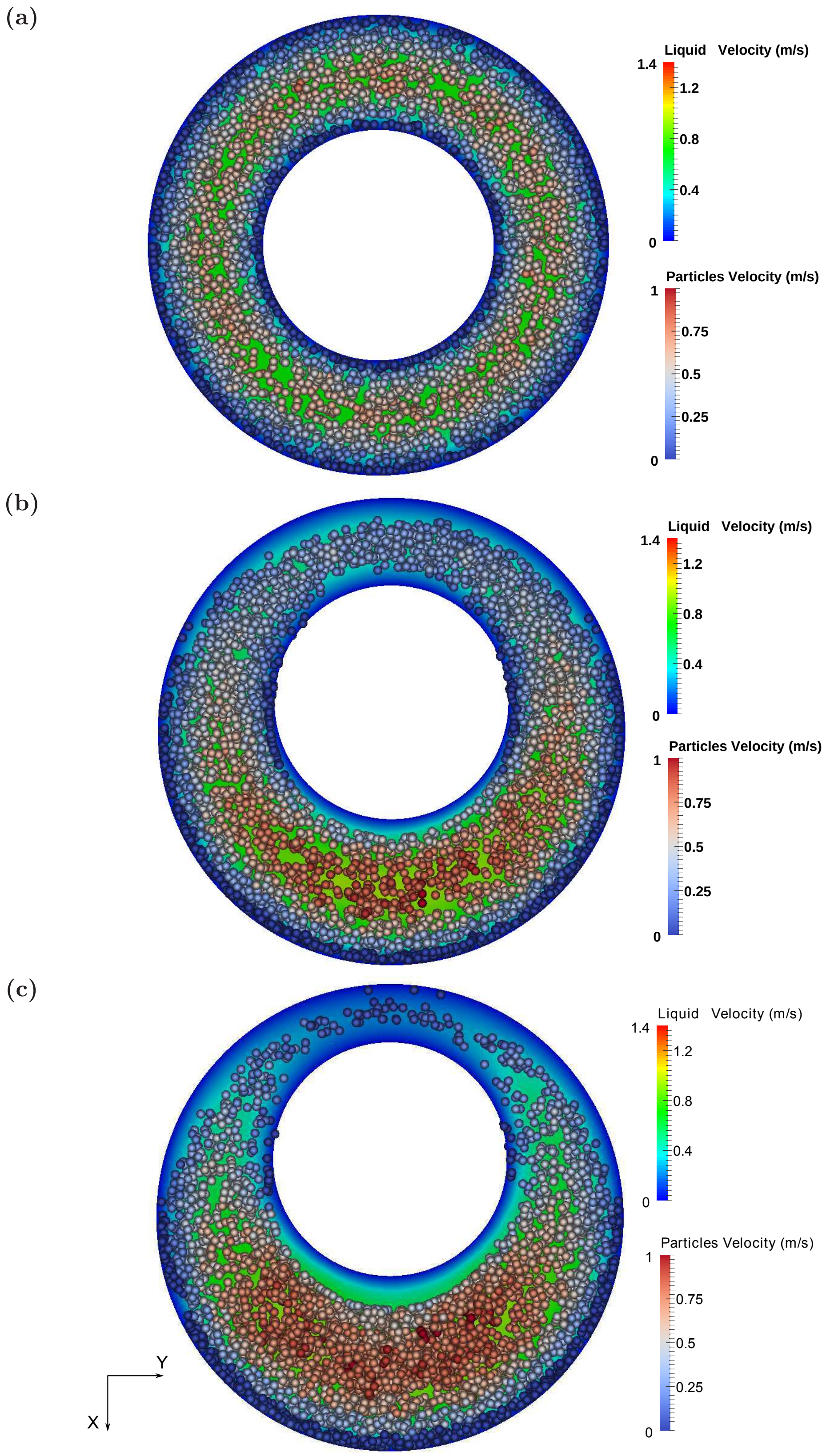

Figure 6.27: Cross sectional top views of experiment #S4: (a) concentric, (b) 25% eccentricity and (c) 50% eccentricity.

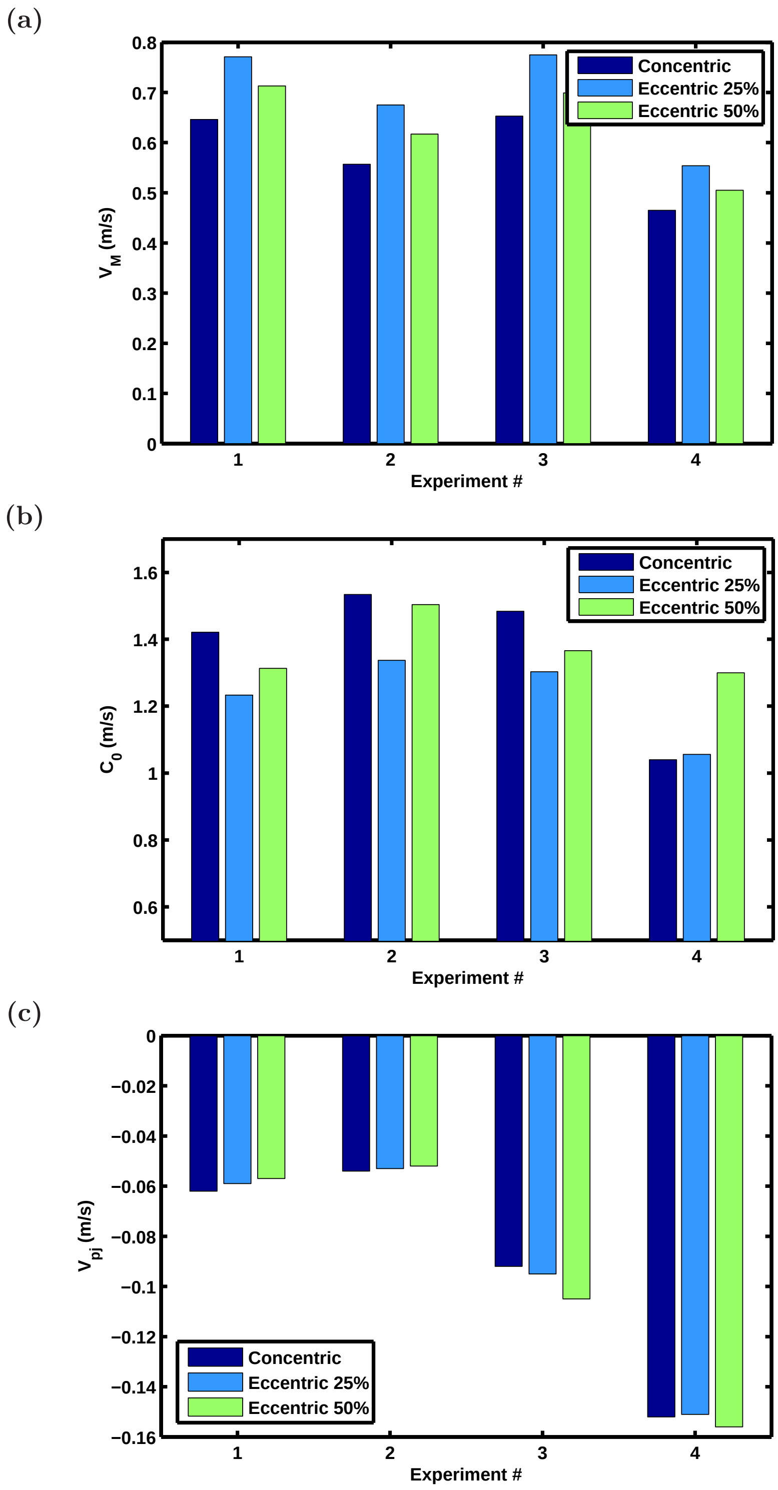

Figure 6.28: Drift-Flux velocity parameters for the 4 basic experiments: (a) mixture velocity $V_{mixture}$, (b) distribution coefficient C_0 and (c) particle drift-flux velocity V_{pj}.

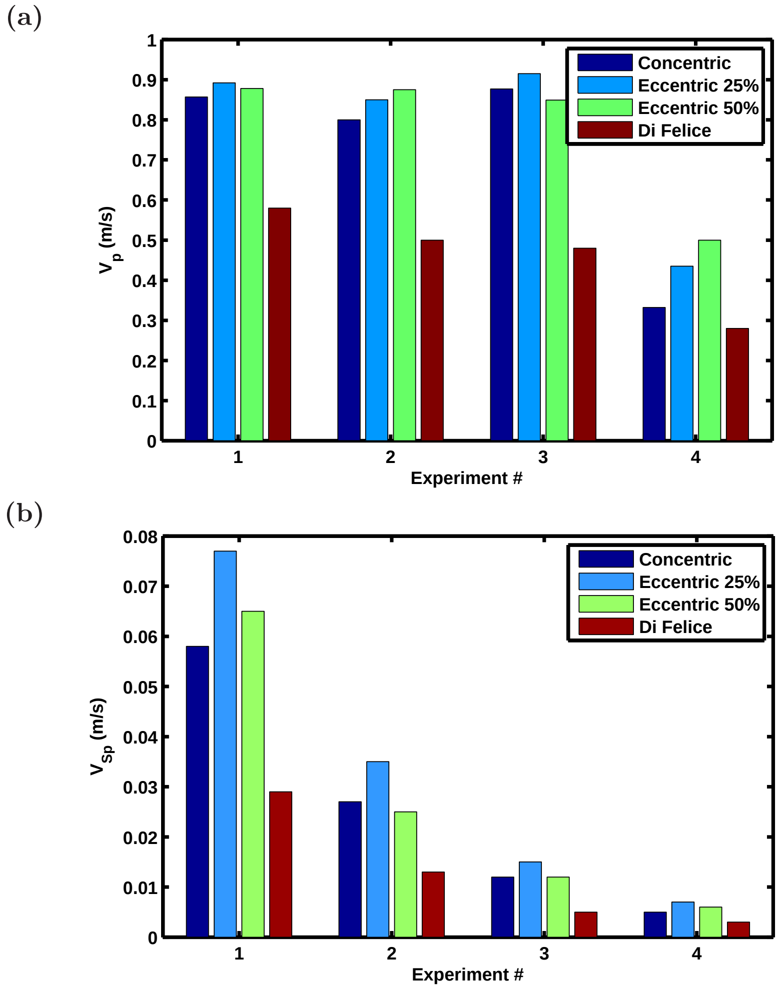

Figure 6.29: (a) Average particle velocity V_p and (b) superficial velocity of particles V_{Sp}.

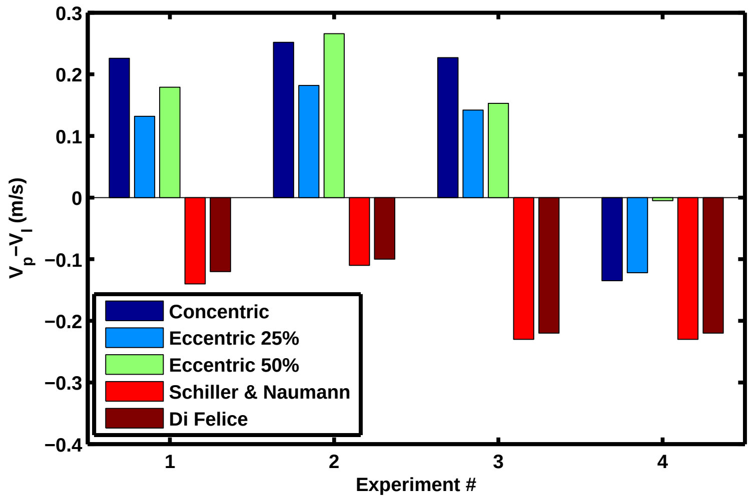

Figure 6.30: Difference between particle and liquid average velocities.

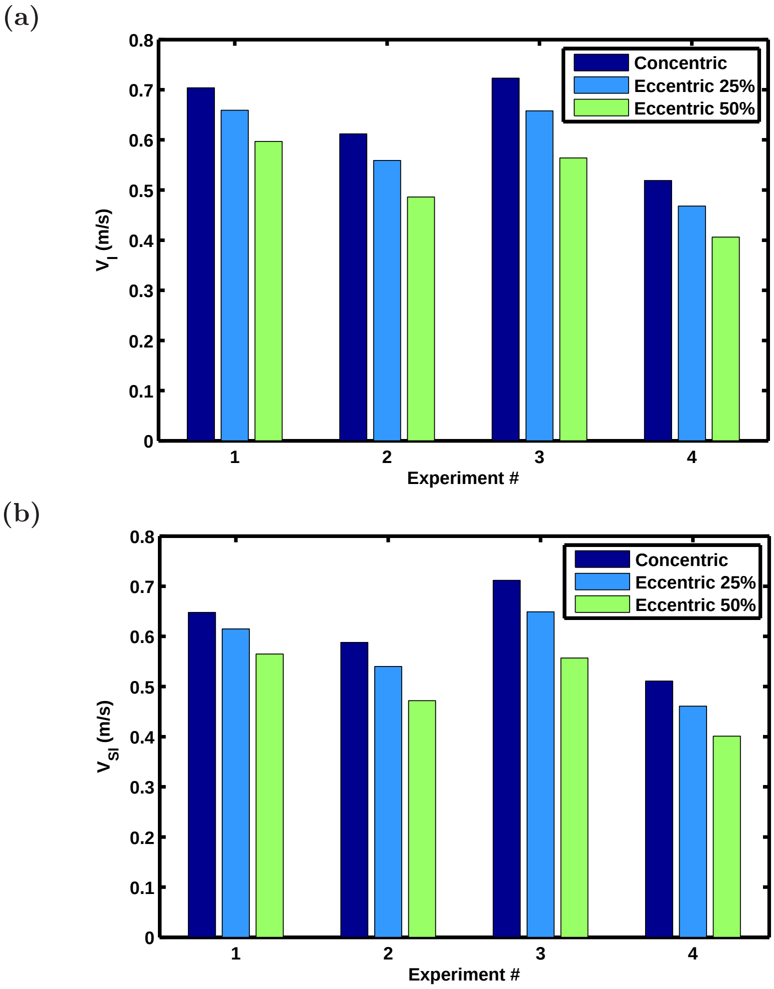

Figure 6.31: (a) Average liquid velocity V_p and (b) superficial velocity of liquid V_{Sl}.

7 Discussion and Conclusions

In this chapter, the conclusions that could be drawn from the work described in this thesis are summarized. It starts with the review of previous work and the justification for the acquisition of new knowledge in relation to cuttings transport. After that, the new implemented flow-loop, where solid-liquid suspension can be measured, is discussed. Some comments and discussions on the numerical models selected for the simulations are given in the following chapter. It continues with a summary of the findings related to the experimental results. Once this is done, the conclusions about the numerical are outlined.

7.1 Review of earlier work

A review of modeling approaches able to describe cuttings transport at the wellbore scale points out the necessity for models based on mechanistic descriptions. Clark and Bickham [12] have presented models based on these descriptions. However, these are based on several assumptions, which leave room for improvement. The assumption of homogeneous particle distributions across annular conducts in vertical transport is taken in this work as the object of investigation. Furthermore, the drift-flux model offers the possibility to integrate information of inhomogeneous particle distributions in modeling approaches convenient at the wellbore scale. Generation of correlations supplying information from wellbore diameter scale or smaller are therefore in great need.

For horizontal transport, the two- and three-layer approaches are regarded as appropriate in terms of computational speed and level of detail supplied. Again here, the current constitutive equations considering momentum and mass balance do not include the effects of eccentricity, inclination or rotation properly. Development of such constitutive equations requires also advanced understanding of transport phenomena within the wellbore. Methods able to supply this understanding could give a great impulse to cuttings transport modeling.

Previous experimental work has mainly concentrated on the generation of empirical correlations through the study of integral parameters. These are constrained to the range of conditions investigated and cannot be accurately extrapolated. Moreover, these do not supply the necessary understanding about the phenomena occurring in the wellbore. Available experimental methods are not able to offer a more detailed picture, because the medium is opaque and the drill string blocks optical access.

Several numerical methods have been developed during the last two decades to model the transport of solid-liquid suspensions. These can be used to substitute physical experiments at the wellbore diameter scale and increase the understanding of the cuttings transport physics. However, these still need careful validation. Spatial and temporal resolution is selected depending on the scale of the problem. Currently, high resolution methods solving flow fields around particles are limited to small scale problems due to the high computational resources required. The work of Capecelatro and Desjardins [64] is a nice example of such high performance computations. On the other hand, lower resolution approaches, able to simulate larger scale problems, require closure relationships still under development. This is specially the case for polydisperse suspensions and those where the carrying medium consists of one of the multiple variations of non-Newtonian rheology. For the drilling industry, shear-thinning and yield-pseudoplastic rheologies are of interest. However, most of the available closure relations have been developed for use in the chemical industry mainly focusing on solid-gas problems. Interaction of particles in viscous fluids increases its modeling complexity, because of lubrication forces appearing when particles approximate each other. Joseph et al. [46] have shown its effects on the coefficient of restitution. The work of Kempe and Fröhlich [45] represents the latest development in that respect. However, these techniques still need to be extensively tested to be considered mature. For their testing and validation, detailed experimental data are in great need.

7.2 Multiphase vertical flow-loop

A main goal of this work was to generate experimental data, which could be compared with state-of-the-art numerical methods. For this aim, a new multiphase flow loop was designed and constructed. The new flow-loop consists of a vertical test pipe, an eductor, a separating container and a multi-stage pump making possible the recirculation of suspensions with controlled volume fraction. The measuring system is based on the PIV and PTV techniques and is able to obtain measurements of the liquid and particle velocities as well as particle position histograms on a plane coaxial to the pipe. Refractive index matching techniques were necessary to avoid interferences of the borosilicate particles used as the solid phase. The selection of spherical particles also helped to obtain better optical properties. However, this was not the only reason. Although drilling cuttings present shapes differing from sphericity in multiple grades, the experiments were designed to supply systems with boundary conditions focused on the study of bidispersity. Multiple size particle would difficult the optical setting and would increase the complexity of the parameter space.

In the experiments with the highest fluid velocities slightly asymmetric velocity profiles were observed. This impurity of the boundary conditions could be solved in future works through a longer straight section of the hose bringing the suspension into the test pipe. This would translate in a larger set-up, which needs to be taken into consideration at the time of design.

Several tests were also performed with shear-thinning fluids. However, it was not possible to find an economic way to produce such fluids with refractive indexes matching those of the particles. Therefore, very low concentrations could be measured. The unsuitability of optical methods for solid-shear-thinning mixtures may require the use of methods based on other principles, as high-speed tomography.

7.3 Solid-liquid suspension measurements

Experiments were successfully performed with mono- and bidisperse suspensions of rigid particles. The results with monodisperse suspensions were used to verify the adequacy of the measuring system. These show migration of the particles to positions close to the pipe axis. This is caused by the action of the lift force appearing in shear flows. Likewise, two-way coupling effects may be clearly appreciated in the modifications of the liquid average velocity profiles. Correspondingly, this is related to the appearance of drag forces.

In bidisperse suspensions, momentum transfer between species becomes important for diameter ratios far from one, either less or higher. In transport condition, the situation is different from the one in sedimentation, due to the fact that smaller particles are faster in the transport condition. Therefore, while the transfer of momentum is from the small particles to the bigger particles, the drag coefficient of the smaller particles increases and the one of the bigger particles decreases. In sedimentation the inverse situation takes place. Since most of the previous work is focused on sedimentation cases, the experimental data offered here constitutes new insight in the momentum transfer occurring in the transport condition.

Lift forces induced by the sheared liquid drive the particles towards the center of the pipe. The accumulation in the central region flattens the velocity profiles of the fluid, because of the momentum transfer between both phases. This explains the fact that lift coefficients of different value supply similar steady state particle distributions. The lift force controls the velocity how these distributions are reached. The actual distribution is controlled by momentum transfer in the parallel direction, namely drag. The same is controlled by concentration, particle size, particle shape, density ratio and fluid viscosity.

An interesting phenomena was observed in the bidisperse experiments. It consists of the concentration of particles far from the axis and around the 0.7 non-dimensional radial position. This phenomena is different to the one first observed by Segré & Silberberg and not previously observed to the best of this author knowledge. It is caused by the modification of the fluid velocity profile and the generation of shear rates with different sign to the one normally observed in conduct flows. This modification translates in lift forces acting towards the wall contrary to the ones acting towards the axis as it is common for a dispersed phase lagging the continuous phase. The phenomena is a very clear example of three-way coupling effects. Therefore, it is a very interesting challenge for numerical methods of the resolved and unresolved classes.

It would be interesting to measure fluid and particles simultaneously at different locations from the entrance. This would allow following the progress of the concentration profiles along the entrance and quantifying the effects of lateral migration in semi-dilute suspensions while providing more complete data for validation of numerical models. This could be the subject for new research project.

7.4 Multiphase models for wellbore diameter scale

The simulations were performed to evaluate the completeness of the physical representation and to investigate the behaviour of solid-liquid suspensions with periodic boundary conditions.

An important point of this thesis was to clarify the importance of models for intermediate systems, where the hydrodynamic interaction is significant. The basic implementation used until now considers fluid-particle and particle-particle interactions. Simulations performed with higher concentrations than 2% show over prediction of liquid and solid velocities caused by spurious increase of the particles kinetic energy. Therefore, such concentrations require more detailed modeling of the hydrodynamic interactions. Lately, Kempe & Frölich [45] have proposed an adaptive collision model (ACM), which could be implemented to extent the capabilities of the CFDEM library. Likewise, the stress tensor constitutive equations should be included to be able to perform simulations with shear-thinning and yield-pseudoplastic fluids. This will also require the development of constitutive equations for particle drag and lift in such fluids. The effects of particles in such sheared fluids is itself a field of intensive research.

The comparison of the simulations with the experimental measurements allows confirmation of the validity of the CFD-DEM models. This being said, the accuracy of the simulations is dependent of the particle concentration. In this way, concentrations up to 2% show very good agreement. While for higher than 2% the accuracy suffers a progressive decrease. This is caused by the more frequent interactions of particles not being properly handled by the models. In this work, the limit has been clearly defined and allows qualification of the results obtained.

The first investigations using the CFD-DEM method have concentrated on the effect of eccentricity on particle transport through vertical annular conducts. These have shown the importance of the lift forces, which cause migration of the particles to faster transport positions. This finding contradicts the homogeneous particle distribution assumption and suggests a possible improvement of the current technique. Furthermore, the importance of the volume fraction in the cuttings transport problem requires an integral parameter able to synthesize as much information as possible. The superficial velocity of the particles V_{Sp} has this property. Optimization of particle transport should take it as the objective function. The studies presented here represent a first attempt to develop constitutive equations for the cuttings transport problem through numerical simulations. These are not self-contained and constitute the first milestone for further developments. Studies focused on the effect of eccentricity should be extended to larger parameter spaces and conditions. Further studies also based in this approach could concentrate on the effects of rotation and inclination.

Bibliography

[1] Geothermie Zentrum Bochum. Geothermal Energy. Website, 2014. http://www.geothermie-zentrum.de/en/geothermal-energy.html.

[2] R. Aragall, V. Mulchandani, S. Hahn, and G. Brenner. Multiscale approach for drilling hydraulics modelling. *OIL GAS European Magazine*, 40:28–29, 2014.

[3] K. Wilson, G. Addie, A. Sellgren, and R. Clift. *Slurry transport using centrifugal pumps*. Springer, 3 edition, 2006.

[4] C. T. Crowe, editor. *Multiphase Flow Handbook*. CRC Press, 2006.

[5] B. W. Swanson, J. R. Heritage, and D. Lawson. Wellbore Fluids Model Provides Basis for Drilling Optimization. In *SPE Annual Technical Conference and Exhibition*. Society of Petroleum Engineers, April 2013.

[6] M Ishii. Thermo-fluid dynamic theory of two-phase flow. *NASA STI/Recon Technical Report A*, 1975.

[7] P. A. Cundall and O. D. L. Strack. A discrete numerical model for granular assemblies. *Géotechnique*, 29(1):47–65, January 1979.

[8] R.K. Clark and K.L. Bickham. A Mechanistic Model for Cuttings Transport. In *SPE Annual Technical Conference and Exhibition*. Society of Petroleum Engineers, April 2013.

[9] A.A. Pilehvari, J.J. Azar, and S.A. Shirazi. State-of-the-Art Cuttings Transport in Horizontal Wellbores. *SPE Drilling & Completion*, 14(September), 1999.

[10] Tahmineh Nazari, Geir Hareland, and Jamal Joseph Azar. Review of Cuttings Transport in Directional Well Drilling: Systematic Approach. *SPE Western Regional Meeting*, 2010.

[11] Y. Luo, P. A. Bern, and B. D. Chambers. Flow-rate predictions for cleaning deviated wells. *SPE Annual Technical Conference and Exhibition*, (SPE 23884):367–376, 1992.

[12] R. K. Clark and K. L. Bickham. A mechanistic model for cuttings transport. *SPE Annual Technical Conference and Exhibition*, (SPE 28306), 1994.

[13] L. Robinson et al. *Drilling Fluids Processing Handbook*. McGraw Hill, 1979.

[14] R. Perry and C. Chilton. *Chemical Engineers Handbook*. McGraw-Hill Book Company, New York, 5 edition, 1973.

[15] R. Pigot. Mud flow in drilling. *Drill and Prod. Pract.*, pages 91–103, 1942.

[16] RP Chhabra. Bubbles, drops, and particles in non-Newtonian fluids. 2006.

[17] P. G. Saffman. The lift on a small sphere in a slow shear flow. *Journal of Fluid Mechanics*, 22:385, 1965.

[18] P. Doron, D. Garnica, and D. Barnea. Slurry flow in horizontal pipes: Experimental and modeling. *International Journal of Multiphase Flow*, 13(4):535, 1987.

[19] V. C. Kelessidis and G. E. Bandelis. Flow pattern and minimum suspension velocity for efficient cuttings transport in horizontal and deviated wells in coiled-tubing drilling. *SPE Drilling & Completion*, pages 213–227, December 2004.

[20] M. E. Ozbayoglu, A. Saasen, M. Sorgun, and K. Svanes. Effect of pipe rotation on hole cleaning for water-based drilling fluids in horizontal and deviated wells. In *IADC/SPE Asia Pacific Drilling Technology Conference and Exhibition*. Society of Petroleum Engineers, 2008.

[21] E. Cayeux, T. Mesagan, S. Tanripada, M. Zidan, and K. K. Fjelde. Real-Time Evaluation of Hole Cleaning Conditions Using a Transient Cuttings Transport Model. *SPE/IADC Drilling Conference*, page 19, 2013.

[22] S. Naganawa and T. Nomura. Simulating transient behavior of cuttings transport over whole trajectory of extended reach well. *IADC/SPE Asia Pacific Drilling . . .*, 2006.

[23] Xiao Le Guo, Zhi Ming Wang, and Zhi Hui Long. Study on three-layer unsteady model of cuttings transport for extended-reach well. *Journal of Petroleum Science and Engineering*, 73(1-2):171–180, 2010.

[24] N. Zuber and J. Findlay. Average volumetric concentration in two-phase flow systems. *Journal of Heat Transfer*, 87(4):453–468, 1965.

[25] G. B. Wallis. *One-dimensional two-phase flow*, volume 1. McGraw-Hill New York, 1969.

[26] Svend Tollak Munkejord. *Analysis of the two-fluid model and the drift-flux model for numerical calculation of two-phase flow.* PhD thesis, Norwegian University of Science and Technology, 2006.

[27] D. Brennan. *The Numerical Simulation of Two-Phase Flows in Settling Tanks.* Phd., University of London, 2001.

[28] A. Pilehvari and R. Serth. Generalized hydraulic calculation method for axial flow of non-newtonian fluids in eccentric annuli. *SPE drilling & completion*, 24(04):553–563, 2009.

[29] E. Guazzelli and J. F. Morris. *A Physical Introduction to Suspension Dynamics*. Cambridge University Press, 2012.

[30] R. J. Hill, D. L. Koch, and A. J. C. Ladd. The first effects of fluid inertia on flows in ordered and random arrays of spheres. *Journal of Fluid Mechanics*, 448(2):213–241, 2001.

[31] R. J. Hill, D. L. Koch, and A. J. C. Ladd. Moderate-reynolds-number flows in ordered and random arrays of spheres. *Journal of Fluid Mechanics*, 448(2):243–278, 2001.

[32] M. A. Van der Hoef, R. Beetstra, and J. A. M. Kuipers. Lattice-boltzmann simulations of low-reynolds-number flow past mono- and bidisperse arrays of spheres: results for the permeability and drag force. *Journal of Fluid Mechanics*, 528:233–254, 2005.

[33] X. Yin and S. Sundaresan. Drag law for bidisperse gas- solid suspensions containing equally sized spheres. *Industrial & Engineering Chemistry Research*, 48(1):227–241, 2008.

[34] M. Sommerfeld, B. van Wachem, and R. Oliemans. Dispersed turbulent multi-phase flow. *Best practice guidelines, ERCOFTAC*, 2009.

[35] G. Segré and A. Silberberg. Behaviour of macroscopic rigid spheres in poiseuille flow part 2. experimental results and interpretation. *Journal of Fluid Mechanics*, 14:136–157, 1961.

[36] F. Takemura and J. Magnaudet. Lateral migration of a small spherical buoyant particle in a wall-bounded linear shear flow. *Physics of fluids*, (21), 2009.

[37] Z. Yu, N. Phan-Thien, and R. I. Tanner. Dynamic simulation of sphere motion in a vertical tube. *Journal of Fluid Mechanics*, 518:61–93, 2004.

[38] H. Aoki, Y. Kurosaki, and H. Anzai. Study on the tubular pinch effect in a pipe flow. i. lateral migration of a single particle in laminar poiseuille flow. *JSME*, 22(164):206–212, 1979.

[39] Z. Yu and X. Shao. Direct numerical simulation of particulate flows with a fictitious domain method. *International Journal of Multiphase Flow*, (36):127–134, 2009.

[40] C. T. Clayton, J. D. Schwarzkopf, M. Sommerfeld, and Y. Tsuji. *Multiphase flows with droplets and particles*. CRC press, 2011.

[41] F. Odar and W. S. Hamilton. Forces on a sphere accelerating in a viscous fluid. *Journal of Fluid Mechanics*, 18(02):302–314, 1964.

[42] M. W. Reeks and S. McKee. The dispersive effects of basset history forces on particle motion in a turbulent flow. *Physics of Fluids (1958-1988)*, 27(7):1573–1582, 1984.

[43] E. E. Michaelides and A. Roig. A reinterpretation of the odar and hamilton data on the unsteady equation of motion of particles. *AIChE Journal*, 57(11):2997–3002, 2011.

[44] M. Sommerfeld. *Modellierung und numerische Berechnung von partikelbeladenen turbulenten Strömungen mit Hilfe des Euler-Lagrange-Verfahrens*. Shaker, 1996.

[45] T. Kempe and J. Fröhlich. Collision modelling for the interface-resolved simulation of spherical particles in viscous fluids. *Journal of Fluid Mechanics*, 709:445–489, 2012.

[46] G. G. Joseph, R. Zenit, M. L. Hunt, and A. M. Rosenwinkel. Particle–wall collisions in a viscous fluid. *Journal of Fluid Mechanics*, 433:329–346, 2001.

[47] H. R. Davis, J.-M. Serayssol, and E. J. Hinch. The elastohydrodynamic collision of two spheres. *Journal of Fluid Mechanics*, 163:479–497, 1986.

[48] Ch. Brücker. Piv in two-phase flows. *von Karman Institute for fluid dynamics, Lecture Series*, 1, 2000.

[49] C. Poelma. *Experiments in particle-laden turbulence*. PhD thesis, Technical University of Delft, 2004.

[50] A. Brandt and W. Merzkirch. Particle image velocimetry applied to a spray jet. *Particle & particle systems characterization*, 11(2):156–158, 1994.

[51] Y. A. Hassan, T. K. Blanchat, C. H. Seeley, and R. E. Canaan. Simultaneous velocity measurements of both components of a two-phase flow using particle image velocimetry. *International Journal of Multiphase Flow*, 18(3):371–395, 1992.

[52] A. L. Tassin, C.-Y. Li, S. L. Ceccio, and L. P. Bernal. Velocity field measurements of cavitating flows. *Experiments in fluids*, 20(2):125–130, 1995.

[53] M. L. Jakobsen, W. J. Easson, C. A. Greated, and D. H. Glass. Particle image velocimetry: simultaneous two-phase flow measurements. *Measurement Science and Technology*, 7(9):1270, 1996.

[54] S. Torii and W.-J. Yang. Melt-particle mixing in gas-stirred ladles with throughflow. *Experiments in fluids*, 13(1):37–42, 1992.

[55] A. Zachos, M. Kaiser, and W. Merzkirch. Piv measurements in multiphase flow with nominally high concentration of the solid phase. *Experiments in fluids*, 20(3):229–231, 1996.

[56] W. Merzkirch, L. Gui, S. Hilgers, R. Lindken, and T. Wagner. Piv in multiphase flow. In *The second international workshop on PIV*, pages 8–11, 1997.

[57] Y. Hassan. Bubble collapse velocity measurements using a particle image velocimetry technique with fluorescent tracers. *ASME FLUIDS ENG DIV PUBL FED, ASME, NEW YORK, NY,(USA), 1993,*, 172:85–92, 1993.

[58] L. Gui and W. Merzkirch. Phase-separation of piv measurements in two-phase flow by applying a digital mask technique. *ERCOFTAC Bull*, 30:45–48, 1996.

[59] K. Nishino and H. Katoand K. Torii. Stereo imaging for simultaneous measurement of size and velocity of particles in dispersed two-phase flow. *Measurement Science and Technology*, 11(6):633, 2000.

[60] R. Lindken and W. Merzkirch. A novel piv technique for measurements in multiphase flows and its application to two-phase bubbly flows. *Experiments in fluids*, 33(6):814–825, 2002.

[61] Derksen D. Eskinand J. Introduction to a series of featured articles:“multiphase computational fluid dynamics for industrial processes”. *Canadian Journal of Chemical Engineering*, 89(2):203, 2010.

[62] Donald L. Koch and Reghan J Hill. Inertial Effects in Suspension and Porous-Media Flows. *Anual review Fluid Mech*, pages 619–647, 2001.

[63] R. Beetstra, M.A. Van der Hoef, and J. A. M. Kuipers. Drag force of intermediate reynolds number flow past mono- and bidisperse arrays of spheres. *AIChE Journal*, 53:489–501, 2007.

[64] J. Capecelatro and O. Desjardins. Eulerian–lagrangian modeling of turbulent liquid–solid slurries in horizontal pipes. *International journal of multiphase flow*, 55:64–79, 2013.

[65] Z. Y. Zhou, S. B. Kuang, K. W. Chu, and A. B. Yu. Discrete particle simulation of particle–fluid flow: model formulations and their applicability. *Journal of Fluid Mechanics*, 661:482–510, 2010.

[66] BPB Hoomans and JAM Kuipers. Discrete particle simulation of bubble and slug formation in a two-dimensional gas-fluidised bed: a hard-sphere approach. *Chemical Engineering . . .*, 1996.

[67] N. G. Deen, M. Van Sint Annaland, M. a. Van der Hoef, and J. a M Kuipers. Review of discrete particle modeling of fluidized beds. *Chemical Engineering Science*, 62:28–44, 2007.

[68] S. McNamara and W. R. Young. Inelastic collapse and clumping in a one-dimensional granular medium. *Physics of Fluids A: Fluid Dynamics (1989-1993)*, 4(3):496–504, 1992.

[69] Y. Tsuji, T. Kawaguchi, and T. Tanaka. Discrete particle simulation of two-dimensional fluidized bed. *Powder technology*, 77(1):79–87, 1993.

[70] B. H. Xu and A. B. Yu. Numerical simulation of the gas-solid flow in a fluidized bed by combining discrete particle method with computational fluid dynamics. *Chemical Engineering Science*, 52(16):2785–2809, 1997.

[71] C.-Y. Yang, Y. Ding, D. York, and W. Broeckx. Numerical simulation of sedimentation of microparticles using the discrete particle method. *Particuology*, 6(1):38–49, 2008.

[72] K. Apostolouand A. N. Hrymak. Discrete element simulation of liquid-particle flows. *Computers & Chemical Engineering*, 32(4):841–856, 2008.

[73] A. Biesheuvel and L. van Wijngaarden. Two-phase flow equations for a dilute dispersion of gas bubbles in liquid. *Journal of Fluid Mechanics*, 148:301–318, 1984.

[74] D. A. Drew. Mathematical modeling of two-phase flow. Technical report, DTIC Document, 1982.

[75] A. Tchikango Siagam. *Numerische und experimentelle Strömungsuntersuchungen in Festbetten mit kleinen Formverhältnissen*. PhD thesis, Technical University of Clausthal, 2009.

[76] T. Peng. Detect circles with various radii in grayscale image via hough transform. MATLAB Central File Exchange, retrieved June 10, 2010.

[77] R. Aragall, F. Yu, J. Dai, and G. Brenner. Closure of drift-flux models for cuttings transport predictions. *OIL GAS European Magazine*, 41:15–18, 2015.

[78] E. Kriegel and H. Brauer. Hydraulischer transport körniger feststoffe durch waagerechte rohrleitungen. *VDI Forschungsheft*, (515), 1966.

[79] E. Carpintero-Rogero and B. Krössand T. Sattelmayer. Simultaneous hs-piv and shadowgraph measurements of gas-liquid flows in a horizontal pipe. In *13th Int. Symp. on Applications of Laser Techniques to Fluid Mechanics, Lisbon, Portugal*, pages 26–29, 2006.

[80] A. Goharzadeh and P. Rodgers. Experimental measurement of laminar axisymmetric flow through confined annular geometries with sudden inward expansion. *Journal of Fluids Engineering*, 131(12):124501, 2009.

[81] M. Raffel, C. E. Willert, and J. Kompenhaus. *Particle Image Velocimetry- A Practical Guide*. Springer Publications, 1998.

[82] R. Budwig. Refractive index matching methods for liquid flow investigations. *Experiments in Fluids*, 17(5):350–355, September 1994.

[83] A. Zachos, M. Kaiser, and W. Merzkirch. PIV measurements in multiphase flow with nominally high concentration of the solid phase. *Experiments in Fluids*, 20:229–231, 1996.

[84] M. M. Cui and R. J. Adrian. Refractive index matching and marking methods for highly concentrated solid-liquid flows. *Experiments in Fluids*, 22:261–264, 1997.

[85] Inci Ayranci, Márcio B. Machado, Adam M. Madej, Jos J. Derksen, David S. Nobes, and Suzanne M. Kresta. Effect of geometry on the mechanisms for off-bottom solids suspension in a stirred tank. *Chemical Engineering Science*, 79:163–176, September 2012.

[86] I. Ayranci, S. M. Kresta, and J. J. Derksen. Experiments and Simulations on Bidisperse Solids Suspension in a Mixing Tank. *Chemical Engineering & Technology*, 36(11):1957–1967, November 2013.

[87] H. Rusche. *Computational fluid dynamics of dispersed two-phase flows at high phase fractions*. PhD thesis, Imperial College London (University of London), 2003.

[88] B.G.M. van Wachem and A.E. Almstedt. Methods for multiphase computational fluid dynamics. *Chemical Engineering Journal*, 96(1-3):81–98, December 2003.

[89] Dimitri Gidaspow. *Multiphase Flow and Fluidization: Continuum and Kinetic Theory Descriptions*. Academic press, 1994.

[90] L. Schiller and A. Naumann. Vdi-zeitschrift 77 (1933).

[91] R. Mei. An approximate expression for the shear lift force on a spherical particle at finite reynolds number. *International Journal of Multiphase Flow*, 18(1):145–147, 1992.

[92] P. G. Saffman. The lift on a small sphere in a slow shear flow. *Journal of Fluid Mechanics*, 22(2):385–400, 1965.

[93] D. S. Dandy and H. A. Dwyer. A sphere in shear flow at finite reynolds number: effect of shear on particle lift, drag, and heat transfer. *Journal of Fluid Mechanics*, 216:381–410, 1990.

[94] Christoph Goniva, Christoph Kloss, Niels G. Deen, Johannes a M Kuipers, and Stefan Pirker. Influence of rolling friction on single spout fluidized bed simulation. *Particuology*, 10(5):582–591, 2012.

[95] CT Crowe, JD Schwarzkopf, M Sommerfeld, and Y Tsuji. *Multiphase flows with droplets and particles*. CRC press, 2011.

[96] MA Van der Hoef and M A Van der Hoef. Numerical simulation of dense gas-solid fluidized beds: A multiscale modeling strategy. *Annu. Rev. Fluid . . .*, 2008.

[97] C Goniva, C Kloss, and S Pirker. Towards fast parallel CFD-DEM: An open-source perspective. *Open Source CFD International . . .*, 2009.

[98] Christoph Goniva. CFDEMcoupling Documentation. Technical report, DCS Computing GmbH, 2012.

[99] J. M. Link, L. a. Cuypers, N. G. Deen, and J. a M Kuipers. Flow regimes in a spout-fluid bed: A combined experimental and simulation study. *Chemical Engineering Science*, 60:3425–3442, 2005.

[100] R. Di Felice. The voidage function for fluid-particle interaction systems. *International Journal of Multiphase Flow*, 20(1):153–159, 1994.

[101] M. Sommerfeld, B. van Wachen, and R. Oliemans. *Best practice Guidelines for Computational Fluid Dynamics of Dispersed Multiphase Flows*. ERCOFTAC, 2008.

[102] E. E. Michaelides. *Particles, Bubbles & Drops. Their motion heat and mass transfer*. World Scientific, 2006.

[103] S. Ergun. Fluid flow through packed columns. *Chemical Engineering Progress*, (48):89–94, 1952.

[104] Y. C. Wen and Y. H. Yu. Mechanics of fluidization. *Chemical Engineering Progress Symposium Series*, 62:110–111, 1966.

[105] J.F. Richardson and W.N. Zaki. The sedimentation of a suspension of uniform spheres under conditions of viscous flow. *Chemical Engineering Science*, 3(2):65 – 73, 1954.

[106] Hrvoje Jasak. *Error Analysis and Estimation for the Finite Volume Method with Applications to Fluid Flows*. PhD thesis, 1996.

[107] Mahsa Bagherzadeh. *Modelling Single Particle Settlement by CFD-DEM Coupling Method*. PhD thesis, Delft University of Technology, 2014.

[108] C. Kloss and S. Pirker. Coupling of DEM and CFD: simulation and experiment. Discrete Element Method, 2009. Kopenhagen.

[109] BK Mishra. A review of computer simulation of tumbling mills by the discrete element method: part I—contact mechanics. *International Journal of Mineral Processing*, 2003.

[110] AO Raji and JF Favier. Model for the deformation in agricultural and food particulate materials under bulk compressive loading using discrete element method. I: Theory, model development. *Journal of food engineering*, 2004.

[111] Z Ning and M Ghadiri. Distinct element analysis of attrition of granular solids under shear deformation. *Chemical engineering science*, 2006.

[112] Y Li, Y Xu, and C Thornton. A comparison of discrete element simulations and experiments for 'sandpiles' composed of spherical particles. *Powder Technology*, 2005.

[113] W. Thielicke and E. J. Stamhuis. PIVlab - Time-Resolved Digital Particle Image Velocimetry Tool for MATLAB. MATLAB Central File Exchange, retrieved November 9, 2011.

[114] C. J. Koh, P. Hookham, and L. G. Leal. An experimental investigation of concentrated suspension flows in a rectangular channel. *Journal of Fluid Mechanics*, 266:1–31, 1994.

[115] J. P. Matas, J. F. Morris, and E. Guazzelli. Inertial migration of rigid spherical particles in poiseuille flow. *Journal of Fluid Mechanics*, 515:171–195, 2004.

[116] D. M. Newitt, J. F. Richardson, M. Abbott, and R. B. Turtle. Hydraulic conveying of solids in horizontal pipes. *Transactions of the Institution of Chemical Engineers*, 33:93–113, 1955.

[117] M. Toda, H. Konno, S. Saito, and S. Maeda. Hydraulic conveying of solids through horizontal and vertical pipes. *International Chemical Engineering*, 9(3):553–560, 1969.

[118] R. C. Jeffrey and J. R. A. Pearson. Particle motion in laminar vertical flow. *Journal of Fluid Mechanics*, 22(4):721–735, 1965.

[119] A. J. Hogg. The inertical migration of non-neutrally buoyant spherical particles in two-dimensional shear flows. *Journal of Fluid Mechanics*, 272:285–318, 1994.

[120] A. Haider and O. Levenspiel. Drag coefficient and terminal velocity of spherical and nonspherical particles. *Powder Technology*, 58:63–70, 1989.

[121] P. Vasseur and R. G. Cox. The lateral migration of a spherical particle in two-dimensional shear flows. *Journal of Fluid Mechanics*, 78:385–413, 1976.

[122] Jean-Philippe Matas, Jeffrey F. Morris, and Élisabeth Guazzelli. Inertial migration of rigid spherical particles in Poiseuille flow. *Journal of Fluid Mechanics*, 515:171–195, 2004.

List of Figures

List of Tables

List of Publications

Aragall, R., Mulchandani, V., and Brenner, G. (2015a). Optical measurement and numerical analysis of mono-and bidisperse coarse suspensions in vertical axisymmetric sudden-expansion. International Journal of Multiphase Flow, 69, 63-80.

Aragall, R., Yu, F., Dai, J. and Brenner, G. (2015b). Closure of Drift-Flux Models for Cuttings Transport Predictions. OIL GAS European Magazine, 41, 15-18.

Aragall, R., Mulchandani, V., Hahn, S. and Brenner, G. (2014a). Multiscale approach for drilling hydraulics modelling. OIL GAS European Magazine, 40, 28-29.

Aragall R., Hahn S., Mulchandani V., Brenner G. (2014b): Multiscale Approach for Drilling Hy-draulics Modeling II, paper presented at 2nd International Symposium on Multiscale Multi-phase Process Engineering, Hamburg, September 24-27, 2014.

Aragall R., Mulchandani V. and Brenner G. (2013a): Analyse von plötzlichen axialsymmetrischen Erweiterungen von bidispersen Suspensionen in laminaren Strömungen (Analysis of bidisperse suspension laminar flows in axisymmetric sudden expansions), presented at Jahrestreffen der ProcessNet Fachgruppen Fluiddynamik und Trenntechnik, Würzburg, Germany, September 25-26, 2013. Paper published at Chemie Ingenieur Technik, Number 9, Pages 1433-1434, September 2013.

Aragall R., Mulchandani V. and Brenner G. (2013b): Experimental analysis on bidispersed particle transport in laminar pipe flow, presented at Jahrestreffen der ProcessNet Fachgruppen Agglomerations- und Schüttguttechnik und Computational Fluid Dynamics, Weimar, March 4-6, 2013.

Aragall R. and Brenner G. (2012): Detailed quantification of dispersed particles transport through PIV and PTV measuring technique, paper presented at 13th Workshop on Two-Phase Flow Predictions, Halle, Germany, September 17-20, 2012.

Aragall R., Kumar P. and Brenner G. (2011): Simultaneous measurements of solid parti-

cle and fluid velocity in two-phase pipe flows using combined PIV/PTV techniques, paper presented at 19. Fachtagung zu Lasermethoden in der Strömungsmesstechnik, Ilmenau, Germany, 6-8 September 2011.

Curriculum Vitae

Personal data

Name	Roger Aragall Tersa
Birth date & place	16.02.1978, Barcelona, Spain
Nationality	Spanish
Marital status	married with two children

Education and training

09.1992 - 06.1996	Spanish Baccalaureate - Institut d'Ensenyament Secundari Vilatzara, Vilassar de Mar, Spain. Between 09.1994 and 06.1995 exchange program at Falconer Central School, Falconer, USA.
09.1998 - 06.2002	Bachelor in Mechanical Engineering - Universitat Politècnica de Catalunya, Escola Universitaria d'Enginyeria Tècnica Industrial de Barcelona, Barcelona, Spain
09.2006 - 06.2009	Diploma in Mechanical Engineering - Universitat de Girona, Escola Politècnica Superior, Girona, Spain. Between 07.2008 and 09.2008 practical training at Ilmenau University of Technology, Ilmenau, Germany. Between 01.2009 and 06.2009 ERASMUS exchange program at Clausthal University of Technology, Clausthal-Zellerfeld, Germany.

Work experience

07.2002 - 07.2004	Project Engineer - EDS Applikations & Manipulations Systeme, Viladecans, Spain.
08.2004 - 08.2006	Industrial Engineer - SUINCASA Level Sensoring, Cabrera de Mar, Spain.
07.2009 - 09.2015	Research Assistant - Institute of Applied Mechanics, Clausthal University of Techonology, Clausthal-Zellerfeld, Germany.
since 09.2015	Research Engineer - Drilling Simulator Celle, Clausthal University of Techonology, Celle, Germany.